1-31-2013

Quantification and propagation of nuclear data uncertainties

Michael Rising

Michael E. Rising
Candidate

Chemical and Nuclear Engineering
Department

This dissertation is approved, and it is acceptable in quality and form for publication:

Approved by the Dissertation Committee:

Anil Prinja , Chairperson

Cassiano de Oliveira

Evangelos Coutsias

Patrick Talou

Quantification and Propagation of Nuclear Data Uncertainties

by

Michael E. Rising

B.S., Nuclear Engineering, Oregon State University, 2006
M.S., Nuclear Engineering, Oregon State University, 2008

DISSERTATION

Submitted in Partial Fulfillment of the
Requirements for the Degree of

Doctor of Philosophy
Engineering

The University of New Mexico

Albuquerque, New Mexico

December, 2012

Acknowledgments

First, I would like to express my gratitude for my advisor at UNM, Anil Prinja. Four years ago, he agreed to take me on as a graduate student and I could not be more thankful. His patience, thoughtfulness and steady guidance both in the classroom and in research meetings has helped me to develop over the years. I would also like to thank him for sharing his infinite knowledge of transport theory and uncertainty quantification methods with me, for this research would not have been possible otherwise. Second, I would like to thank my mentor at LANL, Patrick Talou. For the last three years, I have had the pleasure of learning a great deal about nuclear physics and data evaluation methods from him. He has been an outstanding mentor by engaging me with insightful discussion and providing helpful critique of my work. My hope is that, no matter where my future work takes me, I will be able to maintain a close working relationship with both my advisor, Anil Prinja, and my mentor, Patrick Talou. I would also like to thank my remaining committee members, Cassiano de Oliveira and Vageli Coutsias. I am grateful for both the skills I gained as a student in their classes as well as for their participation in this process. Finally, I would like to acknowledge Forrest Brown, Brian Kiedrowski, Erin Fichtl, Toshihiko Kawano and Morgan White, and thank them for the helpful discussions we have had at various times during my internship at LANL.

Also, I would like to thank my friends and family for their endless support throughout the years. Transitioning to a life in New Mexico has been made possible in part by the continued relationship with my friends from Oregon, the new friendships I have made here and the support of the entire James family. I would especially like to thank my parents, Susan and David Rising, for the endless love and support they have provided over the last 28 years. I can honestly state that without their constant influence in my life, I would be nowhere near where I am today. Finally, I would like to give special thanks to my wife and soulmate, Heather. Her love, support, strength, optimism, and other countless qualities, too many to list here, have made my life so much better. And for that, I sincerely thank her.

Quantification and Propagation of Nuclear Data Uncertainties

by

Michael E. Rising

B.S., Nuclear Engineering, Oregon State University, 2006
M.S., Nuclear Engineering, Oregon State University, 2008

Ph.D., Engineering, University of New Mexico, 2012

Abstract

The use of several uncertainty quantification and propagation methodologies is investigated in the context of the prompt fission neutron spectrum (PFNS) uncertainties and its impact on critical reactor assemblies. First, the first-order, linear Kalman filter is used as a nuclear data evaluation and uncertainty quantification tool combining available PFNS experimental data and a modified version of the Los Alamos (LA) model. The experimental covariance matrices, not generally given in the EXFOR database, are computed using the GMA methodology used by the IAEA to establish more appropriate correlations within each experiment. Then, using systematics relating the LA model parameters across a suite of isotopes, the PFNS for both the uranium and plutonium actinides are evaluated leading to a new evaluation including cross-isotope correlations. Next, an alternative evaluation approach, the unified Monte Carlo (UMC) method, is studied for the evaluation of the PFNS for the n(0.5 MeV)^{239}Pu fission reaction and compared to the Kalman filter. The UMC

approach to nuclear data evaluation is implemented in a variety of ways to test convergence toward the Kalman filter results and to determine the nonlinearities present in the LA model. Ultimately, the UMC approach is shown to be comparable to the Kalman filter for a realistic data evaluation of the PFNS and is capable of capturing the nonlinearities present in the LA model. Next, the impact that the PFNS uncertainties have on important critical assemblies is investigated. Using the PFNS covariance matrices in the ENDF/B-VII.1 nuclear data library, the uncertainties of the effective multiplication factor, leakage, and spectral indices of the Lady Godiva and Jezebel critical assemblies are quantified. Using principal component analysis on the PFNS covariance matrices results in needing only 2–3 principal components to retain the PFNS uncertainties. Then, using the polynomial chaos expansion (PCE) on the uncertain output quantities, the stochastic collocation method (SCM) is used to compute the PCE coefficients. Compared to the "brute force" Monte Carlo forward propagation method, the PCE-SCM approach is shown to be capable of obtaining the same amount of output quantity uncertainty information with orders of magnitude computational savings. Finally, the uncertainties quantified in the correlated model parameters for the suite of uranium and plutonium actinides are propagated through the Big Ten and Flattop assemblies. In the case of the k_{eff} uncertainties in the Big Ten assembly, the uncorrelated PFNS uncertainties leads to 17.5% smaller predicted uncertainties compared with the correlated PFNS uncertainties, suggesting the presence of these cross-isotope correlations are important for this application. Last, the unified Monte Carlo + total Monte Carlo (UMC+TMC) method is implemented to propagate uncertainties from the prior LA model parameters through the Flattop critical assemblies. Due to the fact that cross-experiment correlations are neglected in all of the present evaluation work, the UMC+TMC suffers by predicting smaller uncertainties in the integral quantities by an order of magnitude or more compared to direct sampling from the posterior LA model parameters.

Contents

List of Figures

List of Tables

Chapter 1

Introduction

For several decades in the reactor physics and nuclear engineering application community there has been a need to know how precise the result of a neutron transport simulation is with the focus on improving accuracy and safety margins. While the methodologies, algorithms and computing capabilities have improved over the years, the sources of errors and uncertainties in the transport calculations began to be a major research topic. Some errors in the calculations come from the methodologies used to solve the transport simulations including both discretization errors and statistical noise while other errors come from the lack of knowledge of the system geometry and material composition. Both of these types of errors have been able to be reduced through improvements in the algorithms and increased computer resources with the knowledge of the system being increased from improved accuracy in the measurements of the geometry and material composition. Another source of error in a neutron transport simulation comes directly from the nuclear data, which describes exactly how the neutrons in the simulation interact with the material in the system. Some of the nuclear data that is needed in any given transport simulation can be lacking either due to the difficult to experimentally measure or because of insufficient nuclear physics theory to fully understand. This brings up an important aspect of

this research, which is to identify where uncertainties need to be quantified in the evaluated nuclear data. The most modern evaluated nuclear data libraries, such as ENDF/B-VII.1 in the US [1], JENDL-4.0 in Japan [2], and JEFF-3.1.1 in Europe [3], have already begun expanding on the amount of nuclear data stored to include as much information about the nuclear data uncertainty as needed. This expansion is due to the need within the nuclear application communities (e.g., advanced reactors, medicine, non-proliferation, astrophysics, etc.) to propagate uncertainties through transport simulations so that we can begin to understand the impact that the nuclear data uncertainties alone have on the important integral solutions.

Some examples of important nuclear data include cross sections, angular distributions of scattering interactions and neutron emission, prompt and delayed fission neutron spectra, average fission neutron multiplicities and fission neutron multiplicity distributions. While much work has been devoted to the precise evaluation of cross sections and the associated covariance matrices with recent results obtained as part of the Organization for Economic Cooperation and Development (OECD), Working Party on Evaluation and Cooperation (WPEC) Subgroup 26 [4], it has been pointed out that uncertainties in fission neutron spectra can have a significant impact on the effective multiplication factor in some critical benchmark problems [5]. And, in some other selected integral benchmarks, recent estimates of the neutron fission spectrum uncertainties have been shown to be as important as cross section uncertainties [6, 7]. Partially due to these results from the selected integral benchmarks and because many of the minor actinides in the ENDF/B-VII.1 library [1] have crude evaluated prompt fission spectrum data and even more limited covariance data, an important part of this work focuses on the quantification of uncertainties of the evaluated average prompt fission neutron spectrum (PFNS) for many relevant actinides.

For example, some of the PFNS evaluations for many of the actinides have outdated evaluated mean values due to the availability of more up-to-date theoretical

models and/or experimental results, and many of the actinide evaluated files do not include PFNS covariance matrices. For the most important actinides (e.g. ^{235}U, ^{238}U and ^{239}Pu) evaluations have recently been released in the ENDF/B-VII.1 nuclear data library, but the need for nuclear data and uncertainty evaluations on the minor actinides has increased, especially under the advanced fuel cycle initiative (AFCI) [6, 7] and the increased interest in designing Generation-IV fast reactors [8].

Not only has there been an increased interest in uncertainty quantification but there has been interest in propagating the uncertainties through radiation transport simulations. It is important to study how the uncertainties in the data affect the uncertainty in the final integral quantities of interest including, for example, the effective multiplication factor of a critical system. By studying the uncertainty of the solutions of the transport simulations we can provide feedback to the nuclear data evaluators to help identify where the largest deficiencies still exist. This information can be used to help guide the kind of experiments that need to be done or on which topic theoretical research needs to be focusing on.

Presently, in the ENDF/B-VII.1 evaluated library [1], in order to combine experimental PFNS data with theoretical model calculations the Kalman filter is used [9]. The Kalman filter used in nuclear data evaluations is a first order Bayesian approach and works best if the system response is linear near the central value. Of course, if the system response is nonlinear, the Kalman filter may lead to an evaluation that is inaccurate and inappropriate for use in physics simulations. Therefore, if a significant difference can be seen between the evaluations and their impact on an important application, the quality of the evaluated and covariance data can potentially be seen as a weakness of the current evaluation methodology. The Unified Monte Carlo (UMC) sampling method [10] has been investigated for a few test problems and could be seen as a method to exactly sample from the prior probability distribution functions (PDF) of the theoretical model parameters and minimize those results with respect

to the experimental data used to constrain the model.

The methodology for propagating uncertainties through nuclear physics simulations should also be addressed. There has been work done in the area of uncertainty propagation through nuclear physics simulations including but not limited to sensitivity analysis and perturbation theory [7]. Due to the lack of some evaluated covariance matrices, the propagation of PFNS uncertainties has not been widely investigated. Also, because the UMC method has not yet been implemented for any serious evaluation, a comparison to the Kalman uncertainty propagation results has yet to be done. An alternative approach, the so-called "Total" Monte Carlo methodology [11], takes the prior model parameters and samples from a filtered parameter space to create a realization of the nuclear data of interest. Each realization of the nuclear data set is propagated through a nuclear physics simulation and the final accepted data set is determined from the calculated integral parameters that minimizes discrepancies with the experimentally measured integral parameters. While the idea of bypassing the covariance matrix formulation is tempting this methodology does not explicitly include the differential experimental data available.

The focus of this research is to describe the current state of some important nuclear data evaluations, propose new methods for quantification of uncertainties of evaluated nuclear data and propagate uncertainty through important nuclear physics simulations. The remainder of this dissertation is organized as follows:

- In Chapter 2, we introduce prompt-critical fast reactor systems, neutron transport theory, computational techniques used to simulate nuclear physics experiments, sources of nuclear data uncertainties and the prompt fission neutron spectrum theory.

- In Chapter 3, we introduce uncertainty quantification techniques applied to the evaluated prompt fission neutron spectrum.

- Chapter 4 presents numerical results of applying these uncertainty quantification methods, and discusses the merits and hurdles in each of those.
- In Chapter 5 we discuss the propagation of nuclear data uncertainties. Specifically, we discuss covariance matrix decomposition techniques, and direct sampling and polynomial chaos expansion methods.
- In Chapter 6 we present the numerical results of propagating uncertainties comparing each of the propagation methods introduced.
- In Chapter 7 we draw some conclusions from the numerical results presented and discuss several suggestions for future research that could extend the work reported in this dissertation.

Chapter 2

Background

2.1 Nuclear Physics Critical Assemblies

In the modern era of nuclear physics and engineering research majority of efforts are often directed toward improvements in nuclear physics theory, computational physics methods and numerical algorithm development rather than toward new nuclear physics experiments. Granted, new nuclear physics experiments do get built occasionally, including both the recent developments on the TPC (time-projection chamber) and Chi-Nu experiment at Los Alamos National Laboratory (LANL) used in the re-evaluation efforts of the fission cross section and PFNS, the expense in designing, testing and safely operating an experiment that includes exotic nuclear material can be prohibitive. With increased interest in designing Generation-IV fast reactors [8], the knowledge available from previous experiments need to be utilized to continue improving the state-of-the-art in the future of nuclear engineering design. Previously built nuclear physics experiments, including many of the critical and subcritical assemblies operated at the Pajarito site at LANL [12] may be currently decommissioned, but have been studied extensively for decades and provide

excellent benchmarks for various applications.

Radiation transport critical assembly experiments are some of the most well known and heavily studied physics experiments available for the computational physicist to benchmark nuclear engineering application codes. In fact, the ICSBEP handbook [13] is a compilation of many critical assemblies spanning various materials, geometries and configurations used specifically for validating radiation transport codes. Early on in the study of nuclear fissile materials, many critical assemblies were designed exclusively for the weapons program with a large focus on criticality safety. Many of these tests were composed of highly enriched uranium or plutonium metal and in a simple geometric shape, usually in spherical or cylindrical geometry. By simplifying the material composition and the geometry, the properties of the fissile materials can be well characterized for future design considerations.

The present work focuses on a few very well known fast critical assemblies which began with the Topsy assembly [14] built in 1947. The Topsy assembly contributed some of the first basic fast-neutron fission chain information used for both weapon and fast-reactor design. Not only did the assembly provide information about criticality, critical masses and critical densities, information about the neutron distributions throughout the assembly, spectral indices and reactivity coefficients for various materials was studied as well. Many of the interesting integral quantities measured in these critical assemblies will be defined and introduced later when discussing radiation transport theory and the capabilities of some of the state-of-the-art computational tools available. A few of the subsequent fast critical assemblies built after the Topsy assembly will be the focus of the numerical results presented in this dissertation.

One of the first assemblies built after Topsy was the solid, bare, highly enriched uranium (HEU) sphere, Lady Godiva [15] seen in Fig 2.1. It was an unshielded reactor beginning operation in 1951 and ending operation in 1957, after the second

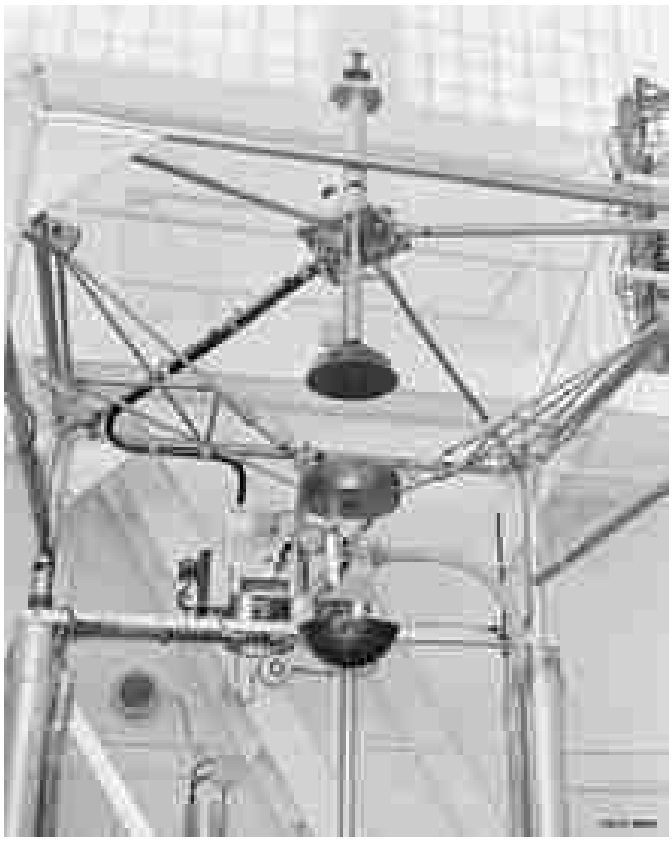

Figure 2.1: Lady Godiva Critical Assembly in a Scrammed Position.

excursion beyond prompt criticality led to many damaged components. The Lady Godiva assembly consisted of a sphere with a diameter of 17.483 cm, mass of 52.42 kg with the material composed of 93.71 wt.% ^{235}U, 5.27 wt.% ^{238}U, 1.02 wt.% ^{234}U and trace amounts of ^{236}U, C, Si and Fe. Because the critical radius of the HEU material was still unknown when designing the Lady Godiva experiment, a shell model was first constructed consisting of sets of nested hemispherical shells. With the information from the shell model the final Lady Godiva critical radius, density and volume was determined and the assembly seen in Fig. 2.1 could be finally manufactured. The Lady Godiva assembly provided a plethora of information about HEU beyond the criticality dimensions that would prove to be extremely useful for future reactor

designs that include HEU in fast-neutron environments.

The plutonium counterpart to the Lady Godiva assembly was the Jezebel assembly [16] built in 1954 composed of a solid, bare, delta-phase plutonium metal in a near spherical shape. In fact, the Jezebel assembly had three separate assemblies including two assemblies made of plutonium and one assembly made of uranium. The assembly known as the ^{239}Pu assembly was composed of 98.98 wt.% Pu and 1.02 wt.% Ga with negligible impurities from materials like C, O and Fe. The composition of the plutonium in the ^{239}Pu Jezebel was found to be 95.2 at.% ^{239}Pu, 4.5 at.% ^{240}Pu and 0.3 at.% ^{241}Pu. Because of the toxicity of plutonium, the components were all plated with nickel but the model used in the present work ignores the thin nickel plating. Although the Jezebel assembly included a couple of alternate assemblies including a ^{240}Pu (about 20.0 at.% ^{240}Pu) and a ^{233}U assembly, this present work will focus only on the original Jezebel assembly. Two configurations of the ^{239}Pu assembly were used to help establish the critical mass and density of an idealized plutonium sphere. With the two configurations including mass adjustment plugs, polar disks, control rods and the inherent pseudo-spherical shape, experimental measurements and careful analyses were used to calculate corrections necessary to convert the Jezebel assembly to a perfect sphere with a critical mass of 16.784 kg and a homogenized density of 15.60 g/cm^3.

Similar to the Jezebel assembly, the Flattop assembly [17] included several configurations including an HEU, ^{233}U and Pu metal core for operation. Built in the 1960's, unlike the previously studied pseudo-spherical assemblies, the Flattop assemblies were spherical in geometry and were surrounded by a thick, normal uranium metal reflector. The HEU core was comprised of two metal hemispheres and when joined together had a combined mass of 17.84 kg and average density of 18.62 g/cm^3 surrounded by a concentric normal uranium shell with a thickness of 18.01 cm and density of 19.0 g/cm^3. The composition of the HEU core was found to be 93.24 wt.%

^{235}U, 5.74 wt.% ^{238}U and 1.02 wt.% ^{234}U with the normal uranium shell composed of 99+ wt.% ^{238}U. The ^{233}U core was also comprised of two metal hemispheres of uranium metal highly enriched in ^{233}U instead of HEU, which is highly enriched in ^{235}U. After minor corrections were made to the original experiment, the idealized core has a mass of 5.74 kg and an average density of 18.42 g/cm^3 surrounded by the same normal uranium shell with a thickness of 19.91 cm. The core is composed of 98.13 wt.% ^{233}U, 1.24 wt.% ^{234}U, 0.60 wt.% ^{238} and 0.03 wt.% ^{235}U. Last, the Pu core will be studied and is composed of 93.80 wt.% ^{239}Pu, 4.80 wt.% ^{240}Pu and 0.30 wt.% ^{241}Pu with the remaining material in the core being 1.10 wt.% Ga. Once again, the delta-phase plutonium metal components were plated with nickel and assembled in a similar way the uranium cores were assembled. The final assembled core has a mass of 6.06 kg with an average density of 15.53 g/cm^3, once again being surrounded by the same normal uranium reflector material with a thickness of 19.609 cm.

The last critical assembly studied in this dissertation is the Big Ten critical assembly [18], which features a cylindrical core with an intermediate enrichment of uranium on average throughout the core. The assembly first attained criticality in 1971 and was named Big Ten because of its overall experimental mass of uranium (10 metric tons) and because the average ^{235}U enrichment within the core is 10%. This assembly differs substantially from the assemblies discussed previously. These assemblies were small with highly enriched materials in spherical geometries leading to the majority of neutrons in the assemblies being fast. The Big Ten assembly was designed to study cross sections of materials in an environment that had a slightly softer spectrum of neutrons and this requires the assembly to be larger to allow fast neutrons to interact with the reflecting parts of the assembly before leaking from the system. Within the Big Ten assembly, four different zones of uranium material were used including a 93 wt.% ^{235}U zone, a 10 wt.% ^{235}U zone, a natural uranium zone and a depleted uranium zone. The Big Ten assembly had several different configurations during its 25 year life but the present work will use a recognized and acceptable

model that has been homogenized in two sections throughout the core leading to a core with a somewhat balanced amount of each uranium isotope.

Originally, many of the experiments were developed to support the weapons program to study the neutronic behavior of highly enriched uranium and plutonium during delayed-critical, prompt-critical and superprompt-critical excursions [12]. After performing many fast burst criticality experiments, the work was later extended to include fundamental nuclear data research, biological studies, nuclear energy measurements and radiation damage effects. In fact, while the Lady Godiva [15] and the Jezebel [16] assemblies were built with the emphasis on weapons research, the Flattop [17] and the Big Ten [18] assemblies were built during the so-called "Rover" period with the emphasis placed on broader nuclear physics research with many new nuclear reactor designs in mind. Some of the interesting integral quantities that have been measured for each of the critical assemblies presented are the effective multiplication factor, the neutron leakage spectrum and the spectral indices of several important neutron-induced reactions. All of these original assemblies have been extensively studied and thanks to the wealth of knowledge gained from these assemblies, they have been used for future critical assembly design and especially in validating criticality calculations performed by neutron transport codes.

2.2 Neutron Transport Simulations

To model the critical assemblies faithfully the nuclear interactions taking place within the system must be well understood in order to reproduce the measured integral quantities. For this work we consider the time-independent linear Boltzmann transport equation in a multiplying medium that has been seen extensively in various textbooks [19, 20, 21, 22]. The assumptions made in the derivation of this form of the Boltzmann transport equation include: a fixed medium, Markov process for par-

ticle interactions (next event only depends on current state), particles are considered as points, particles do not interact with one another, relativistic effects are negligible, outside forces are neglected (i.e. gravity, magnetic field), material properties do not change as a consequence of particle interactions and stochastic effects are negligible. With these assumptions in mind, the transport equation can be described by:

$$\begin{aligned}
&\hat{\Omega}\cdot\nabla\psi(\vec{r},E,\hat{\Omega})+\Sigma_t(\vec{r},E)\psi(\vec{r},E,\hat{\Omega}) \\
&\quad=\int_0^\infty dE'\int_{4\pi} d\hat{\Omega}'\Sigma_s(\vec{r},E'\to E,\hat{\Omega}'\cdot\hat{\Omega})\psi(\vec{r},E',\hat{\Omega}') \\
&\quad+\frac{1}{4\pi}\frac{\bar{\nu}}{k}\int_0^\infty dE'\int_{4\pi} d\hat{\Omega}'\Sigma_f(\vec{r},E')\chi(\vec{r},E',E)\psi(\vec{r},E',\hat{\Omega}')\,,
\end{aligned} \tag{2.1}$$

$$\psi(\vec{r},E,\hat{\Omega})=0\,,\quad \text{if } \hat{\Omega}\cdot\hat{e}_S<0 \text{ for } \vec{r} \text{ on } S\,, \tag{2.2}$$

where S denotes the domain surface, $\hat{e}_s$ is the unit outward normal vector on the surface, and the boundary conditions given in Eq. (2.2) are known as vacuum boundary conditions. The variables that are solved in Eq. (2.1) include the k-eigenvalue and the angular flux, $\psi(\vec{r},E,\hat{\Omega})$, which is a function of spatial location, $\vec{r}$, energy, E, and direction vector, $\hat{\Omega}$. The first loss term on the left-hand-side is known as the streaming term expressed as the spatial divergence of the angular flux. The second loss term on the left-hand-side is the total collision operator where the total cross section of the material, $\Sigma_t(\vec{r},E)$, which is dependent on the space and energy variables, acts on the angular flux. This term describes the interactions of the neutral particles with the material that are subsequently removed from the phase space, $(\vec{r},E)$. The right-hand-side of Eq. (2.1) are the source terms that describe the neutral particles that are sourced into the phase space through some interaction with the media. The first source term is called the in-scatter term. This term describes the neutral particles integrated over the phase space variables, $(E',\hat{\Omega}')$, which interact with the material in a scattering collision described by the double-differential scattering cross section,

$\Sigma_s(\vec{r}, E' \rightarrow E, \hat{\Omega}' \cdot \hat{\Omega})$, and end up in the phase space of interest, $(\vec{r}, E, \hat{\Omega})$. The second source term is the fission source term and it describes the neutral particles integrated over the phase space variables, $(E', \hat{\Omega}')$, which interact with the material in a fissioning collision described by the fission cross section, $\Sigma_f(\vec{r}, E')$. After the fission occurs, there is an average number of neutral particles, $\bar{\nu}$, that are released in the fission event with an energy spectrum, $\chi(\vec{r}, E', E)$, leading to particles being sourced into the phase space of interest, $(\vec{r}, E, \hat{\Omega})$. The fission source term is scaled by the k-eigenvalue which is also known as the effective multiplication of the system and as the ratio of the number of neutrons in one generation to the number of neutrons in the previous generation. The effective multiplication factor values can be split into three categories:

$\mathbf{k < 1}$ describes a *subcritical* system where the asymptotic neutron population approaches zero in the absence of a fixed source,

$\mathbf{k = 1}$ describes a *critical* system where the neutron population remains constant due to the self-sustaining fission chain reaction,

$\mathbf{k > 1}$ describes a *supercritical* system where the neutron population diverges regardless of the presence of a source.

For the problems that are considered in the present work, the effective multiplication factor is studied along with the total leakage from the system and some important spectral indices. The k eigenvalue is computed directly in the solution of the transport equation. The remaining integral parameters studied here, including the total leakage and the spectral indices, are derived from the other solution resulting from the transport computation, the angular flux, $\psi(\vec{r}, E, \hat{\Omega})$. The total leakage

is defined by the relationship,

$$J = \int_S dA \int_0^\infty dE \int_{\hat{\Omega}\cdot\hat{e}_s>0} d\hat{\Omega}\ \hat{\Omega}\cdot\hat{e}_s\psi(\vec{r},E,\hat{\Omega})\,, \tag{2.3}$$

where $\hat{e}_s$ is once again the unit outward normal vector on the surface of the domain, S, and $\vec{r}_s$ denotes that the leakage is evaluated at the surface. This term describes the rate of neutrons leaving the domain and is an important measured quantity for any type of radiation transport application. The spectral indices are also derived from the angular flux, ψ, in the following manner:

$$\mathcal{I}^{(n)}(\vec{r}) = \frac{1}{N}\int_0^\infty dE \int_{4\pi} d\hat{\Omega}\ \Sigma^{(n)}(\vec{r},E,\hat{\Omega})\psi(\vec{r},E,\hat{\Omega})\,, \tag{2.4}$$

where $\Sigma^{(n)}(\vec{r},E,\hat{\Omega})$ is defined as a particular neutron-induced cross section for isotope n. The reason that this quantity is of interest is because the energy spectra seen in the angular flux affect these quantities in a substantial way depending on the critical assembly being studied. In order to measure a spectral index, specific materials are placed in or near the critical assembly and after the materials have been subjected to the angular flux within the experiment the measurements of each reaction take place. Generally, the N in Eq. (2.4) is defined as a similar reaction that is very well known and this allows the measurements of the spectral indices in many differing experiments to be compared in a reasonable fashion. In the present work the well known reaction will be defined with respect to the $\Sigma_f^{(^{235}U)}(\vec{r},E)$ cross section, because the neutron-induced fission reaction of ^{235}U is considered very well known and a "standard" in the ENDF/B nuclear data library [23]. In this work, the $\Sigma^{(n)}$ isotope will vary from $\Sigma_f^{(^{238}U)}$, $\Sigma_f^{(^{237}Np)}$ and $\Sigma_f^{(^{239}Pu)}$, but each will again be the associated fission cross section of each isotope. These reactions are of particular interest because both the ^{238}U and ^{237}Np fission reactions are threshold reactions that require a minimum neutron energy for the reactions to even occur, and the ^{239}Pu

fission reaction is also well known. Ultimately, the spectral index integral quantities studied in the present work are defined by,

$$\mathcal{I}^{(238f)}(\vec{r}) = \frac{1}{N(\vec{r})} \int_0^\infty dE \; \Sigma_f^{(^{238}U)}(\vec{r}, E)\phi(\vec{r}, E)\,, \tag{2.5}$$

$$\mathcal{I}^{(237f)}(\vec{r}) = \frac{1}{N(\vec{r})} \int_0^\infty dE \; \Sigma_f^{(^{237}Np)}(\vec{r}, E)\phi(\vec{r}, E)\,, \tag{2.6}$$

$$\mathcal{I}^{(239f)}(\vec{r}) = \frac{1}{N(\vec{r})} \int_0^\infty dE \; \Sigma_f^{(^{239}Pu)}(\vec{r}, E)\phi(\vec{r}, E)\,, \tag{2.7}$$

where the spectral indices are written shorthand with the $(238f)$ in Eq. (2.5) referring to the fission reaction of ^{238}U, for example. The $N(\vec{r})$ term in Eqs. (2.5)–(2.7) is defined as,

$$N(\vec{r}) = \int_0^\infty dE \; \Sigma_f^{(^{235}U)}(\vec{r}, E)\phi(\vec{r}, E)\,. \tag{2.8}$$

The scalar flux, $\phi(\vec{r}, E)$, in Eqs. (2.5)–(2.7) is defined as the angular flux integrated over all angles in $\hat{\Omega}$,

$$\phi(\vec{r}, E) = \int_{4\pi} d\hat{\Omega} \; \psi(\vec{r}, E, \hat{\Omega})\,. \tag{2.9}$$

By studying these spectral indices, particular information about the energy spectrum of the angular flux can be inferred based on the calculated quantities. In general, the fission cross sections in Eqs. (2.5)–(2.7) can be defined for any reaction the neutrons might undergo including capture, elastic and inelastic scattering, $(n, 2n)$, etc.

The transport equation can be posed in many other ways for various applications, but for this application the neutral particles of interest will be neutrons and the applications of interest include time-independent prompt critical systems where the

materials in the experiment are in a configuration such that they can maintain a self-sustaining chain reaction of fission events without the presence of an external source of neutrons. For materials like uranium and plutonium, the neutron-induced nuclear physics in the scattering cross section, fission cross section and the prompt fission neutron spectrum are very interesting with some complexities making it challenging to solve this integro-differential equation. First remember that this equation includes unknowns in both the k-eigenvalue as well as the angular flux, ψ. The most common way of solving this form of the transport equation is the so-called power iteration method [24, 25]. The power iteration method can be best described by first viewing the transport equation in Eq. (2.1) in operator notation,

$$(\mathbf{L}+\mathbf{T})\psi = \mathbf{S}\psi + \frac{1}{k}\mathbf{F}\psi\,, \tag{2.10}$$

where $\mathbf{L}$ is the streaming operator, $\mathbf{T}$ is the total collision operator, $\mathbf{S}$ is the scattering source operator, $\mathbf{F}$ is the fission source operator, k is the effective multiplication eigenvalue and ψ is the angular flux written shorthand which remains a function of the phase space variables, $(\vec{r}, E, \hat{\Omega})$. Rearranging Eq. (2.10) into an eigenvalue form,

$$\begin{aligned}
(\mathbf{L}+\mathbf{T}-\mathbf{S})\psi &= \frac{1}{k}\mathbf{F}\psi\,,\\
\psi &= \frac{1}{k}(\mathbf{L}+\mathbf{T}-\mathbf{S})^{-1}\mathbf{F}\psi\,,\\
\psi &= \frac{1}{k}\mathbf{M}\psi\,,
\end{aligned} \tag{2.11}$$

where the operator $\mathbf{M} = (\mathbf{L}+\mathbf{T}-\mathbf{S})^{-1}\mathbf{F}$. The power iteration method solves this problem by assuming the right-hand-side k and ψ are known and the left-hand-side ψ is solved by applying the $\mathbf{M}$ operator. The new ψ is used to compute a new k and the iteration continues until both quantities converge. The algorithm can be seen

here following an initial guess for $k^{(0)}$ and $\psi^{(0)}$,

$$\psi^{(n+1)} = \frac{1}{k^{(n)}}\mathbf{M}\psi^{(n)}\,, \tag{2.12}$$

$$k^{(n+1)} = k^{(n)}\frac{\left\langle F\psi^{(n+1)}\right\rangle}{\left\langle F\psi^{(n)}\right\rangle}\,, \tag{2.13}$$

where Eqs. (2.12) and (2.13) are repeated for N time until the conditions $||\psi^{(N+1)} - \psi^{(N)}|| < \epsilon$ and $|k^{(N+1)} - k^{(N)}| < \epsilon$ are satisfied, where ϵ is a user-defined convergence tolerance. The methods available for inverting the $(\mathbf{L} + \mathbf{T} - \mathbf{S})$ operator in Eq. (2.11) needed for each power iteration have been extensively studied over many years and are separated into three classes of techniques: deterministic, Monte Carlo and hybrid. Each category has its own advantages and disadvantages.

Deterministic methods are derived from the transport equation and involve discretizing the angular flux in each of the phase space variables including handling the differential and integral portions seen in Eq. (2.1) and then solving a large set of coupled equations. Deterministic methods are often computationally inexpensive and naturally provide solutions everywhere in the problem domain. However, these methods can have some disadvantages due to the approximations made when dealing with the spatial, energy and angular variables. Some disadvantages of using deterministic methods to solve the transport equation include inaccuracies in the computed integral quantities that can be caused by spatial truncation errors, angular quadrature order, polynomial expansion of the scattering cross section, energy group structure and ray effects, to name a few.

The Monte Carlo method for solving the transport equation was first brought to light by Von Neumann [26] in the 1940s with many subsequent developments and texts written [22, 27, 28]. Monte Carlo methods involve simulating the individual histories of radiation particles using random sequences of particle events and averaging over all event histories. The methodology relies on the facts that each individual

history is considered a Markov process and can be treated independently from all other histories, and as the number of histories gets very large the average quantities computed approach the true solution. The Monte Carlo method tries to avoid the discretization errors made by the deterministic methods by modeling the particle physics as faithfully as possible and the resulting solutions are generally referred to as the "exact" solution that other methods try to duplicate. A couple of the disadvantages of the Monte Carlo method include the inherent statistical noise introduced by the random sequences of events and the large computational cost required to solve problems with a complex phase space where the number of histories necessary may become large. Because of the nature of the Monte Carlo method, being that it is inherently parallelizable, the method can easily benefit from some of the very large computational multi-core clusters now available.

The final class of methods are the hybrid methods which have characteristics of both the deterministic and Monte Carlo methods, trying to utilize the advantages while limiting the inherent disadvantages each possess. Generally, the hybrid class of methods are application specific and will not be discussed any further in this dissertation.

Depending on what methods are used to solve the radiation transport problem, some modeling uncertainties or errors will be introduced. In the present work, when calculating the effective multiplication factor, the leakage and the spectral indices of each critical assembly, the Monte Carlo method is the method of choice. The MCNP5-1.60 code package [29, 30], a well established and respected Monte Carlo radiation transport code, is used to simulate all critical assemblies discussed previously.

Up to this point, most of the research toward the nuclear physics critical assemblies and the radiation transport codes has been on trying to exactly match the experimental measurements with the simulated results. Unfortunately this goal is

not as easy as it may seem. For example, the ICSBEP handbook [13] contains hundreds of the accepted benchmarks with a variety of materials and geometries. To obtain sufficient agreement between all of the benchmarks and the simulated results, the nuclear data going into the radiation transport codes, such as the cross sections, fission spectra and average multiplicity, has to be very well known. With the large amount of data and complexity, especially in the double-differential scattering cross section, matching every single benchmark is an extremely difficult task. Because of this difficulty, the uncertainties in the nuclear data libraries need attention so that we can begin to understand the sources of the discrepancies between the benchmarks and the simulations.

2.3 Nuclear Data Uncertainty

Recently, there has been an increased interest in the reactor physics community to include not only the evaluated values of nuclear data used in physics simulations but to also include the evaluated uncertainties associated with the nuclear data. The confidence in which the expected solution is known with respect to the nuclear data uncertainties is an important piece of information that can help in determining where future research efforts need to be focused. With the increased computer processing power available and newer and more sophisticated algorithms used in nuclear physics simulations, it is not sufficient to only calculate the expected solution anymore. Although errors do exist in nuclear physics simulations because of model imperfections, truncation errors and Monte Carlo noise among others, uncertainties in nuclear data need to be quantified.

Uncertainties in the expected values in the evaluated nuclear data libraries like ENDF/B-VII.1 [1] can come from many sources including experimental measurement uncertainties, theoretical model parameter uncertainties and the subsequent theoret-

ical model deficiencies. Quantifying the theoretical model deficiencies requires intimate knowledge of how the assumptions made while deriving the theoretical model affect the accuracy of the model predictions. Because the theoretical models are often derived from fundamental nuclear physics principles, uncertainties due to model deficiencies are very difficult to assess and beyond the scope of this research. Next we discuss the experimental data uncertainties and theoretical model parameter uncertainties.

Before discussing the experimental and model parameter uncertainties, some mathematical definitions of the uncertainties are introduced. In the present research, a probabilistic approach is used to describe the data uncertainties in the form of univariate and multivariate random variables. First, a single or univariate random variable $X(\omega)$ is completely characterized by the univariate probability density function, $P(X)dX$, describing the probability that $X(\omega)$ lies between X and $X + dX$ where the domain for X is finite and bounded by $X_{min} \leq X \leq X_{max}$. The moments of the univariate random variable are described by weighted integrals of the probability density function such that,

$$E[X^m] = \langle X^m \rangle = \int_{X_{min}}^{X_{max}} X^m P(X) dX \,, \tag{2.14}$$

where m is the order of the moment taken and $\langle \cdots \rangle$ denotes an ensemble average of the quantity inside. Note that the expectation or mean value of $X(\omega)$ is defined as the first moment where $m = 1$ in Eq. (2.14). From the moments of univariate random variable, the definition of the variance is,

$$\sigma^2 = E\Big[\left(X - E[X]\right)^2 \Big] = \int_{X_{min}}^{X_{max}} \Big(X - \langle X \rangle \Big)^2 P(X) dX \,, \tag{2.15}$$

where the standard deviation of the univariate random variable, σ, is simply the square root of the variance.

For a multivariate random variable, $\vec{x}(\omega) = \{x_1(\omega), x_2(\omega), \ldots x_N(\omega)\}$, the joint or multivariate probability density function, $P_N(\vec{x})d\vec{x}$, completely characterizes the random space where,

$$P_N(\vec{x})d\vec{x} = P_N(x_1, x_2, \ldots x_N)dx_1dx_2 \ldots dx_N \,, \tag{2.16}$$

is the probability that $x_1(\omega)$ lies between x_1 and $x_1 + dx_1$, $x_2(\omega)$ lies between x_2 and $x_2 + dx_2$, and continuing on to where $x_N(\omega)$ lies between x_N and $x_N + dx_N$. Analogous to the moments of the univariate random variable, a relationship exists describing the moments of multivariate random variables,

$$E[\vec{x}^{\,m}] = \langle \vec{x}^{\,m} \rangle = \int_{x_{1,min}}^{x_{1,max}} \cdots \int_{x_{N,min}}^{x_{N,max}} \vec{x}^{\,m} P_N(\vec{x})d\vec{x} \,, \tag{2.17}$$

where the vector multiplication is component-by-component and not interpreted as a dot product or cross product multiplication. The expectation or mean value for the multivariate random variable is defined in Eq. (2.17) when $m = 1$. From the moments of the multivariate random variable, the definition of the variance can be established by,

$$\vec{\sigma}^{\,2} = E\Big[(\vec{x} - E[\vec{x}])^2 \Big] = \int_{x_{1,min}}^{x_{1,max}} \cdots \int_{x_{N,min}}^{x_{N,max}} \Big(\vec{x} - \langle \vec{x} \rangle \Big)^2 P_N(\vec{x})d\vec{x} \,. \tag{2.18}$$

The standard deviation of the multivariate random variable, defined as the square root of the variance, $\vec{\sigma}$, gives insight into the amount of randomness coming from the second moment of the multivariate random variable in terms of the same units as the mean of the distribution.

When dealing with multivariate random variables defined by the joint probability density function, the correlations between the random vector component can be

characterized through the covariance matrix, which is a generalization of the notion for the variance. The individual components of the covariance matrix are defined by,

$$\begin{aligned}\mathbf{C}_{i,j} &= E\Big[\Big(x_i - E[x_i]\Big)\Big(x_j - E[x_j]\Big)\Big] \\ &= \int_{x_{i,min}}^{x_{i,max}} \int_{x_{j,min}}^{x_{j,max}} \Big(x_i - \langle x_i \rangle\Big)\Big(x_j - \langle x_j \rangle\Big) P_2(x_i, x_j) dx_j dx_i \end{aligned} \tag{2.19}$$

Of course, higher moments of the multivariate random variables can be defined, however, in the present work, the covariance matrix is used to describe all of the randomness in the nuclear data uncertainty. One final definition relating the uncertainties in a multivariate random variable is defined by the components of the correlation coefficient matrix,

$$\rho_{i,j} = \frac{\mathbf{C}_{i,j}}{\sqrt{\mathbf{C}_{i,i}\mathbf{C}_{j,j}}}\,, \tag{2.20}$$

where diagonal components of the covariance matrix normalize the covariance matrix such that the values of the components of the correlation coefficient matrix strictly range from -1 to 1.

In the present work, the covariance matrix is used to define the uncertainties in the quantity of interest and more importantly, define the way that the uncertainties interact with each other within a data set. The variance or standard deviation defines the total uncertainty for each data point in the data set. This information is useful for displaying the uncertainty information on a single graph using error bars to indicate the magnitude of uncertainty at each data point. Last, the correlation matrix strictly defines how the uncertainties within the data set interact with each other. If strong correlations exist, then fewer independent sources of uncertainty exist within the data set whereas if weak correlations exist, there are more independent sources of uncertainty.

The methods of computing an appropriate PFNS covariance matrix utilizing the uncertainties in experimental data and model parameters, and then analyzing and using the covariance matrix in a realistic application is a central theme of this dissertation. First, the potential sources of uncertainties are discussed at some length.

2.3.1 Experimental Data Uncertainties

Most of the experimental data used in this work were taken from the EXFOR experimental database [31]. Many of the datasets for the PFNS in the EXFOR database often only contain total uncertainties of the measurements while some might include a few individual sources of uncertainty coming from background interference, normalization measurements, etc. Experimental uncertainties have been categorized into three groups:

1. Short-energy-range (SER) uncertainties describe energy-dependent uncertainties that contribute to the overall uncertainty but do not interact between energies or energy bins. This would lead to a diagonal covariance matrix of partial uncertainties and an example of this type of uncertainty in nuclear data experiments is the statistical uncertainty from the number of counts in an energy bin. There may be correlations between neighboring bins due to bin sizing and uncertainty in the energy recorded, but in this work, the statistical uncertainty is considered to only contribute to the covariance in the diagonal elements.

2. Medium-energy-range (MER) correlations describe energy-dependent uncertainties that contribute not only to the total uncertainty but also contribute to the covariance matrix in the neighboring off diagonal terms. In the present work, the MER correlations are represented as a linear relationship for which

the correlations decrease from 100% to a minimum correlation given by some energy range parameters.

3. Long-energy-range (LER) correlations describe energy-independent uncertainties that contribute to the overall uncertainty in the form of a constant covariance matrix. This type of uncertainty is usually called the normalization uncertainty which will be identified by σ_N. Examples of LER correlations include target mass uncertainty, target geometry, sample self-absorption, etc.

By separating out all sources of uncertainty in experimental measurements, correlations can be computed more faithfully in this way. Recent work at the International Atomic Energy Agency (IAEA) [32] led to PFNS experimental correlation matrices using the GMA code [33] evaluated this way. The way that the correlation matrix is handled in GMA is best shown by an equation for the correlation matrix, $\rho_{i,j}$,

$$\rho_{i,j} = \frac{(\sigma_N)^2 + Q_{i,j}}{\sigma_i \sigma_j}\,, \tag{2.21}$$

where σ_i and σ_j are the total uncertainty at energy E_i and energy E_j, respectively,

$$\sigma_i = \sqrt{(\sigma_N)^2 + \sum_{k=1}^{K} \left(\sigma_i^k\right)^2}\,, \tag{2.22}$$

and the σ_i^k is the energy dependent uncertainty from source k. The source k can be from statistical uncertainty, background uncertainty, detector efficiency uncertainty, etc. To properly compute the $Q_{i,j}$ factor, some knowledge about how uncertainties interact with one another needs to be known. The counting statistics are considered SER correlations and they do not contribute to the $Q_{i,j}$ off diagonal terms. On the other hand, energy dependent uncertainty such as detector efficiency and background uncertainty should be included in the $Q_{i,j}$ off diagonal terms if the experimental

information is available. For the diagonal terms, $Q_{i,i}$ is given by,

$$Q_{i,i} = \sum_{k=1}^{K} \left(\sigma_i^k\right)^2 , \qquad \text{for} \quad i = j \, , \tag{2.23}$$

where K is the total number of uncertainty sources, and this definition ensures that the diagonal elements of the correlation matrix, $C_{i,i}$ are equal to unity. The off diagonal terms for $Q_{i,j}$ for energies that are far apart are given by,

$$Q_{i,j} = \sum_{k=1}^{K} \sigma_i^k \sigma_j^k a_k \left(a_k + b_k\right) , \quad \text{for} \quad i \neq j \quad \text{and} \quad |E_i - E_j| \geq b_k c_k E_i \, , \tag{2.24}$$

where the definitions for a_k, b_k and c_k determine the MER correlations with the minimum correlation defined by the choice of the $a_k \left(a_k + b_k\right)$ term. The remaining correlations that are not too far apart are computed linearly based on the energy difference between E_i and E_j,

$$Q_{i,j} = \sum_{k=1}^{K} \sigma_i^k \sigma_j^k \left(a_k + b_k\right) \left(a_k + b_k - \frac{|E_i - E_j|}{c_k E_i}\right) ,$$

$$\text{for} \quad i \neq j \quad \text{and} \quad |E_i - E_j| < b_k c_k E_i \, . \tag{2.25}$$

Determining what to choose for the a_k, b_k and c_k can be difficult especially when trying to correctly construct a correlation matrix of an older PFNS experiment. In recent IAEA work and the work presented here, the default values for the MER correlation coefficients have been, $a_k = b_k = c_k = 0.5$, given in the GMA code manual [33].

Many of the older PFNS experiments that have enough recorded details have been revisited by the IAEA [32]. The goal of that work has been to analyze known sources of uncertainty given by the experimentalists and to compute realistic covariance matrices of the experimental data to include in the EXFOR database. In

all of the results that follow, the experimental correlation matrices are either taken from the recent IAEA work where available or they are computed using the GMA code methodology extended to other experiments outlined in Eqs. (2.21)–(2.25) with the experimental uncertainties taken from the EXFOR database. Note that cross-experiment correlations, which do certainly exist, are not considered in this work, but should be the subject of future work.

2.3.2 Model Parameter Uncertainties

Another source of uncertainty present in evaluated nuclear data comes from the theoretical model parameters. Usually, a theoretical model will be derived with respect to a set of physical parameters that are either known to a certain degree from experimental measurement or from some derived systematics based on interpolation or extrapolation of similar experimental measurements. The reason that theoretical models are used in nuclear data evaluations is because in places where measurements are deficient or simply do not exist, theoretical models are used to predict the missing data. Here the theoretical model will be defined as a function, $f(\vec{x})$, which depends on the input parameters, $\vec{x}$.

Besides the uncertainties in the model parameters $\vec{x}$, deficiencies of the model $f(\vec{x})$ also exist. The theoretical model uncertainty is considered to be a deficiency in the model that cannot be propagated from the input parameter uncertainties. Although they do exist, because of the complex nature of the theoretical models, the theoretical model deficiencies will not be discussed any further and are a subject of future work.

In the present work, the input parameters, $\vec{x}$, are considered to have a covariance matrix, $\mathbf{X}$, including the uncertainties of the model parameters. The model parameters that are used in this work are all physically measurable quantities. Therefore,

the model parameters used in the present work have been researched independently of the prompt fission neutron spectrum (PFNS) and have been assigned some uncertainties. Because theoretical model deficiencies are not considered and we wish to allow the parameters more flexibility in order to match the experimental data, the uncertainties in the model parameter covariance matrix will be conservatively estimated allowing the experimental uncertainties to dominate the overall source of uncertainties.

2.4 The Prompt Fission Neutron Spectrum and Multiplicity

The average PFNS is defined as a probability distribution function, $\chi(E', E)$, describing the probability a neutron of energy E' induces a fission event with the emitted prompt fission neutrons with energy E. Linked closely to the PFNS is the average prompt fission neutron multiplicity (PFNM), $\bar{\nu}_p$, which is defined as the average number of prompt neutrons emitted in a fission event. The PFNM is presented here, but the majority of this work is dedicated to the PFNS with some current and future work focused on PFNM uncertainty quantification and propagation.

Presently, work is being done on developing a new model for prompt fission reactions using an advanced Monte Carlo Hauser-Feshbach (MCHF) model [34, 35], originally inspired by the work done by Browne and Dietrich [36]. The approach consists in following all possible fission fragment configurations and subsequent neutron cascades keeping track of the outcomes of each fission event. The MCHF model has the capability of calculating many more quantities associated with the prompt fission event as well as the average PFNS and average PFNM. It can also calculate the neutron multiplicity distribution, $P(\nu)$, the average neutron multiplicity as a function

of fragment mass and kinetic energy, $\bar{\nu}(A, KE)$, the PFNS for a given multiplicity, $\chi|_{\nu=\nu_o}$, and neutron-neutron energy and angular correlations.

The idea of the MCHF model is to follow all possible neutron and gamma ray cascades from all of the possible fission fragment yields of the fissioning nucleus. This means that one of the model parameters needed for the MCHF model calculation is the fission fragment mass yield. Some experimental measurements of the fission fragment mass yield exist for a few isotopes and incident neutron energies only and theoretical modeling is currently underway to provide a starting point for MCHF model calculations of other actinides [37]. From the total excitation energy of each of the fissioning fragments the emission of neutrons and gamma rays can be done through Monte Carlo sampling. If γ-rays are neglected, the neutrons are emitted sequentially until not enough excitation energy remains for neutron emission and the remaining excitation energy is given as the total emitted gamma ray energy. When neutrons are emitted, the Weisskopf spectrum [38] at the fission fragment temperature is randomly sampled from to give a neutron energy. The total excitation energy of the fission fragment is reduced by the binding energy and kinetic energy carried away by the neutron, and a subsequent neutron is released in the same way. The Monte Carlo process is repeated until sufficient sampling of the entire phase space is completed and the noise in the solution is within a desired range.

The advanced MCHF model has not been included in any of the ENDF/B-VII.0 data evaluations but major efforts are underway to use it in near future releases of the ENDF/B-VII library. With the amount of potential gains in knowledge of the fission reaction process especially with respect to the correlations between related fission reactions, this method should have a significant impact on the evaluation process related to nuclear fission reactions in future evaluation studies.

2.4.1 The Los Alamos Model

For the most important actinides, the ENDF/B-VII.1 [1] evaluations of PFNS are based on the Los Alamos (LA) or Madland-Nix model [39]. The LA model calculates the average neutron spectrum in the laboratory as a function of outgoing energy, $N(E)$ for a given incident neutron energy. An advantage of using the LA model for calculating the average PFNS is that the model contains very few tunable parameters. The most important are the average total kinetic energy of the fission fragment $\langle \mathrm{TKE} \rangle$, the average energy release $\langle E_r \rangle$, and the average level density parameter $\langle a \rangle$ which is used in calculating the maximum value of the temperature T_m related to the excitation energy distribution in the fragments.

In the laboratory frame, the average neutron energy spectrum is

$$N(E) = \frac{1}{2\sqrt{E}_f T_m^2} \int_{(\sqrt{E}-\sqrt{E}_f)^2}^{(\sqrt{E}+\sqrt{E}_f)^2} d\epsilon \sigma_c(\epsilon) \sqrt{\epsilon} \int_0^{T_m} dT k(T) T \exp(-\epsilon/T) \,, \tag{2.26}$$

where E_f is the fission fragment kinetic energy per nucleon and $k(T)$ is the temperature dependent normalization constant defined by

$$k(T)^{-1} = \int_0^{\infty} d\epsilon' \sigma_c(\epsilon') \epsilon' \exp(-\epsilon'/T) \,, \tag{2.27}$$

where $\sigma_c(\epsilon')$ is the energy-dependent cross section for the inverse process of compound nucleus formation. Assuming an equal number of neutrons are emitted from the light and heavy fragments, the average neutron energy spectrum in the laboratory frame is given as an average over the spectra for the light and heavy fragments,

$$N(E) = \frac{1}{2} \left[N_L(E) + N_H(E) \right] \,, \tag{2.28}$$

where the subscripts L and H identify the light and heavy fission fragment, respectively. While there is ample experimental evidence that $\bar{\nu}_L \neq \bar{\nu}_H$, we decided to keep the original assumption of the LA model for the present work. By providing two more parameters, the average neutron separation energy of the fission fragments $\langle S_n \rangle$ and the average total energy carried away through gamma-ray emission $\langle E_\gamma \rangle$, the average prompt fission neutron multiplicity, $\bar{\nu}$ can also be inferred. The average fission neutron multiplicity is calculated by

$$\bar{\nu} = \frac{\langle E_r \rangle + B_n + E_n - \langle \mathrm{TKE} \rangle - \langle E_\gamma \rangle}{\langle S_n \rangle + \langle \epsilon \rangle} \,, \tag{2.29}$$

where E_n is the energy of the incident neutron and $\langle \epsilon \rangle$ is the average energy of the spectrum in the center-of-mass frame.

Derivation of the model is based on nuclear evaporation theory [38] and is the result of averaging over the entire fission fragment distribution and neutron cascades. In the LA model, the fission fragment temperature distribution is assumed to be triangular starting from zero to a maximum value for the temperature, T_m, calculated from the average excitation energy, $\langle E^* \rangle = \langle E_r \rangle + E_n + B_n - \langle \mathrm{TKE} \rangle$, and the average level density parameter of the fission fragments, $\langle a \rangle$,

$$T_m = \sqrt{\frac{\langle E^* \rangle}{\langle a \rangle}} \,. \tag{2.30}$$

For each fission fragment pair, the distribution of the temperature is assumed to be the same, i.e. $T_{m,L} = T_{m,H}$.

Equation (2.26) was derived under the assumption that neutrons are evaporated isotropically in the center-of-mass reference frame of the fission fragments. If the fragments carry a large spin, it can be shown [40] that this assumption is no more valid, and that the prompt fission neutron spectrum in the center-of-mass should

read

$$\phi\left(\epsilon,\theta\right) \propto \phi\left(\epsilon\right)\left(1+b\cos^2\theta\right)\,, \tag{2.31}$$

where θ is the angle between the neutron and fission fragment directions. Equation (2.26) now becomes

$$\begin{aligned} N(E) = \quad & \frac{1}{2\sqrt{E}_f T_m^2}\frac{1}{1+b/3}\int_{(\sqrt{E}-\sqrt{E}_f)^2}^{(\sqrt{E}+\sqrt{E}_f)^2} d\epsilon\sigma_c(\epsilon)\sqrt{\epsilon}\times \\ & \left(1+b\frac{\left(E-\epsilon-E_f\right)^2}{4\epsilon E_f}\right)\int_0^{T_m} dT k(T) T\exp(-\epsilon/T)\,. \end{aligned} \tag{2.32}$$

In the present work, we have included the anisotropy coefficient b as a parameter.

2.4.2 Model Parameter Systematics

Usually, a theoretical model will be derived with respect to a set of physical parameters that are either known to a certain accuracy from experimental measurement or from some systematics, parameterized into a functional form derived from experiments as well. As mentioned earlier, the LA model has very few tunable parameters. Recently some of these parameters have been systematically evaluated by Tudora [41]. Specifically, the average total kinetic energy of the fission fragments $\langle\mathrm{TKE}\rangle$, the average energy release $\langle E_r\rangle$, and the average neutron separation energy of the fission fragments $\langle S_n\rangle$ at thermal energy were systematically estimated for the following actinides: $^{226-232}$Th, $^{224-233}$Pa, $^{229-238}$U, $^{231-237}$Np, $^{234-242}$Pu, and $^{240-245}$Am.

The following relations were obtained in [41]:

$$\langle \mathrm{TKE} \rangle_{th} = \alpha_1 + \alpha_2 \frac{Z^2}{A^{1/3}}\,, \quad \text{in [MeV]} \tag{2.33}$$

$$\langle E_r \rangle_{th} = \alpha_3 + \alpha_4 x(Z,A) + \alpha_5 x(Z,A)^2\,, \quad \text{in [MeV]}\,, \tag{2.34}$$

where x is the fissility parameter given by

$$x(Z,A) = \left(\frac{Z^2}{A}\right) / \left(50.883 \left(1 - 1.7826 \left(\frac{N-Z}{A}\right)^2\right)\right)\,, \tag{2.35}$$

and $N = A - Z$. The present work includes two additional model parameters. First, the average level density parameter, $\langle a \rangle$ is expressed in terms of the mass number, A,

$$\langle a \rangle = A/\alpha_6\,, \quad \text{in [MeV}^{-1}\text{]} \tag{2.36}$$

as in the original LA model [39]. As mentioned earlier, the anisotropy of the neutrons emitted from an excited fission fragment is now considered in our LA model calculations. In this work, the anisotropy coefficient, b, is also a parameter,

$$b = \alpha_7\,. \tag{2.37}$$

Utilizing the systematics evaluated by Tudora [41] in a data evaluation sense, allows the simultaneous evaluation of the uncertainties of a suite of actinides bringing consistency and cross-isotopes correlations, and more reliable extrapolations to neighboring nuclei for which no experimental data exist. This can be seen as an improvement to the present evaluations of the minor actinides in [1] of which some are still based on simple theoretical models and do not include evaluated covariance matrices.

Chapter 3

Uncertainty Quantification: Theory

With increased interest in nuclear data uncertainties, several collaborative efforts in the form of international workshops have taken place to present new research on uncertainty quantification methods and to present some practical results of the methods available [42, 43]. Some of the earliest methods of obtaining uncertainty information in the form of a covariance matrix were based largely on experimental data. In principle, if enough well documented experimental measurements have been taken, an adequate covariance matrix can be estimated. Using the generalized least-squares methodology, the GLUCS [44] code can be used to build a covariance matrix for a particular nuclear reaction from the experimental data sets. However, the resulting covariance matrices have been found to have very small off-diagonal components with large variances along the diagonal leading to very weak correlations between data points.

Many of the newer methods that are discussed in more detail here have been studied and implemented in the last 10 years or so. Much like the methods of solving

the transport problem discussed in Ch. 2.2, the contemporary methods of calculating nuclear data uncertainties fall into three categories: deterministic, Monte Carlo, and hybrid methods.

The deterministic methods are based on a Bayesian updating procedure that propagates prior model parameters and uncertainties by incorporating new knowledge from an experimental data set to obtain posterior evaluated model parameters and uncertainties, which are used to infer the evaluated nuclear reactions and uncertainties. Generally the deterministic methods require only a few theoretical model calculations and then apply the experimental data sets. Actually, in the updating procedure the uncertainties are quantified in the theoretical model parameter covariance matrix making it possible to then calculate a covariance matrix in the nuclear data phase-space using the theoretical model calculation. There are a few drawbacks of the deterministic methods including: the theoretical model calculation response is assumed to be linear with respect to a change in the model parameters, the resulting distribution of the parameters is assumed to be a multivariate Gaussian distribution, and the methods are limited to continuum quantities only. Similar to the Generalized Least Square Method (GLSM) [45], the Kalman filter [9, 46] has been a widely adopted deterministic method and will be discussed in more detail in the following section Ch. 3.1.

Stochastic or Monte Carlo methods do not generally have the same drawbacks the deterministic methods have. First, it is not necessary to assume the theoretical model response is linear with respect to a change in the input model parameters. Also, the stochastic methods are not limited to specific distributions of parameters and results, and they can handle discrete quantities unlike the deterministic methods. One drawback of many of the stochastic methods that has led to some criticism is the fact that many of the methods do not explicitly include experimental data.

One such stochastic method that does not explicitly include experimental data

is the "Filtered" Monte Carlo approach [47]. In this approach, implemented with the TALYS code [48], nuclear model uncertainties via the nuclear model parameters are propagated to the final evaluated uncertainties. The nuclear model parameter uncertainties are chosen such that the possible nuclear model calculations only span the spread of the existing experimental measurements for each reaction. Basically, the nuclear model parameters are sampled in a Monte Carlo fashion and if the nuclear model calculation falls outside of the existing experimental measurements, the sample is thrown away and another random sample is taken. After enough successful Monte Carlo samples, the average mean and covariance converge and a final evaluated mean and covariance for the parameters and model reactions are determined. This method has been used in building the nuclear data library TENDL [49] based solely on nuclear modeling with only partial use of the existing experimental data.

Instead of building the entire nuclear data library with means and covariances for all of the important nuclear reactions that can be used in nuclear physics simulations, the "Total" Monte Carlo method [11] has been suggested as an approach that propagates uncertainties in the model parameters all the way through the selected nuclear physics calculations. Each Monte Carlo sample of the model parameters that is accepted as in the Filtered Monte Carlo method is then used to calculate all theoretical model reactions, which are then used in selected nuclear physics calculations. This methodology provides an alternative to the usual ways of propagating uncertainties from a covariance matrix, i.e. sensitivity/perturbation methods and random sampling from decomposed covariances, by completely bypassing the evaluation of a covariance matrix and propagating uncertainties directly to nuclear physics calculations. The "Total" Monte Carlo approach has been employed for various applications including criticality studies [50], fast reactors [51] and fusion [52]. Although this methodology can be seen as an improvement over the traditional uncertainty propagation methods, the method still uses existing experimental data in an incomplete way, relying almost entirely on nuclear modeling.

Another stochastic method that has been developed is the Backward-Forward Monte Carlo method [53]. First, this method performs a Backward Monte Carlo step, which uses both the experimental data available and the model parameters to form a covariance matrix of the parameters. This is done by sampling from the independent parameters, computing the sample weight, which is based on a χ^2 estimate of the goodness of the model fit with experimental data, and then averaging the Monte Carlo samples to obtain a prior covariance matrix of the model parameters. Then, a Forward Monte Carlo step is taken, sampling from the computed parameter covariance and averaging the Monte Carlo samples to obtain the posterior covariance matrix of the parameters and theoretical model. This methodology uses the experimental data in a more formal way compared with the Filtered and Total Monte Carlo approaches using the experimental data as a more rigorous way to filter the sampling of the model parameters. An alternative stochastic approach, the Unified Monte Carlo method [10], capable of correctly handling experimental data is discussed in detail in Ch. 3.2.

The final category of methods used to evaluate nuclear data uncertainties falls under the class of hybrid methods. These methods make use of both deterministic and stochastic approaches trying to maximize the benefit of each and minimize their disadvantages. One such approach makes use of the GANDR code system [54]. Using the nuclear reaction code EMPIRE [55], Monte Carlo samples of the model parameters are used to obtain the prior mean values and covariances of several model reactions. These model reactions are then used in conjunction with the appropriate existing experimental data in a GLSM fit [45] to obtain the posterior reactions of interest. The advantages this method has over the previously discussed methods are that it allows the evaluation to include uncertainties for discrete quantities, e.g., spin and parity of discrete state, by Monte Carlo sampling through the EMPIRE code (not possible with deterministic methods) and it uses experimental data with the averaged model calculations in a rigorous sense through the GLSM fitting. Unfortunately, the

result of the evaluation only includes information about the posterior model reactions and nothing about the posterior model parameters.

3.1 Kalman Filter

In the context of nuclear data evaluations, the Kalman filter [9, 46] has been used to infer the best estimate of the central value and associated uncertainties of a nuclear reaction, a cross section for example [56, 57], combining experimental measurements and model predictions in a purely deterministic approach. The first-order Kalman filter most used in nuclear data evaluations can be derived from Bayes' theorem [58], expressed as

$$p(\vec{\mathbf{x}}) = AL(\phi, \mathbf{V}|\vec{\mathbf{x}})p_0(\vec{\mathbf{x}}|\vec{\mathbf{x}}_0, \mathbf{X})\,, \tag{3.1}$$

where $p(\vec{\mathbf{x}})$ is the posterior probability density function (PDF) of the parameters, $\vec{\mathbf{x}}$, L is the likelihood PDF, p_0 is the prior PDF, and A is the PDF normalization constant. The $\vec{\mathbf{x}}_0$ are the prior model parameters, $\mathbf{X}$ is the prior model parameter covariance matrix, ϕ is the experimental data and $\mathbf{V}$ is the experimental data covariance matrix. The normalization constant A is chosen such that the posterior PDF is normalized over the domain D of interest,

$$\int_D p(\vec{\mathbf{x}})d\vec{\mathbf{x}} = 1\,. \tag{3.2}$$

The Principle of Maximum Entropy [59, 60] states that the optimal choice for the shape of the likelihood and prior parameter PDF is a multivariate normal function or Gaussian distribution if the only knowledge of the prior parameters is the mean and the covariance matrix [45]. Therefore, the appropriate choice for the shape of

the prior parameter PDF and likelihood PDF would be,

$$p_0(\vec{\mathbf{x}}|\vec{\mathbf{x}}_0, \mathbf{X}) \sim \exp\left\{ -(1/2)\left[(\vec{\mathbf{x}} - \vec{\mathbf{x}}_0)^T \mathbf{X}^{-1} (\vec{\mathbf{x}} - \vec{\mathbf{x}}_0)\right] \right\}, \tag{3.3}$$

$$L(\phi, \mathbf{V}|\vec{\mathbf{x}}) \sim \exp\left\{ -(1/2)\left[(f(\vec{\mathbf{x}}) - \phi)^T \mathbf{V}^{-1} (f(\vec{\mathbf{x}}) - \phi)\right] \right\}, \tag{3.4}$$

where $f(\vec{\mathbf{x}})$ is the output of the theoretical model calculation given as a function of $\vec{\mathbf{x}}$. Substituting the definitions in Eqs. (3.3) and (3.4) into the Bayes' theorem in Eq. (3.1) results in the PDF of the posterior parameters,

$$\begin{aligned} p(\vec{\mathbf{x}}) &\sim \exp\left\{ -(1/2)[(f(\vec{\mathbf{x}}) - \phi)^T \mathbf{V}^{-1} (f(\vec{\mathbf{x}}) - \phi) + (\vec{\mathbf{x}} - \vec{\mathbf{x}}_0)^T \mathbf{X}^{-1} (\vec{\mathbf{x}} - \vec{\mathbf{x}}_0)] \right\} \\ &= \exp\left\{ -(1/2)[(\vec{\mathbf{x}} - \vec{\mathbf{x}}_1)^T \mathbf{P}^{-1} (\vec{\mathbf{x}} - \vec{\mathbf{x}}_1) \right\}, \end{aligned} \tag{3.5}$$

where the first assumption in deriving the Kalman filter comes from the assumptions for p_0 and L, requiring the posterior PDF of the parameters to be a Gaussian distribution with the knowledge of the posterior parameters, $\vec{\mathbf{x}}_1$, and the posterior covariance matrix, $\mathbf{P}$. Note that the maximum probability corresponds to the peak of the Gaussian distribution at $\vec{\mathbf{x}} = \vec{\mathbf{x}}_1$. As the second assumption made, the response of the model calculation, $f(\vec{\mathbf{x}})$, is taken to be a first-order Taylor series expansion about the prior model parameters such that,

$$f(\vec{\mathbf{x}}) \simeq f(\vec{\mathbf{x}}_0) + \mathbf{C}(\vec{\mathbf{x}} - \vec{\mathbf{x}}_0)\,, \tag{3.6}$$

where $\mathbf{C}$ is the sensitivity matrix whose coefficients are

$$C_{i,j} = \frac{\partial f(\vec{\mathbf{x}})_i}{\partial x_j}|_{\vec{\mathbf{x}}=\vec{\mathbf{x}}_0}\,, \tag{3.7}$$

where i refers to the i-th energy point of the model calculation and j refers to the j-th model parameter. The sensitivity matrix in Eq. (3.7) can be computed by a

simple numerical differencing around $\vec{\mathbf{x}}_0$,

$$C_{i,j} \sim \frac{f(\vec{\mathbf{x}}_0 + \delta x_j \hat{e}_j)_i - f(\vec{\mathbf{x}}_0 - \delta x_j \hat{e}_j)_i}{2\delta x_j}\,, \tag{3.8}$$

where δx_j is relatively small compared with the value of the associated prior parameter value in $\vec{\mathbf{x}}_0$, and $\hat{e}_j$ is a unit vector in the j-th row.

In Eq. (3.5), the arguments of the exponential terms can be equated such that:

$$(f(\vec{\mathbf{x}}) - \phi)^T \mathbf{V}^{-1} (f(\vec{\mathbf{x}}) - \phi) + (\vec{\mathbf{x}} - \vec{\mathbf{x}}_0)^T \mathbf{X}^{-1} (\vec{\mathbf{x}} - \vec{\mathbf{x}}_0) = (\vec{\mathbf{x}} - \vec{\mathbf{x}}_1)^T \mathbf{P}^{-1} (\vec{\mathbf{x}} - \vec{\mathbf{x}}_1)\,. \tag{3.9}$$

For convenience we define,

$$\begin{aligned} \vec{\mathbf{y}} &\equiv f(\vec{\mathbf{x}}_0) - \phi\,, \\ \tilde{\mathbf{x}}_0 &\equiv \vec{\mathbf{x}} - \vec{\mathbf{x}}_0\,, \\ \tilde{\mathbf{x}}_1 &\equiv \vec{\mathbf{x}}_1 - \vec{\mathbf{x}}_0\,. \end{aligned} \tag{3.10}$$

We can now rewrite Eq. (3.9) as:

$$(\vec{\mathbf{y}} + \mathbf{C}\tilde{\mathbf{x}}_0)^T \mathbf{V}^{-1} (\vec{\mathbf{y}} + \mathbf{C}\tilde{\mathbf{x}}_0) + \tilde{\mathbf{x}}_0^T \mathbf{X}^{-1} \tilde{\mathbf{x}}_0 = (\tilde{\mathbf{x}}_0 - \tilde{\mathbf{x}}_1)^T \mathbf{P}^{-1} (\tilde{\mathbf{x}}_0 - \tilde{\mathbf{x}}_1)\,, \tag{3.11}$$

using the linear assumption in Eq. (3.6). Reorganizing the terms in Eq. (3.12) leads to:

$$\begin{aligned} &\tilde{\mathbf{x}}_0^T (\mathbf{X}^{-1} + \mathbf{C}^T \mathbf{V}^{-1} \mathbf{C}) \tilde{\mathbf{x}}_0 + 2\vec{\mathbf{y}}^T \mathbf{V}^{-1} \mathbf{C} \tilde{\mathbf{x}}_0 + \vec{\mathbf{y}}^T \mathbf{V}^{-1} \vec{\mathbf{y}} \\ &\quad = \tilde{\mathbf{x}}_0^T \mathbf{P}^{-1} \tilde{\mathbf{x}}_0 - 2\tilde{\mathbf{x}}_1^T \mathbf{P}^{-1} \tilde{\mathbf{x}}_0 + \tilde{\mathbf{x}}_1^T \mathbf{P}^{-1} \tilde{\mathbf{x}}_1\,. \end{aligned} \tag{3.12}$$

Now, when the coefficients of the $\tilde{\mathbf{x}}_0^T\tilde{\mathbf{x}}_0$, $\tilde{\mathbf{x}}_0$ and constant terms in Eq. (3.12) are equated, the following relationships are found,

$$\tilde{\mathbf{x}}_0^T(\mathbf{X}^{-1} + \mathbf{C}^T\mathbf{V}^{-1}\mathbf{C})\tilde{\mathbf{x}}_0 = \tilde{\mathbf{x}}_0^T\mathbf{P}^{-1}\tilde{\mathbf{x}}_0\,, \tag{3.13}$$

$$2\vec{\mathbf{y}}^T\mathbf{V}^{-1}\mathbf{C}\tilde{\mathbf{x}}_0 = -2\tilde{\mathbf{x}}_1^T\mathbf{P}^{-1}\tilde{\mathbf{x}}_0\,, \tag{3.14}$$

$$\vec{\mathbf{y}}^T\mathbf{V}^{-1}\vec{\mathbf{y}} = \tilde{\mathbf{x}}_1^T\mathbf{P}^{-1}\tilde{\mathbf{x}}_1\,, \tag{3.15}$$

resulting in definitions for the posterior covariance matrix from Eq. (3.13) and the updated model parameters from Eq. (3.14) while the equality in Eq. (3.15) holds true. From Eqs. (3.13) and (3.14) the posterior covariance and parameter update are inferred,

$$\mathbf{P} = (\mathbf{X}^{-1} + \mathbf{C}^T\mathbf{V}^{-1}\mathbf{C})^{-1}\,, \tag{3.16}$$

$$\tilde{\mathbf{x}}_1 = -\mathbf{P}\mathbf{C}^T\mathbf{V}^{-1}\vec{\mathbf{y}}\,. \tag{3.17}$$

Replacing the variables in Eq. (3.17) with the definitions in Eq. (3.10) results in an expression for the posterior parameters,

$$\vec{\mathbf{x}}_1 = \vec{\mathbf{x}}_0 + \mathbf{P}\mathbf{C}^T\mathbf{V}^{-1}(\phi - f(\vec{\mathbf{x}}_0))\,. \tag{3.18}$$

The final Kalman filter equations after applying the matrix inversion properties, discussed in Appendix A, to Eqs. (3.16) and (3.18) result in the posterior model parameters and covariance matrix,

$$\vec{\mathbf{x}}_1 = \vec{\mathbf{x}}_0 + \mathbf{X}\mathbf{C}^T\left(\mathbf{C}\mathbf{X}\mathbf{C}^T + \mathbf{V}\right)^{-1}(\phi - f(\vec{\mathbf{x}}_0))\,, \tag{3.19}$$

$$\mathbf{P} = \mathbf{X} - \mathbf{X}\mathbf{C}^T\left(\mathbf{C}\mathbf{X}\mathbf{C}^T + \mathbf{V}\right)^{-1}\mathbf{C}\mathbf{X}\,. \tag{3.20}$$

The method that is generally employed to compute the final evaluated parameter central values and covariance matrix is to apply Eqs. (3.19) and (3.20) for each new

experimental dataset included in the analysis. First, the *a priori* values, $\vec{\mathbf{x}}_0$ and $\mathbf{X}$, are assumed to be known to some extent outside of the influence of the experimental data being used. With the experimental data, ϕ and $\mathbf{V}$, known, and having already computed the sensitivity coefficients, $\mathbf{C}$, Eqs. (3.19) and (3.20) are applied to obtain *a posteriori* values, $\vec{\mathbf{x}}_1$ and $\mathbf{P}$, for the model parameters. If more experimental data exist that should be used to constrain the model parameters, the *a posteriori* values are set as the *a priori* values and the same Eqs. (3.19) and (3.20) are used again albeit with a new experimental data set filling in the ϕ and $\mathbf{V}$ components. This method is generally referred to as the Bayesian updating technique because the updates are applied iteratively with different experimental data each time.

The final evaluated mean values and covariance matrix of the quantity of interest are given as

$$\Phi = f(\vec{\mathbf{x}}_1)\,, \tag{3.21}$$

$$\mathbf{F} = \mathbf{C}\mathbf{P}\mathbf{C}^T\,, \tag{3.22}$$

where Φ represents the evaluated mean model reaction and $\mathbf{F}$ represents the evaluated reaction covariance matrix. If the model is indeed linear, then the evaluated mean model reaction can be calculated by,

$$\Phi = f(\vec{\mathbf{x}}_0) + \mathbf{C}(\vec{\mathbf{x}}_1 - \vec{\mathbf{x}}_0)\,. \tag{3.23}$$

In the special case when experimental data is unavailable, the likelihood function would be equal to unity and the posterior PDF would assume the same shape as the prior PDF,

$$\begin{aligned} p(\vec{\mathbf{x}}) &\sim \exp\left\{-(1/2)[(\vec{\mathbf{x}} - \vec{\mathbf{x}}_0)^T\mathbf{X}^{-1}(\vec{\mathbf{x}} - \vec{\mathbf{x}}_0)]\right\} \\ &= \exp\left\{-(1/2)[(\vec{\mathbf{x}} - \vec{\mathbf{x}}_1)^T\mathbf{P}^{-1}(\vec{\mathbf{x}} - \vec{\mathbf{x}}_1)\right\}\,. \end{aligned} \tag{3.24}$$

In this situation, it is clear that the assumption the posterior parameters are distributed normally is no longer an assumption, but is a result of having no other experimental data to constrain the parameters. In order to satisfy Eq. (3.24) the posterior parameters and covariance matrix are equal to the prior parameters and covariance matrix,

$$\vec{\mathbf{x}}_1 = \vec{\mathbf{x}}_0\,, \tag{3.25}$$

$$\mathbf{P} = \mathbf{X}\,. \tag{3.26}$$

The posterior spectrum and covariance matrix calculated from Eqs. (3.21) and (3.22) are then,

$$\Phi = f(\vec{\mathbf{x}}_1) = f(\vec{\mathbf{x}}_0)\,, \tag{3.27}$$

$$\mathbf{F} = \mathbf{CPC}^T = \mathbf{CXC}^T\,, \tag{3.28}$$

equivalent to the prior spectrum and covariance matrix. This special case will be used when comparing the Kalman filter results with the Unified Monte Carlo (UMC) results for verification that the UMC method is implemented correctly.

3.2 Unified Monte Carlo

The Unified Monte Carlo method (UMC) [10] has been suggested as a potential alternative to the Generalized Least Squares (GLS) method used for nuclear data evaluations [10]. Some of the limitations and approximations associated with the GLS approach could be avoided by using the UMC approach. The UMC methodology results from applying Bayes' theorem in the form described in Eqs. (3.1) and (3.2). In this form, the PDF of posterior parameters can be written explicitly, but our interest is in calculating integral moments of the posterior PDF. The $\vec{x}$ values are

assumed to be random variable arguments centered about the prior parameter PDF. The mean value components of the posterior parameters $\vec{x}_1$ can be defined by,

$$\langle x_i \rangle = \frac{\int\limits_D x_i p(\vec{\mathbf{x}}) d\vec{\mathbf{x}}}{\int\limits_D p(\vec{\mathbf{x}}) d\vec{\mathbf{x}}} \,, \tag{3.29}$$

and the covariance matrix components for the posterior parameters P can be defined by,

$$P_{ij} = \left\langle \Big(x_i - \langle x_i \rangle \Big) \Big(x_j - \langle x_j \rangle \Big) \right\rangle = \left\langle x_i x_j \right\rangle - \left\langle x_i \right\rangle \left\langle y_j \right\rangle , \tag{3.30}$$

where the average values $\langle \cdots \rangle$ are obtained in Eq. (3.29).

Equation (3.5) is written without explicitly including the normalization constant, but in the implementation of the UMC method, the normalization, mean values and covariance matrix are calculated simultaneously, which is why Eq. (3.29) includes the normalization integral in the denominator. Our interest is in determining the mean and covariance of the parameters in Eqs. (3.29) and (3.30), respectively, and in calculating the mean and covariance of a given reaction, $\Phi(\vec{x})$,

$$\langle \Phi_i \rangle = \frac{\int\limits_D \Phi_i(\vec{\mathbf{x}}) p(\vec{\mathbf{x}}) d\vec{\mathbf{x}}}{\int\limits_D p(\vec{\mathbf{x}}) d\vec{\mathbf{x}}} \,, \tag{3.31}$$

$$F_{ij} = \frac{\int\limits_D \Phi_i(\vec{\mathbf{x}}) \Phi_j(\vec{\mathbf{x}}) p(\vec{\mathbf{x}}) d\vec{\mathbf{x}}}{\int\limits_D p(\vec{\mathbf{x}}) d\vec{\mathbf{x}}} - \langle \Phi_i \rangle \langle \Phi_j \rangle \,. \tag{3.32}$$

The solutions for the mean and covariance matrix for the parameters shown in Eqs. (3.29) and (3.30) and the mean and covariance for the spectrum in Eqs. (3.31) and (3.32) can be easily solved by Monte Carlo sampling from the domain of the prior parameters. For a Monte Carlo random history, k, the model parameters, $\vec{\mathbf{x}}_k$,

are randomly sampled in each individual component, where the i-th component of the model parameters is denoted as x_{ik}. Using these terms we can see that the continuous integral equations can be solved by Monte Carlo integration leading to the following equations for the evaluated parameters and spectrum, respectively,

$$\langle x_i \rangle = \lim_{K\to\infty} \left[\frac{\sum_{k=1}^{K} x_{ik} p(\vec{\mathbf{x}}_k)}{\sum_{k=1}^{K} p(\vec{\mathbf{x}}_k)} \right], \tag{3.33}$$

$$P_{ij} = \lim_{K\to\infty} \left[\frac{\left(\sum_{k=1}^{K} x_{ik} x_{jk} p(\vec{\mathbf{x}}_k) \right)}{\left(\sum_{k=1}^{K} p(\vec{\mathbf{x}}_k) \right)} - \langle x_i \rangle \langle x_j \rangle \right], \tag{3.34}$$

and,

$$\langle \Phi_i \rangle = \lim_{K\to\infty} \left[\frac{\sum_{k=1}^{K} \Phi_i(\vec{\mathbf{x}}_k) p(\vec{\mathbf{x}}_k)}{\sum_{k=1}^{K} p(\vec{\mathbf{x}}_k)} \right], \tag{3.35}$$

$$F_{ij} = \lim_{K\to\infty} \left[\frac{\left(\sum_{k=1}^{K} \Phi_i(\vec{\mathbf{x}}_k) \Phi_j(\vec{\mathbf{x}}_k) p(\vec{\mathbf{x}}_k) \right)}{\left(\sum_{k=1}^{K} p(\vec{\mathbf{x}}_k) \right)} - \langle \Phi_i \rangle \langle \Phi_j \rangle \right], \tag{3.36}$$

where $p(\vec{\mathbf{x}})$ is calculated as the product of the exact prior parameter and likelihood PDFs in Eqs. (3.3) and (3.4), respectively.

This UMC methodology has been used and compared against the traditional GLS method for some simple examples with few input values only [10]. For the set of simple examples, both the brute force (BF) Monte Carlo method and the

Metropolis (METR) algorithm developed by Metropolis *et al.* [61] and later generalized by Hastings [62] were used to compute the mean and covariance shown in Eqs. (3.33) and (3.34). Although the METR algorithm performed much better in convergence and computation time, the authors concluded that the BF approach was better suited for realistic applications, while the METR algorithm needs additional work to be efficient for a variety of applications [10].

To directly compare the Kalman filter with the UMC method, the assumption that the theoretical model response is linear will be made for verification purpose only in the context of the UMC integral equations. Using the definitions in Eq. (3.10), with the linear assumption of the model response, the posterior PDF takes a familiar form,

$$p(\vec{\mathbf{x}}) = \exp\left\{-\frac{1}{2}\left[\tilde{\mathbf{x}}_0^T\mathbf{X}^{-1}\tilde{\mathbf{x}}_0 + (\vec{\mathbf{y}}+\mathbf{C}\tilde{\mathbf{x}}_0)^T\mathbf{V}^{-1}(\vec{\mathbf{y}}+\mathbf{C}\tilde{\mathbf{x}}_0)\right]\right\}. \tag{3.37}$$

Expanding the terms in the exponential function while separating some of the exponential terms leads to,

$$\begin{aligned} p(\vec{\mathbf{x}}) &= \exp\left\{-\frac{1}{2}\left[\tilde{\mathbf{x}}_0^T(\mathbf{X}^{-1}+\mathbf{C}^T\mathbf{V}^{-1}\mathbf{C})\tilde{\mathbf{x}}_0 + \vec{\mathbf{y}}^T\mathbf{V}^{-1}\mathbf{C}\tilde{\mathbf{x}}_0 + \tilde{\mathbf{x}}_0^T\mathbf{C}^T\mathbf{V}^{-1}\vec{\mathbf{y}}\right]\right\} \\ &\quad \times \exp\left\{-\frac{1}{2}\left[\vec{\mathbf{y}}^T\mathbf{V}^{-1}\vec{\mathbf{y}}\right]\right\}. \end{aligned} \tag{3.38}$$

Notice the second exponential term in Eq. (3.38) does not depend on the integration variables in Eq. (3.29), therefore it can be moved outside the integral in both the numerator and denominator, canceling each other out in both the definitions of the mean and covariance. Before doing so, we multiply and divide Eq. (3.38) by a useful exponential term,

$$\begin{aligned} &\exp\left\{-\frac{1}{2}\left[\vec{\mathbf{y}}^T\mathbf{V}^{-1}\mathbf{C}\left(\mathbf{X}^{-1}+\mathbf{C}^T\mathbf{V}^{-1}\mathbf{C}\right)^{-1}\mathbf{C}^T\mathbf{V}^{-1}\vec{\mathbf{y}}\right]\right\} \\ &\quad = \exp\left\{-\frac{1}{2}\left[\vec{\mathbf{y}}^T\mathbf{V}^{-1}\mathbf{C}\mathbf{Q}\mathbf{C}^T\mathbf{V}^{-1}\vec{\mathbf{y}}\right]\right\}, \end{aligned} \tag{3.39}$$

where $\mathbf{Q} = \left(\mathbf{X}^{-1} + \mathbf{C}^T\mathbf{V}^{-1}\mathbf{C}\right)^{-1}$ is defined for convenience at this point. In applying this exponential term and using the definition for $\mathbf{Q}$, the first exponential term in Eq. (3.38) can be compressed resulting in,

$$\begin{aligned} p(\vec{\mathbf{x}}) &= \exp\left\{-\frac{1}{2}\left[\left(\tilde{\mathbf{x}}_0 + \vec{R}\right)^T \mathbf{Q}^{-1}\left(\tilde{\mathbf{x}}_0 + \vec{R}\right)\right]\right\} \\ &\quad \times \exp\left\{-\frac{1}{2}\left[\vec{\mathbf{y}}^T\mathbf{V}^{-1}\vec{\mathbf{y}}\right]\right\} \exp\left\{\frac{1}{2}\left[\vec{\mathbf{y}}^T\mathbf{V}^{-1}\mathbf{C}\mathbf{Q}\mathbf{C}^T\mathbf{V}^{-1}\vec{\mathbf{y}}\right]\right\}, \end{aligned} \tag{3.40}$$

where $\vec{R} = \mathbf{Q}\mathbf{C}^T\mathbf{V}^{-1}\vec{\mathbf{y}}$ is defined for convenience. This modified version of the posterior PDF in Eq. (3.40) is inserted into the exact integrals for the mean and covariance. Note that the final two exponential terms in Eq. (3.40) are independent from the variables of integration in the moment equations and are now cancelled out. The resulting equations for the components of the mean and covariance, given the linear model assumption and given that the domain D spans from $-\infty$ to ∞, can be seen as,

$$\langle \tilde{x}_i \rangle = \frac{\int_{-\infty}^{\infty} \cdots \int_{-\infty}^{\infty} \tilde{x}_{0,i} \exp\left\{-\frac{1}{2}\left[\left(\tilde{\mathbf{x}}_0 + \vec{R}\right)^T \mathbf{Q}^{-1}\left(\tilde{\mathbf{x}}_0 + \vec{R}\right)\right]\right\} d\tilde{\mathbf{x}}_0}{\int_{-\infty}^{\infty} \cdots \int_{-\infty}^{\infty} \exp\left\{-\frac{1}{2}\left[\left(\tilde{\mathbf{x}}_0 + \vec{R}\right)^T \mathbf{Q}^{-1}\left(\tilde{\mathbf{x}}_0 + \vec{R}\right)\right]\right\} d\tilde{\mathbf{x}}_0}, \tag{3.41}$$

and,

$$P_{i,j} = \frac{\int_{-\infty}^{\infty} \cdots \int_{-\infty}^{\infty} \tilde{x}_{0,i}\tilde{x}_{0,j} \exp\left\{-\frac{1}{2}\left[\left(\tilde{\mathbf{x}}_0 + \vec{R}\right)^T \mathbf{Q}^{-1}\left(\tilde{\mathbf{x}}_0 + \vec{R}\right)\right]\right\} d\tilde{\mathbf{x}}_0}{\int_{-\infty}^{\infty} \cdots \int_{-\infty}^{\infty} \exp\left\{-\frac{1}{2}\left[\left(\tilde{\mathbf{x}}_0 + \vec{R}\right)^T \mathbf{Q}^{-1}\left(\tilde{\mathbf{x}}_0 + \vec{R}\right)\right]\right\} d\tilde{\mathbf{x}}_0} - \langle \tilde{x}_i \rangle \langle \tilde{x}_j \rangle . \tag{3.42}$$

Shown in Appendix B the solutions to the exponential integrals in Eqs. (3.41) and (3.42) are,

$$\begin{aligned} \langle \tilde{\mathbf{x}} \rangle &= -\vec{R} \\ &= -\left(\mathbf{X}^{-1} + \mathbf{C}^T\mathbf{V}^{-1}\mathbf{C}\right)^{-1} \mathbf{C}^T\mathbf{V}^{-1}\vec{\mathbf{y}}, \end{aligned} \tag{3.43}$$

and,

$$\begin{aligned} \mathbf{P} &= \mathbf{Q} \\ &= \left(\mathbf{X}^{-1} + \mathbf{C}^T\mathbf{V}^{-1}\mathbf{C}\right)^{-1} . \end{aligned} \tag{3.44}$$

Finally cleaning up the expressions and inserting the original variables back into Eq. (3.43) we see,

$$\vec{\mathbf{x}}_1 = \vec{\mathbf{x}}_0 + \mathbf{P}\mathbf{C}^T\mathbf{V}^{-1}(\phi - f(\vec{\mathbf{x}}_0)) , \tag{3.45}$$

where Eqs. (3.45) and (3.44) are identical to the results found in deriving the Kalman filter in Eqs. (3.18) and (3.16), respectively. In fact, this approach can be seen as an alternate method for deriving the Kalman filter equations directly.

This is an important result, especially when testing the implementation of the UMC method. In Ch. 4.2, we will check that when the linear model assumption is enforced in the context of the UMC algorithm, the UMC results toward the Kalman filter results with or without the use of the direct experimental data. Chapter 4.2.1 discusses the implementation details of the UMC method, and the linear model assumption while including or excluding experimental data to study the UMC convergence properties.

It is important to note that the posterior values obtained in the Kalman filter correspond to the function peak, while the posterior values obtained in the UMC method correspond to the true mean of the underlying posterior PDF. In deriving the Kalman filter, a normal distribution is assumed for the posterior PDF in Eq. (3.5). In the case where direct measurements of the nuclear reaction being considered are the only experimental data included and the theoretical model response is linear, the Kalman filter assumption is exact and the UMC results (given sufficient sampling of the prior PDFs) would be the same as the Kalman filter results. When indirect

experimental data, like ratio data or integral data, are included in the evaluation, the posterior PDF will be skewed (shifting the mean away from the peak) and the UMC method will result in a more appropriate estimate for the posterior parameters and covariance matrix. This will be important when comparing Kalman and UMC results. In Ch. 4.2 the UMC implementation details will be discussed in the context of a realistic PFNS evaluation compared with the Kalman filter.

Chapter 4

Uncertainty Quantification: Numerical Results

One of the major improvements made to the ENDF/B-VII.0 [63] nuclear data library released in 2006 is the inclusion of a significant number of evaluated nuclear data uncertainties. In fact, the newly released ENDF/B-VII.1 [1] library contains 423 neutron-induced evaluations of which 190 include covariance matrices. Some of the covariances included in the new library release span many different reaction channels and types including the most important cross sections, secondary particle energy spectra, prompt fission neutron spectra, and prompt fission neutron multiplicity [57].

The prompt fission neutron spectrum (PFNS) uncertainty evaluations that were released in the ENDF/B-VII.1 library include, but are not limited to, the neutron-induced fission reactions on ^{235}U, ^{238}U, ^{238}Pu and ^{239}Pu below the second-chance fission threshold. Of the evaluated PFNS covariance matrices mentioned, the PFNS for the ^{238}Pu(n,f) reaction is the only one that has been evaluated using the Kalman filter without differential experimental data to help constrain the model parameters. In fact, differential experimental data of the PFNS for the ^{238}Pu(n,f) reaction has

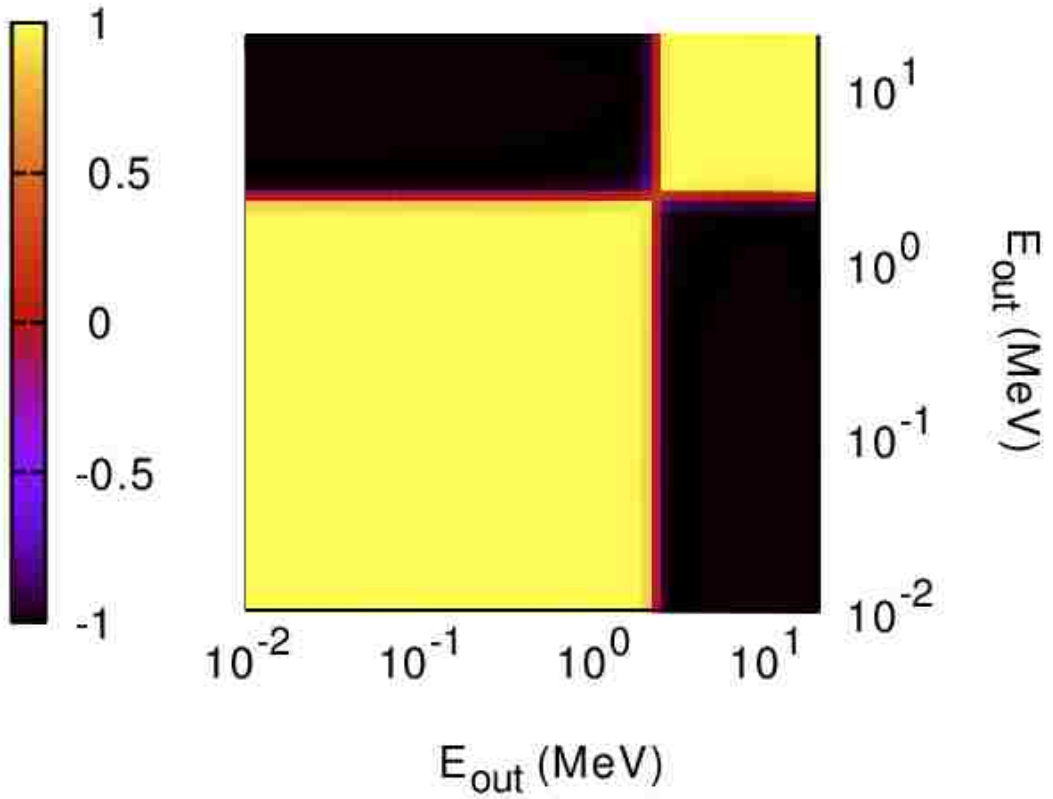

Figure 4.1: The correlation matrix of the PFNS for the n(0.5 MeV)+^{238}Pu fission reaction in the ENDF/B-VII.1 nuclear data library [1]. The clear two-block pattern seen is the result of the probability distribution properties of the PFNS based only on the model calculations.

never been measured or published, making it difficult to reasonably evaluate the reaction as well as the uncertainties using only the theoretical model. Figure 4.1 shows the results of the n+^{238}Pu PFNS covariance evaluation included in the ENDF/B-VII.1 library. The shape of the n+^{238}Pu covariance matrix has two very distinct regions of correlation and anti-correlation because it is based purely on model predictions and the linear model assumption.

4.1 Actinide Suite Evaluation

The recent work in [64, 65] has been done to remedy the fact that the minor actinides have scarce experimental data available making it difficult to evaluate the mean values and covariance matrices consistently with the major actinides. In the present work each actinide evaluation of the PFNS across a suite of isotopes uses the same values of the LA model parameters, α_i for $i = 1, ..., 7$, defined previously in Eqs. (2.33)–(2.34) and (2.36)–(2.37). Note that the α_i for $i = 1, ..., 5$, in the present work have been altered from their original values given by Tudora [41] by shifting the origin of the systematics to a reference isotope that is likely to have the smallest uncertainty for each actinide (e.g. ^{235}U for uranium isotopes, ^{239}Pu for plutonium isotopes, etc.). As an example,

$$\langle \mathrm{TKE} \rangle_{th} = \hat{\alpha}_1 + \hat{\alpha}_2 \left[\frac{Z^2}{A^{1/3}} - \frac{Z_0^2}{A_0^{1/3}} \right], \quad \text{in [MeV]}, \tag{4.1}$$

$$\begin{aligned} \langle E_r \rangle_{th} &= \hat{\alpha_3} + \hat{\alpha}_4 \left[x(Z, A) - x(Z_0, A_0) \right] \\ &+ \hat{\alpha}_5 \left[x(Z, A) - x(Z_0, A_0) \right]^2, \quad \text{in [MeV]}, \end{aligned} \tag{4.2}$$

where the fissility parameter, $x(Z, A)$, is defined in Eq. (2.35) and the same shape of the systematics exist now centered around the isotope (Z_0, A_0). For simplicity, the parameters used in the remainder of this document will assume the definition $\alpha_i = \hat{\alpha}_i$ for $i = 1, ..., 5$, such that each reference to the parameters henceforth will be assumed to be defined in Eqs. (4.1) and (4.2).

The posterior parameters and uncertainties are obtained using the Kalman filter in Eqs. (3.19) and (3.20) using the differential experimental data available in the EXFOR database [31] and the LA model calculations. In Tables 4.1 and 4.4 where the IAEA work [32] is cited, the dataset that is used in this work is the "corrected" dataset from the IAEA calculated in the same fashion outlined in Ch. 2.3.1 using

the GMA methodology [33]. In most cases, the "corrected" dataset is a modified version of the original where the central values are only slightly changed, if at all, and the uncertainties and calculated correlations have been adjusted to account for uncertainties that the experimentalists did not include in the original work or EXFOR entry. In all other cases, the dataset that is used in this work is taken directly from the EXFOR database and the correlation matrix is computed using the GMA methodology.

4.1.1 Uranium 229-238

The uranium suite of isotopes has the most PFNS experimental measurements in the EXFOR database as well as some of the most recent measurements [67, 68]. The differential data listed in Table 4.1 are used to constrain the parameters and associated uncertainties in the present evaluation work. In the cases where the experimental data are also cited by the IAEA work [32], the IAEA results were used in place of the original EXFOR entries.

Figures 4.2 and 4.3 show the prior parameter values and posterior parameter values across the entire suite of uranium actinides for the average total kinetic energy and energy release, respectively. Plotted along with the prior and posterior systematics are the parameter values calculated by Madland for the n(thermal)+^{235}U, n(thermal)+^{238}U, and n(thermal)+^{239}Pu reactions [80]. Note that the prior uncertainties are shaded in light red and are chosen to be large enough to allow the model parameters to explore a large but reasonable parameter space. Note that the slopes of the prior and posterior systematics differ slightly due to the inclusion of experimental data of multiple uranium isotopes.

The prior values for $\alpha_1 - \alpha_6$ are calculated from the systematics given by Tudora [41] and the prior value and prior uncertainty for α_7 is taken to be within

Mass # (A)	First Author	Date	E_{inc} (MeV)	E_{out} (MeV)	EXFOR Entry	Ref.
233	Miura	2002	0.55	0.7-12.1	22688-002	[69]
233	Lajtai	1985	thermal	0.03-3.855	30704-002	[70]
233	Starostov	1985	thermal	0.83-9.3	40930-004	[71, 32]
233	Boytsov	1983	thermal	0.025-4.6	40873-002	[72, 32]
235	Kornilov	2010	thermal	0.68-11.8	31692-002	[67, 32]
235	Vorobyev	2010	thermal	0.21-10.8	41516-017	[68, 32]
235	Staples	1995	0.5-3.5	0.596-16.772	13982-002	[73]
235	Boikov	1991	2.9	0.232-11.885	41110-009	[74]
235	Wang	1989	thermal	0.58-12.3	32587-002	[75, 32]
235	Lajtai	1985	thermal	0.025-4.0	30704-003	[70, 32]
235	Starostov	1985	thermal	0.085-12.3	40930-006	[71, 32]
235	Boytsov	1983	thermal	0.025-4.6	40873-004	[72, 32]
235	Johansson	1977	0.53	0.625-14.45	20175-003	[76]
235	Adams	1975	0.52	0.625-15.629	20996-003	[77]
238	Trufanov	2001	5.0	0.28-12.27	41450-003	[78]
238	Boikov	1991	2.9	0.232-11.885	41110-010	[74]
238	Baba	1989	2.0	2.5-12.87	22112-002	[79]

Table 4.1: Experimental measurements of the PFNS for the neutron-induced $^{229-238}$U fission reactions used in the present work including work from both the EXFOR database [31] and modified data from the IAEA PFNS experimental data [32].

one standard deviation of the value proposed in the original anisotropy work by Ericson [40]. The prior and posterior parameters along with their uncertainties are summarized in Table 4.2. For α_4 and α_5 the relative uncertainty increased from the prior uncertainty given due to the increase in the parameter value. In terms of the behavior of the absolute uncertainty, we expect the uncertainty to decrease or remain unchanged when using the differential experimental data to constrain the model parameters.

The prior parameters are uncorrelated, i.e. diagonal covariance matrix based on the chosen prior uncertainties, and the posterior parameter correlations resulting from applying the Kalman filter (Eq. (3.20)) are given in Table 4.3. The average

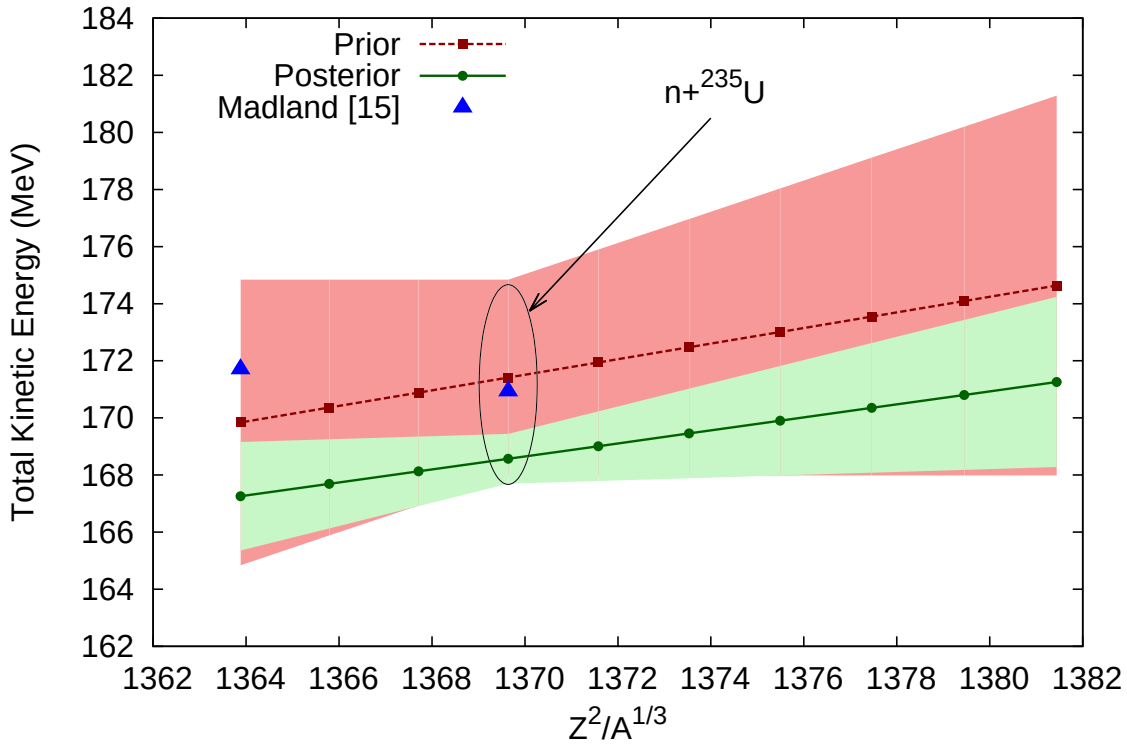

Figure 4.2: The prior and posterior average total kinetic energy of the fission fragments of the n+$^{229-238}$U PFNS plotted with calculations done by Madland [80].

Parameter		Prior Value	Prior Uncertainty (%)	Posterior Value	Posterior Uncertainty (%)
$\langle$TKE$\rangle$	α_1	171.41	2.0	168.57	0.52
—	α_2	0.273	100.0	0.228	78.29
$\langle E_r \rangle$	α_3	187.85	6.0	185.13	0.37
—	α_4	784.34	50.0	442.21	63.56
—	α_5	25586	25.0	20783	30.04
C	α_6	11.000	4.0	10.094	3.78
b	α_7	0.100	50.0	0.098	16.04

Table 4.2: Parameters of the LA model evaluation of the n+$^{229-238}$U PFNS, where $\alpha_1 - \alpha_6$ are in MeV and α_7 is dimensionless.

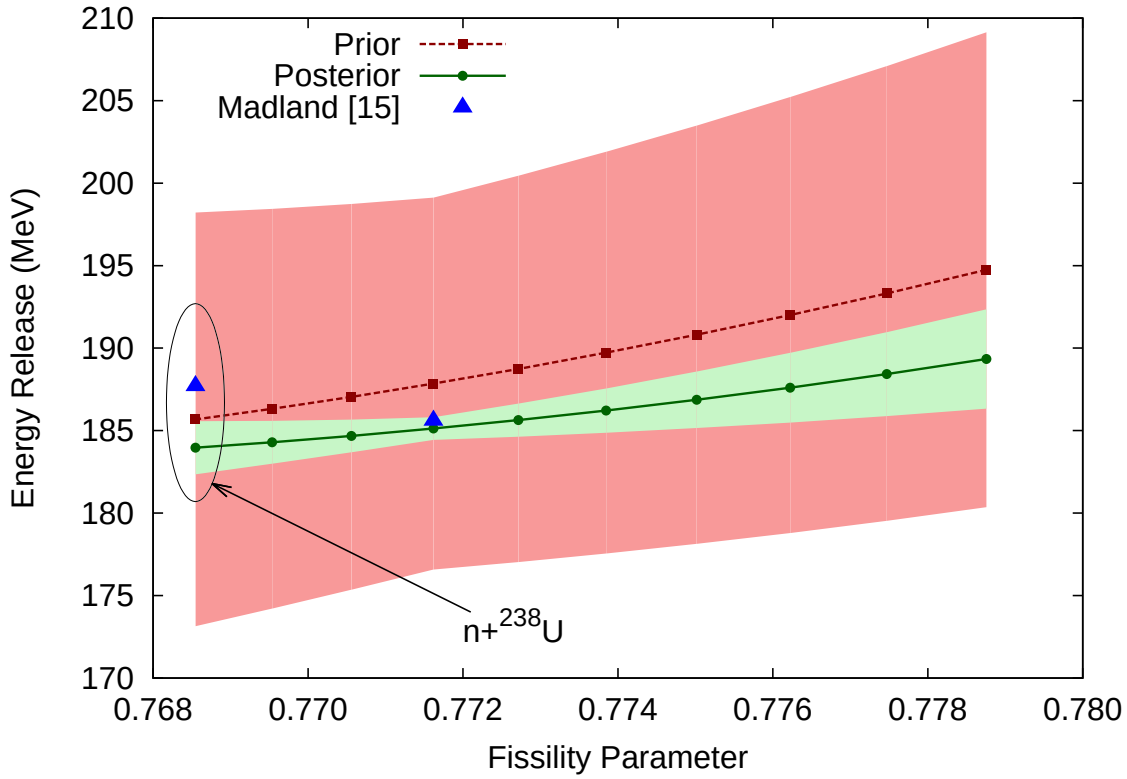

Figure 4.3: The prior and posterior average energy release of the n+$^{229-238}$U PFNS plotted with calculations done by Madland [80].

total kinetic energy and the average energy release show a strong correlation seen in the calculated correlations between the α_1 and α_3 terms and the α_2 and α_4 terms. This result has been seen in previous work including the recent evaluation of n(0.5 MeV)+^{239}Pu uncertainties [66]. It is expected as the average excitation energy $\langle E^* \rangle$ appearing in Eq. (2.30) is mostly determined by the difference between $\langle E_r \rangle$ and $\langle \text{TKE} \rangle$. To keep $\langle E^* \rangle$ nearly constant, $\langle E_r \rangle$ and $\langle \text{TKE} \rangle$ have to be strongly correlated. It also follows from the Kalman filter that the level density parameter, α_6, is correlated with the dominant average total kinetic energy term, α_1, and is anti-correlated with the dominant average energy release term, α_3. Once again, to keep the T_m calculation in Eq. (2.30) nearly constant, the α_6 parameter needs to be

anti-correlated with the $\langle E_r \rangle$ term and correlated with the $\langle \text{TKE} \rangle$ term. Lastly, it is observed that the anisotropy parameter, α_7, is moderately correlated with both the average total kinetic energy and the average energy release. The remaining parameter, α_5, has a very weak correlation with all of the other parameters in this study.

Parameter	α_1	α_2	α_3	α_4	α_5	α_6	α_7
α_1	100						
α_2	-1	100					
α_3	36	0	100				
α_4	-3	97	0	100			
α_5	-3	-4	0	-2	100		
α_6	61	-1	-50	-2	-3	100	
α_7	25	0	7	-2	-1	11	100

Table 4.3: Posterior parameters correlations of the LA model evaluation of the n+$^{229-238}$U PFNS.

From the posterior parameters listed in Table 4.2 and the posterior parameter correlation matrix in Table 4.3 the evaluated PFNS and associated covariance matrix for any n+$^{229-238}$U first-chance fission reaction can be computed using Eqs. (3.21) and (3.22). The n(thermal)+^{233}U PFNS and covariance matrix are computed and the results are shown in Figs. 4.4–4.6.

In the most recent release of the ENBF/B-VII.1 data library [1], the evaluated PFNS of the n(thermal)+^{233}U is described as an energy dependent Watt spectrum while the remaining major actinides in the library have been evaluated using the LA model. Using the information from the posterior parameters and covariance matrix, a more consistent evaluation of the PFNS and its uncertainties across this suite of uranium isotopes can be included in future releases of the ENDF/B-VII library.

In Fig. 4.5 the uncertainty of the PFNS for the n(thermal)+^{233}U reaction is shown compared with the JENDL-4.0 [2] evaluation. The "Posterior from KALMAN" re-

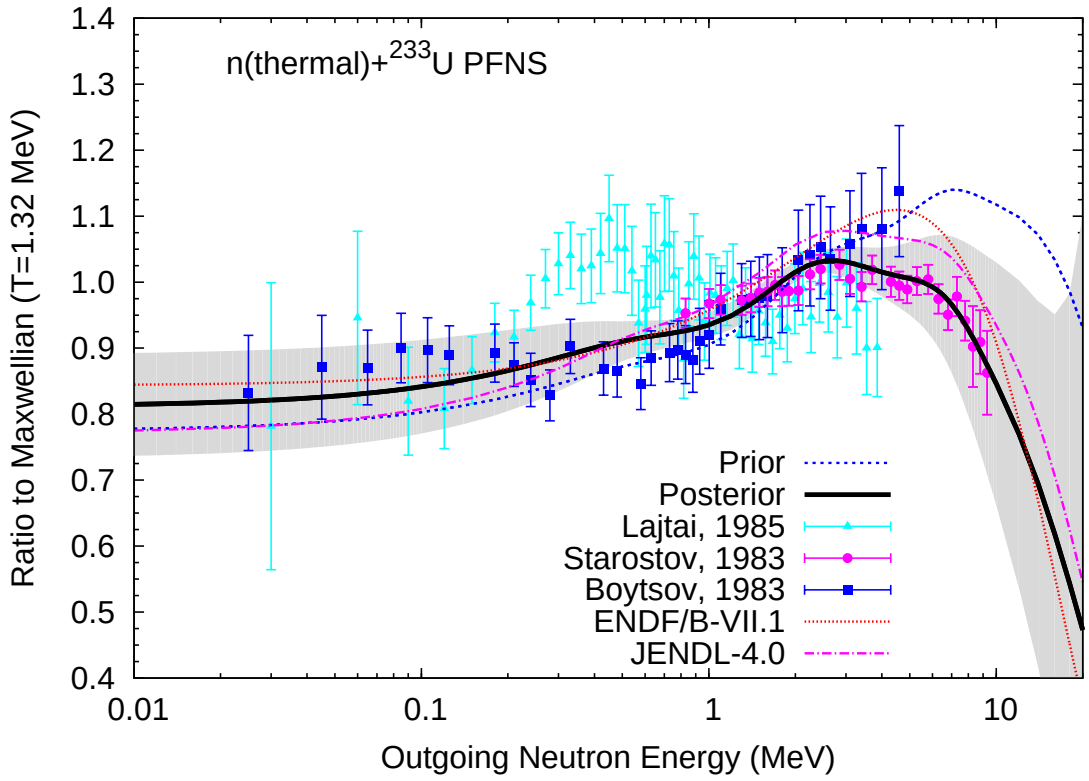

Figure 4.4: The PFNS of the n(thermal)+^{233}U fission reaction is plotted as a ratio to a Maxwellian spectrum at T=1.32 MeV with experimental data and the current ENDF/B-VII.1 and JENDL-4.0 evaluations. The experimental data are normalized to the posterior PFNS in the thick black line.

sults show extremely low uncertainties reported and this can be partly attributed to how the experimental correlations are handled. Even though the experimental correlation matrices for each individual experiment used in the present work were evaluated more realistically using the GMA methodology, correlations between separate experimental datasets have not been included in this work. Because all of the datasets are considered uncorrelated, the posterior uncertainties resulting from the Kalman filter are much smaller than reported experimental uncertainties. To remedy this, an *ad hoc* fix is applied by "rescaling" the covariance matrix such that the smallest uncertainty in the PFNS will be rescaled to what is believed to be a more

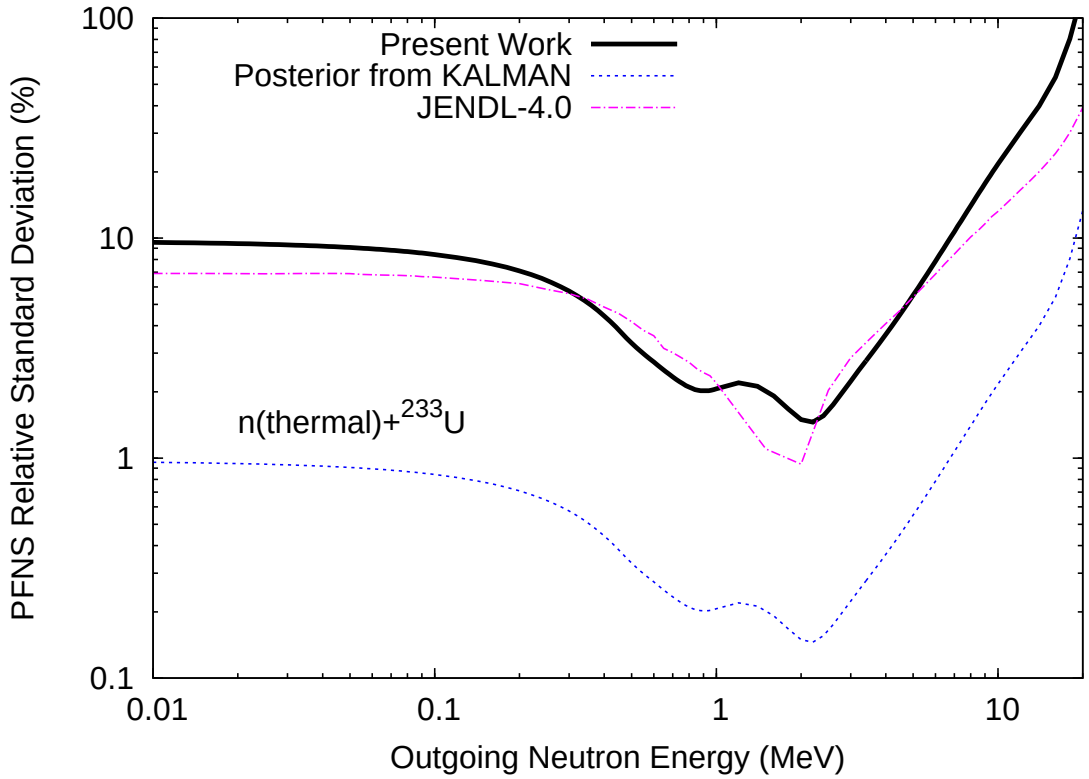

Figure 4.5: The uncertainty of the PFNS for the n(thermal)+^{233}U fission reaction. The lowest evaluated uncertainty lies near the mean outgoing neutron energy ($\sim$ 2 MeV) and located generally where experimentalists report the smallest statistical uncertainties.

realistic uncertainty value in the range of 1-2% near the mean outgoing energy.

Due to the fact that the PFNS is a probability distribution function and its integral must be normalized to unity, the correlation matrix has a unique shape. As can be seen in Fig. 4.6 the correlations are divided into two separate block regions. Starting from the low energy tail of the PFNS, near the mean outgoing energy the correlation goes from being highly correlated to highly anti-correlated. This simply means that the PFNS has a pivoting point near the mean outgoing energy and if one side increases the alternate side must compensate and decrease. Note that

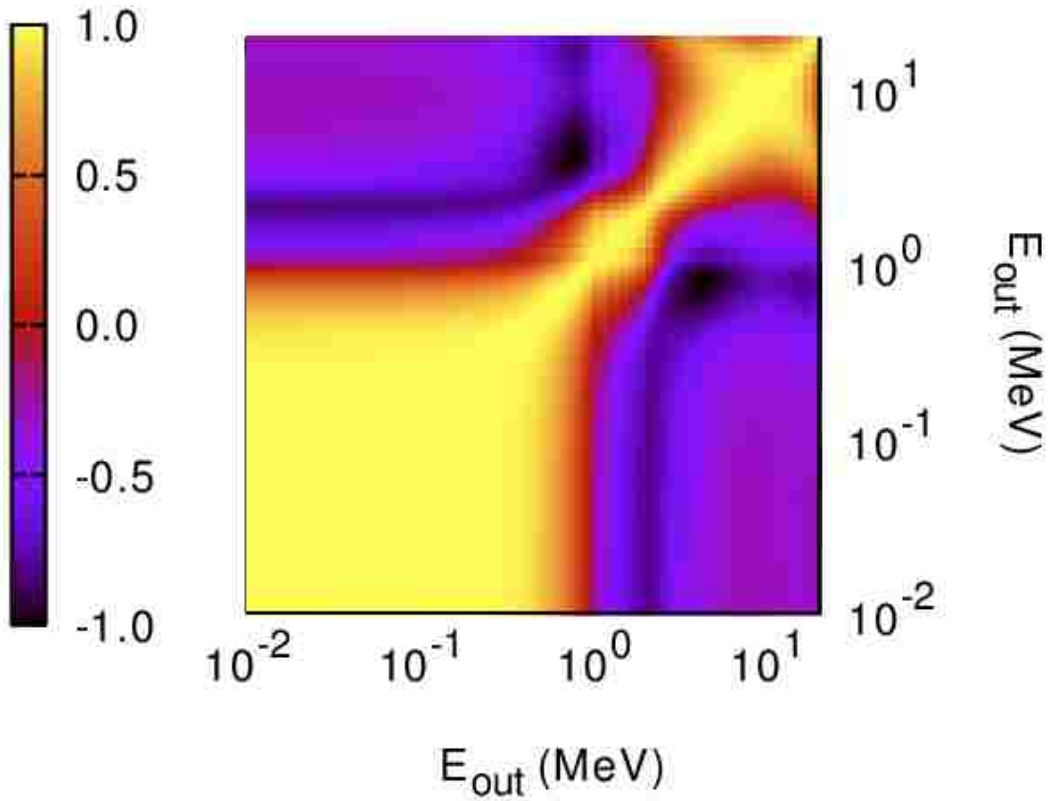

Figure 4.6: The correlation matrix of the PFNS of the n(thermal)+^{233}U fission reaction. As already observed for the ^{238}Pu PFNS in Fig. 4.1, the overall shape of the covariance matrix is dominated by two strongly correlated blocks. The inclusion of experimental data in the analysis leads to finer structures in the matrix.

this feature is very important when sampling from the covariance matrix because it ensures that the sampled PFNS will remain normalized.

The most recent PFNS experimental datasets available for the ^{235}U(n_{th},f) reaction are shown in Fig. 4.7 along with the present work. Both Kornilov [67] and Vorobyev [68] datasets have been normalized to the posterior results shown as the solid line. Over the entire energy range of the Kornilov dataset, excluding the last few data points above 10 MeV, the agreement with the present work is extremely good. In general, this present work agrees to within the quoted experimental uncertainties

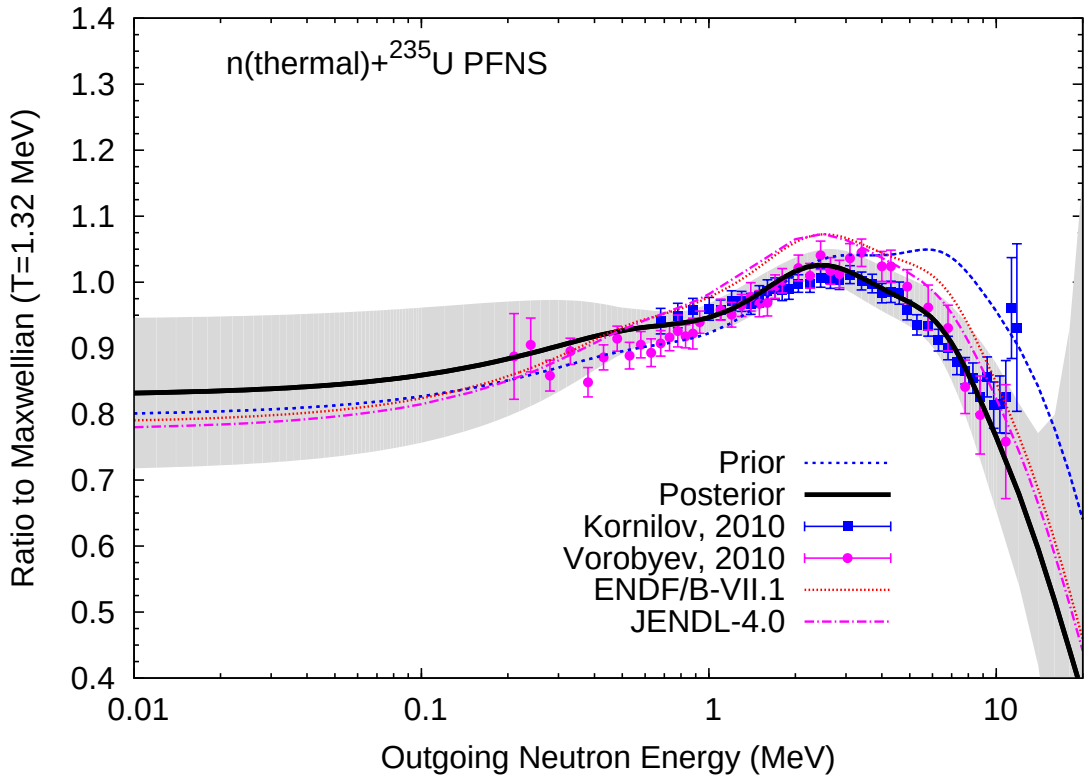

Figure 4.7: The PFNS of the ^{235}U(n$_{th}$,f) reaction plotted in ratio to a Maxwellian spectrum at T= 1.32 MeV with experimental data and the current ENDF/B-VII.1 and JENDL-4.0 evaluations.

excluding a couple of data points in each of the high and low energy tails.

The n(thermal)+^{235}U fission reaction is very important in many applications. For some other applications, the incident energy dependence of the PFNS is of importance as well. The previous evaluation of the PFNS for the n(0.5 MeV)+^{235}U fission reaction used mostly the Johansson [76] dataset to constrain LA model parameters. Figure 4.8 shows the present work along with the Johansson dataset normalized to the posterior PFNS. It can be seen that the present work is within the quoted uncertainties and the shape of the spectrum over the experimental data energy range is generally in very good agreement.

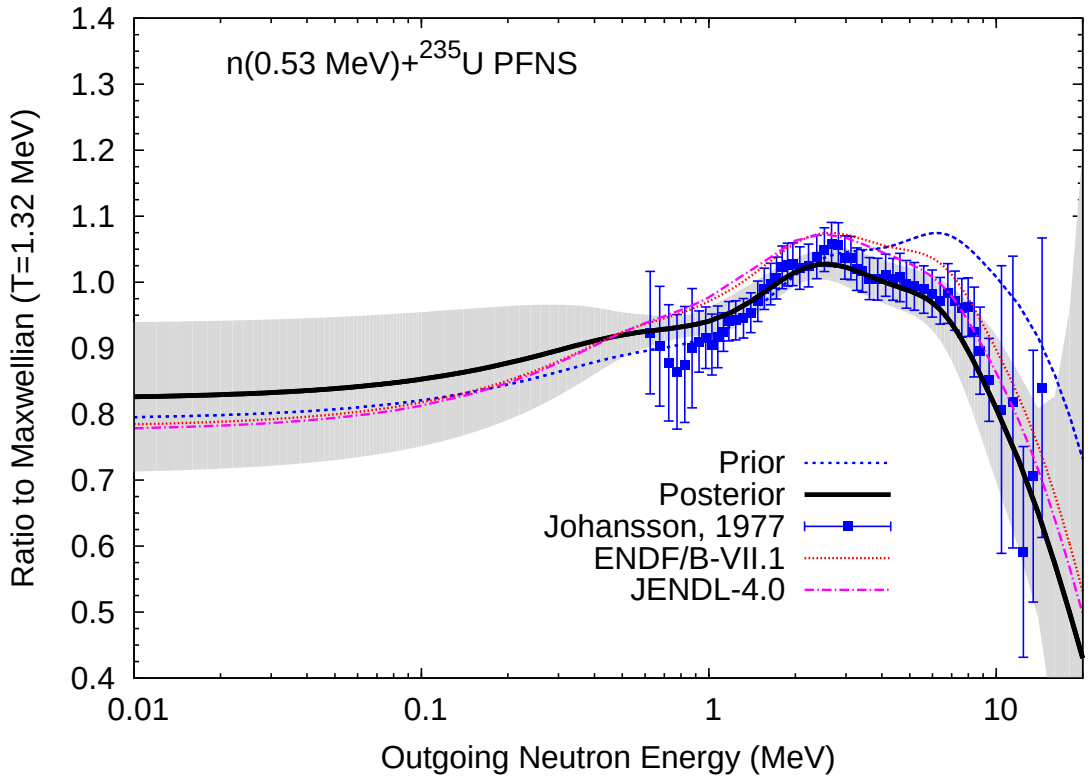

Figure 4.8: The PFNS of the n(0.53 MeV)+^{235}U fission reaction plotted as a ratio to a Maxwellian spectrum at T=1.32 MeV with experimental data and the current ENDF/B-VII.1 and JENDL-4.0 evaluations.

In both Figs. 4.7 and 4.8 the most recent ENDF/B-VII.1 evaluation is plotted along with the present work. The only difference between the two versions of the LA model used is the inclusion of the anisotropy parameter (see Eqs. (2.31) and (2.32)). The effect that this parameter has on the PFNS is in the low energy tail between 400 keV and 1 MeV and can be seen in the difference between the shapes of the ENDF/B-VII.1 PFNS and the present work. By including this new parameter, the low energy part of the spectrum changes shape and increases while leaving the shape of the peak and the high energy tail almost unchanged.

In this work, the experimental measurements done by Boikov [74] for both n(2.9

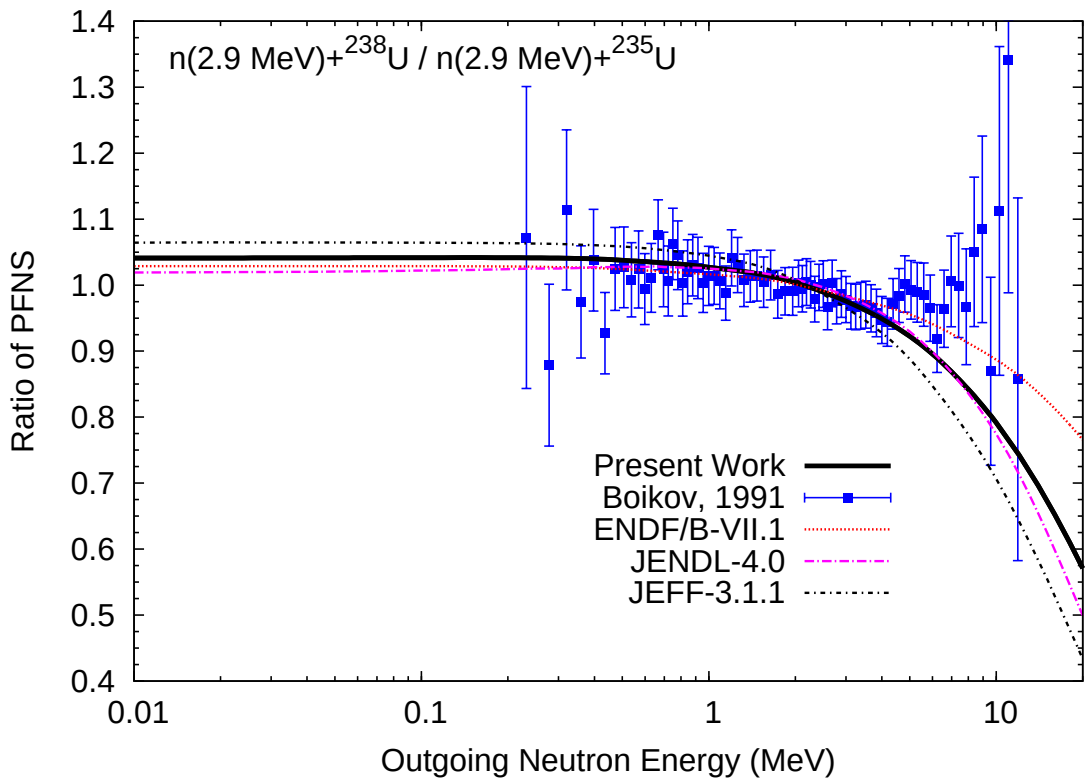

Figure 4.9: The ratio of the PFNS for the n(2.9 MeV)+^{238}U fission reaction to the PFNS for the n(2.9 MeV)+^{235}U fission reaction is plotted with the present work, experimental data by Boikov [74] and the current ENDF/B-VII.1, JENDL-4.0, and JEFF-3.1.1 evaluations.

MeV)+^{235}U and n(2.9 MeV)+^{238}U reactions have been included in the evaluation procedure. These datasets have been the main culprit in terms of large discrepancies in the high energy tail between the experimental data and the posterior results. The n(2.9 MeV)+^{238}U evaluated PFNS is in good agreement throughout the entire range of the experimental outgoing energy unlike the n(2.9 MeV)+^{235}U evaluated PFNS which has large discrepancies in the high outgoing energy tail of the spectra. In Fig. 4.9 a ratio of the two measurements has been plotted as well as the same ratio of the present work and several evaluated data libraries. The present work and the evaluated data libraries show the same downward trend at higher energies

while the ratio of the experimental measurements is almost constant above 5-MeV outgoing neutron energy. The simplified treatment of the level density used in this work (Eq. (2.36)) leads naturally to a harder spectrum for ^{235}U than for ^{238}U. Boikov data do not show this trend however. The best agreement is obtained for ENDF/B-VII.1, whose parameter values have been tuned around this incident neutron energy to better agree with Boikov's data.

4.1.2 Plutonium 235-242

The plutonium suite of isotopes has several PFNS experimental measurements in the EXFOR database but only for ^{239}Pu. In the cases where the experimental data are cited by the work done at the IAEA [32], the data reported by the IAEA is the differential data used in this work which may differ slightly from the original published data. The use of the LA model and Kalman filter for evaluating the PFNS uncertainties of the n(0.5 MeV)+^{239}Pu reaction was done recently [66]. The present work follows the same methodology applied to the entire suite of plutonium isotopes below the threshold for second-chance fission.

Mass # (A)	First Author	Date	E_{inc} (MeV)	E_{out} (MeV)	EXFOR Entry	Ref.
239	Staples	1995	0.5-3.5	0.596-15.952	13982-003	[73]
239	Lajtai	1985	thermal	0.03-3.855	30704-004	[70, 32]
239	Starostov	1985	thermal	3.007-11.2	40930-008	[71, 32]
239	Boytsov	1983	thermal	0.021-4.5	40873-006	[72, 32]
239	Knitter	1972	0.215	0.28-13.87	20576-003	[81]

Table 4.4: Experimental measurements of the n+$^{235-242}$Pu PFNS used in the present work including entries from both the EXFOR database [31] and modified data from the IAEA PFNS experimental data [32].

Figure 4.10 shows the prior parameter values and posterior parameter values across the entire suite of plutonium isotopes for the difference between the average

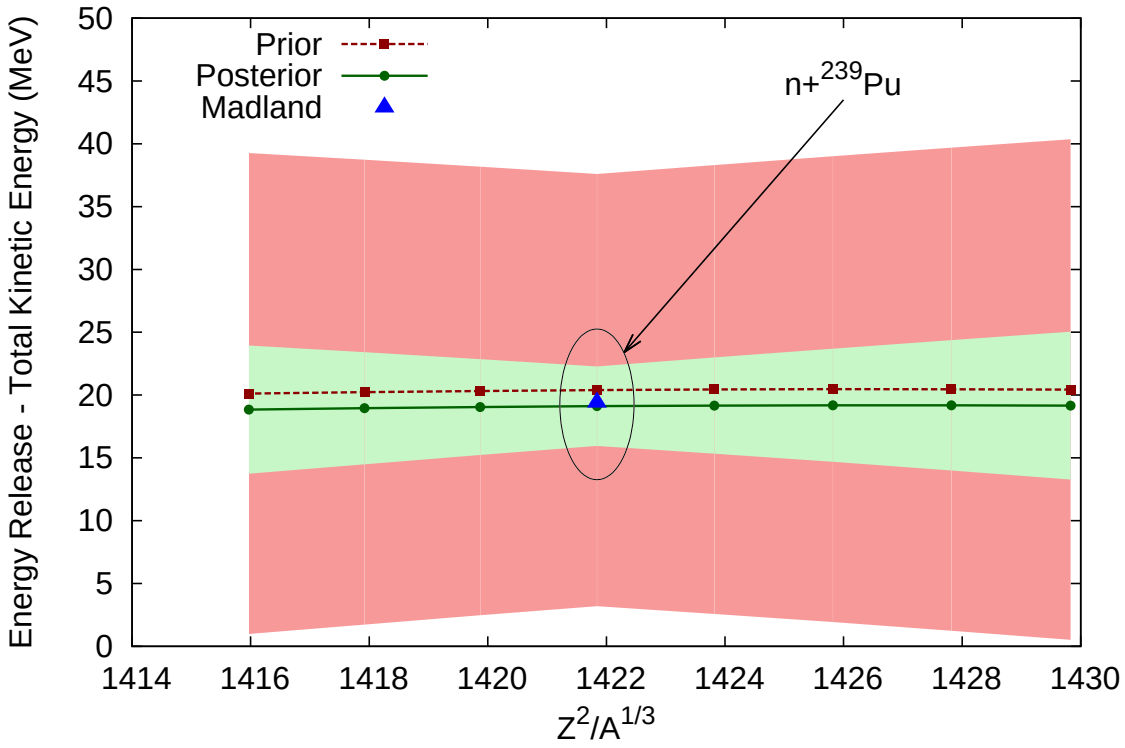

Figure 4.10: The difference between the average energy release and the total kinetic energy of the n+$^{235-242}$Pu PFNS plotted with calculations done by Madland [80].

energy release, $\langle E_r \rangle$, and the average total kinetic energy, $\langle \mathrm{TKE} \rangle$. Because Fig. 4.10 is the difference between two uncertain parameters the prior uncertainty band shaded in light red and the posterior uncertainty band shaded in light blue are large. This allows the model parameters to explore a very large and in some cases unphysical parameter space, but the experimental data constrains the parameters in a very reasonable way.

The prior values taken from Tudora [41] and posterior parameters from the present work along with all of the uncertainties are given in Table 4.5. Because the prior systematics were altered from the original values given by simply shifting the origin of the parameters to be located at the n+^{239}Pu reaction, the prior and

posterior values for α_2, α_4, and α_5 remain the same. If other experimental data in the plutonium suite existed outside of ^{239}Pu, then the prior and posterior values for α_2, α_4, and α_5 would differ and the plutonium suite would have results similar to the uranium suite discussed earlier.

Parameter		Prior Value	Prior Uncertainty (%)	Posterior Value	Posterior Uncertainty (%)
$\langle$TKE$\rangle$	α_1	177.56	2.0	178.34	1.14
—	α_2	-0.231	100.0	-0.231	100.0
$\langle E_r \rangle$	α_3	197.96	6.0	195.43	0.91
—	α_4	-354.69	50.0	-354.69	50.0
—	α_5	-5140.7	25.0	-5140.7	25.0
C	α_6	11.000	4.0	11.042	3.82
b	α_7	0.100	50.0	0.127	20.91

Table 4.5: Parameters of the LA model evaluation of the n+$^{235-242}$Pu PFNS, where $\alpha_1 - \alpha_6$ are in MeV and α_7 is dimensionless.

The prior correlations between the parameters are chosen to be null and the posterior parameter correlations resulting from applying the Kalman filter (Eq. (3.22) are given in Table 4.6. Once again, because of the shifting of the systematics and the lack of experimental data outside of ^{239}Pu, the correlations for α_2, α_4, and α_5 remain zero. Again, the correlation between α_1 and α_3 show that the average total kinetic energy and the average energy release across this suite of isotopes are strongly correlated. The level density parameter, α_6, is correlated with the average total kinetic energy, α_1, and is anti-correlated with the average energy release, α_3. The anisotropy parameter, α_7, is correlated with both α_1 and α_3. Basically, the same trends exist in the correlations between the parameters as was seen in the evaluation of the suite of uranium isotopes.

Although there is a lack of experimental PFNS data for other plutonium isotopes, from the posterior parameters listed in Table 4.5 and the posterior parameter correlation matrix in Table 4.6, the evaluated PFNS and associated covariance matrix

Parameter	α_1	α_2	α_3	α_4	α_5	α_6	α_7
α_1	100						
α_2	0	100					
α_3	81	0	100				
α_4	0	0	0	100			
α_5	0	0	0	0	100		
α_6	25	0	-34	0	0	100	
α_7	35	0	29	0	0	3	100

Table 4.6: Posterior parameters correlations of the LA model evaluation of the n+$^{235-242}$Pu PFNS.

for any n+$^{234-242}$Pu first-chance fission reaction can be computed using Eqs. (3.21) and (3.22) and the LA model. Note that if constraints are placed on even just one isotope, a reasonable set of model parameters are available as a result and can be used to calculate any of the PFNS in the suite of isotopes.

Figure 4.11 shows the prior and posterior spectra as well as the thermal experimental data used to constrain the parameters and the current ENDF/B-VII.1 and JENDL-4.0 evaluations. The experimental data below about 500 keV show very large discrepancies, but the present work is in reasonable agreement with the experimental data from Starostov [71] and Boytsov [72]. Both the ENDF/B-VII.1 and JENDL-4.0 evaluations are very similar to each other and the main difference between the present evaluation and previous evaluations is the inclusion of the anisotropy parameter in the LA model that increases the PFNS below 500-keV outgoing energies, thus lowering the peak of the spectrum to maintain normalization of the distribution. Compared with the shape of the ENDF/B-VII.1 and JENDL-4.0 PFNS, the present work has a lower peak in the 1–3-MeV range and the low energy tail from 0.5–1 MeV is higher.

Although the uncertainties for the neutron-induced prompt fission neutron spectrum for low incident energies was done recently [66, 57] using much of the same

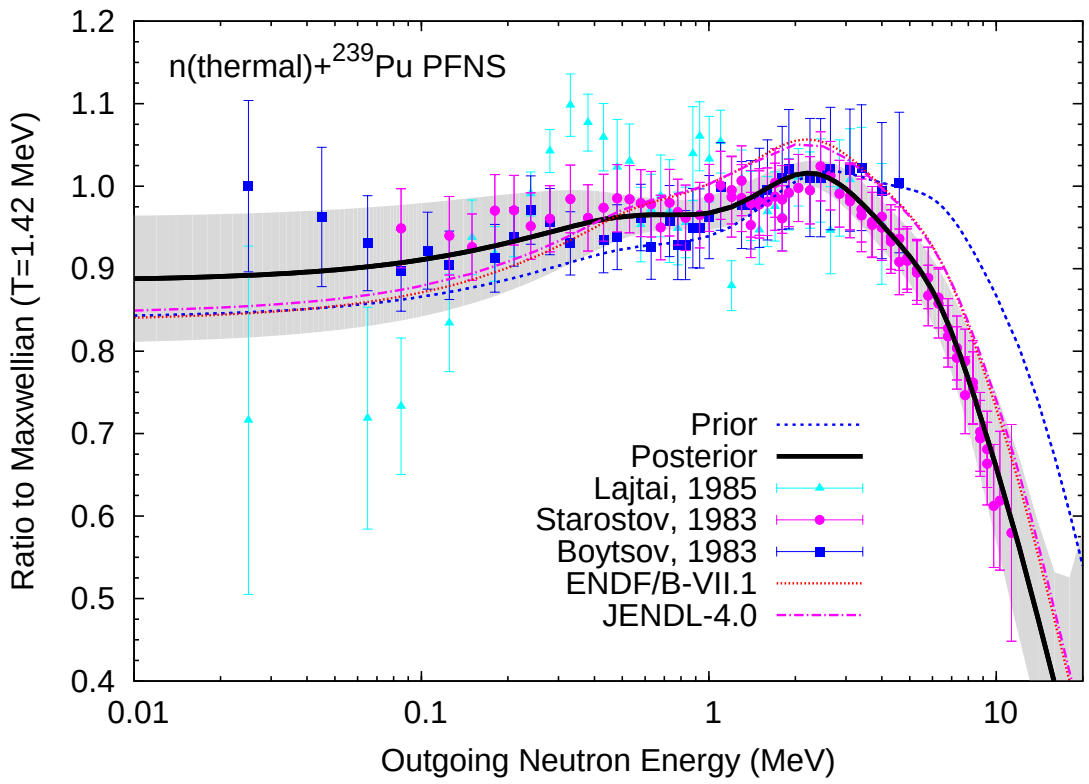

Figure 4.11: The PFNS of the n(thermal)+^{239}Pu fission reaction plotted with experimental data and the current ENDF/B-VII.1 evaluation. The posterior parameters in Table 4.5 were used in Eq. (3.21) to compute this present evaluation.

experimental data, this evaluation has been carried out in order to compare the new evaluated spectrum with the addition of the anisotropy parameter against the ENDF/B-VII.1 evaluation as well as evaluate the spectra and uncertainties across the entire suite of plutonium actinides in a consistent manner. In general, the uncertainties shown in Fig. 4.12 are in agreement with both the ENDF/B-VII.1 and JENDL-4.0 evaluations in both shape and magnitude. Once again, it can be seen that the evaluated uncertainties resulting from the Kalman filter are unreasonably low, therefore the same *ad hoc* fix mentioned previously has been applied by scaling the entire covariance matrix by a constant allowing the correlations to remain invariant to the scaling.

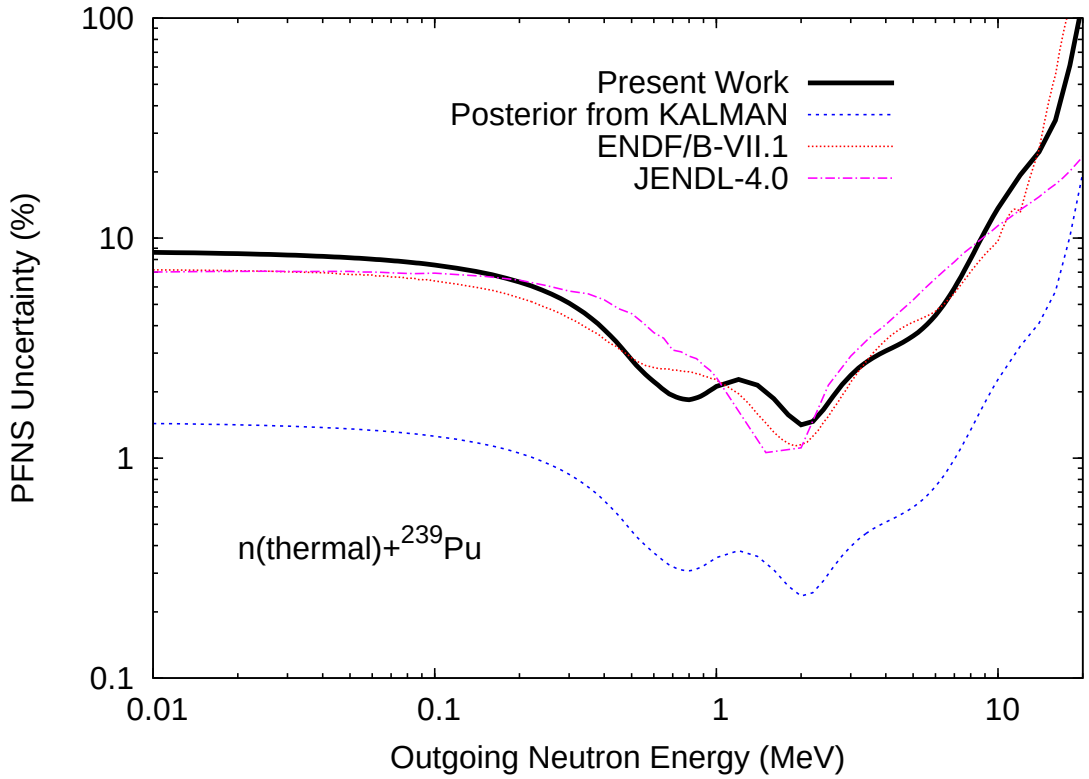

Figure 4.12: The uncertainty in the PFNS of the n(thermal)+^{239}Pu fission reaction. The lowest evaluated uncertainty is near the mean outgoing neutron energy and located generally where experimentalists report the smallest statistical uncertainties.

By applying the covariance matrix of the posterior parameters, built from the uncertainties and correlation matrix in Tables 4.5 and 4.6, respectively, to Eq. (3.22) where the sensitivity coefficients of the PFNS for the n(0.5 MeV)+^{238}Pu fission reaction are known, the associated covariance matrix can be computed. The correlation matrix computed from the resulting covariance matrix can be seen in Fig. 4.13. Comparing the n(0.5 MeV)+^{238}Pu PFNS correlation matrix from the ENDF/B-VII.1 data library in Fig. 4.1 with the correlation matrix in Fig. 4.13 of the same reaction, significant differences can be seen because of the indirect inclusion of the n+^{239}Pu PFNS experimental data in Table 4.4.

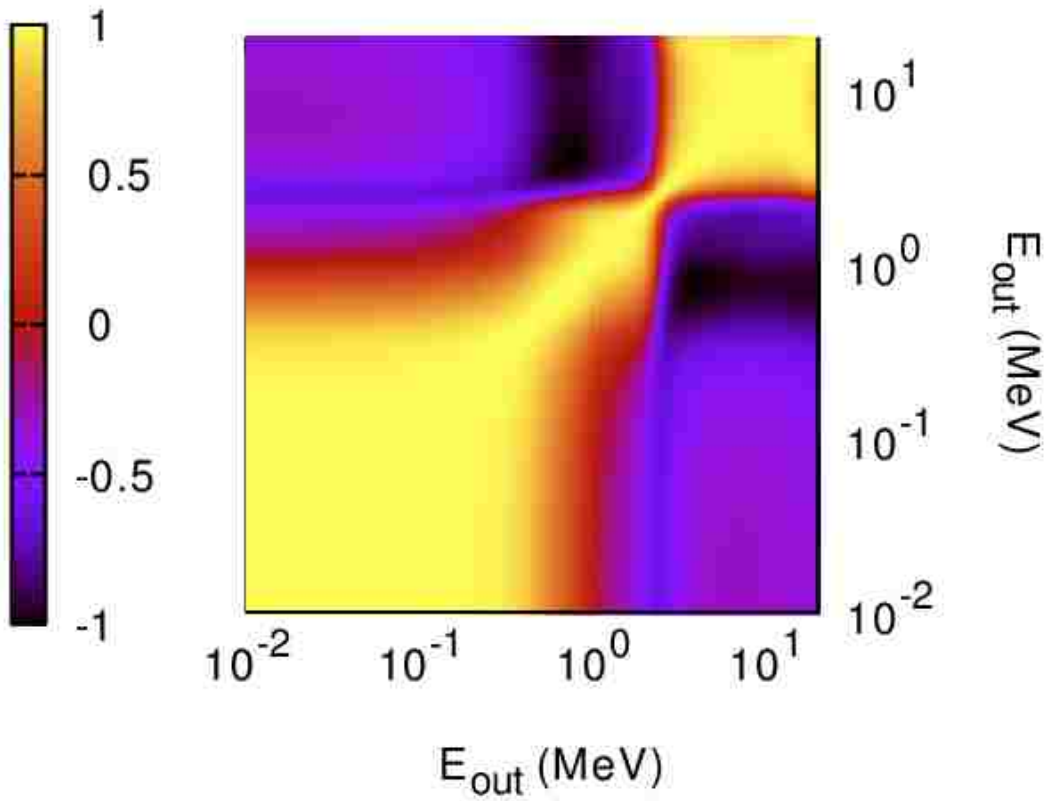

Figure 4.13: The correlation matrix of the PFNS for the n(0.5 MeV)+^{238}Pu fission reaction resulting from the present work. With respect to the evaluation of the same reaction in ENDF/B-VII.1 seen in Fig. 4.1 the structural differences of the correlation matrix are due to the inclusion of experimental data in Table 4.4 for the PFNS of the n+^{239}Pu fission reaction.

The result of this work is that any of the PFNS of the $^{229-238}$U or $^{235-242}$Pu fission reactions mean values and covariance matrices below the second-chance fission threshold can be computed in a consistent way. Results of this work have been saved in ENDF-formatted files and delivered to the National Nuclear Data Center at BNL for inclusion in a future release of the ENDF/B library.

4.1.3 Summary

We have evaluated the PFNS and the associated uncertainties of both a suite of uranium isotopes and a suite of plutonium isotopes below the threshold for second-chance fission in a consistent manner. The entire evaluation process was explained with much detail. In the present calculations, a modified LA model was used by introducing an anisotropy parameter. The uncertainties of the parameters were discussed as well as the systematics obtained to help describe the behavior of the parameters across a suite of isotopes. Experimental data were obtained from the EXFOR database and the uncertainties were estimated using the same methodology that was used for the evaluation of the standard cross sections [23]. A Bayesian approach, a first order, linear Kalman filter, was used to combine the experimental data and uncertainties with the LA model calculations to obtain a reasonable evaluation of the parameters and covariance matrix.

The evaluation of the parameters and covariance matrix provides a consistent way to compute the evaluated PFNS and covariance matrix across isotopes. In the ENDF/B-VII.1 nuclear data library, many of the minor actinides have missing or inconsistent evaluated PFNS and covariance matrices. The results presented in this work will be proposed to fill those gaps, even for actinides where there is no experimental data. This work can be further extended to include other actinides, e.g., thorium, neptunium, americium, protactinium, and higher incident neutron energies, above the threshold for second-chance fission.

Future work will focus on studying other evaluation approaches, e.g., Unified Monte Carlo [10] discussed in the following section, expanding the experimental data used to constrain the model parameters, e.g., average outgoing energy of the PFNS and average multiplicity, and further understanding the sources of uncertainty for the experimental datasets. The only way to truly understand the impact that the

PFNS uncertainties have on applications is to propagate the uncertainties through well known problems seen in Ch. 6.

4.2 Unified Monte Carlo Implementation

In recent years, there has been research devoted to stochastic methodologies for use in the nuclear data evaluation process. Some of this work has led to interesting results, by avoiding some of the disadvantages of the deterministic methods, namely the Kalman filter method, but some of the methods have introduced their own disadvantages. One method that seems to have almost all of the advantages of the deterministic and stochastic methods with very little of the disadvantages is the Unified Monte Carlo (UMC) approach [10]. So far, the UMC approach has been investigated for a small toy problem only and has yet to be widely implemented in realistic nuclear data evaluations. The background and mathematical theory of the UMC approach have been discussed in Ch. 3.2.

Before moving to the UMC evaluation results, the implementation of the UMC algorithm is verified by simplifying the evaluation to allow comparison directly to the Kalman filter. Because both methods are derived from the same mathematical principles, the UMC method can be "dumbed" down by making the same assumptions that were necessary to derive the Kalman filter. The first UMC results will be obtained by assuming that the LA model calculation is linear with respect to the model parameters. When experimental data is not available to the evaluator or only direct experimental data (no ratio data, integral data, etc.) are used in the evaluation, the UMC results should converge to the Kalman results, given enough Monte Carlo histories are performed and the parameter phase space has been sufficiently sampled. In the original implementation of the UMC method [10], the model parameters were sampled from a uniform distribution with a spread of one standard

deviation to each side of the model parameters, seen mathematically as,

$$\vec{\mathbf{x}}_k = \vec{\mathbf{x}}_0 + \vec{\sigma}_{\vec{\mathbf{x}}_0} \left(2\vec{\xi}_k - 1 \right) , \tag{4.3}$$

where k is the realization index, $\vec{\sigma}_{\vec{\mathbf{x}}_0}$ is the prior standard deviation of the parameters and $\vec{\xi}$ is a uniformly distributed vector of independent random numbers between 0 and 1. By using this sampling distribution, the entire phase space of the parameters may not be sufficiently sampled. Because the prior PDF of the parameters is a Gaussian distribution, a more rigorous approach to sampling the parameters phase space would be to sample from a Gaussian distribution about the prior model parameters, seen as,

$$\vec{\mathbf{x}}_k = \vec{\mathbf{x}}_0 + \vec{\sigma}_{\vec{\mathbf{x}}_0} \left(\vec{\mathcal{N}}_k(0,1) \right) , \tag{4.4}$$

where $\vec{\mathcal{N}}(0,1)$ denotes a zero mean, unit variance vector of independent normally distributed random numbers. Both of these sampling methods as well as the validity of the linear model response assumption are studied in the context of the UMC evaluation methodology applied first to the evaluation of the PFNS for the n(0.5 MeV)+^{239}Pu fission reaction uncertainties previously studied by Talou *et al.* [66] with the addition of the anisotropy parameter fixed at a value of 0.1.

4.2.1 Test Problem: n(0.5 MeV)+^{239}Pu PFNS Evaluation

The data sets used in the evaluation are shown in Table 4.7, similar to the data sets used in the actinide suite evaluation seen in Table 4.4. The uncertainties in the experimental data sets are taken from the EXFOR database [31] and the correlations within each data set are approximated to be 50% in each of the off-diagonal correlation matrix elements. Note that each data set is again considered to be uncorrelated to each of the other data sets. In this work as in the previous evaluation work, the

experimental data sets are all considered at the same incident energy of 0.5 MeV because the model parameters are assumed to be energy-independent. This allows the evaluation of the PFNS uncertainties to be valid over a range of incident energies utilizing multiple experimental datasets while saving on storage space that would be needed to retain many of the large tabulated covariance matrices.

First Author	Date	E_{inc} (MeV)	E_{out} (MeV)	EXFOR Entry	Ref.
Staples	1995	0.5	0.596-15.952	13982-003	[73]
Lajtai	1985	thermal	0.03-3.855	30704-004	[70]
Boytsov	1983	thermal	0.021-4.5	40873-006	[72]
Knitter	1972	0.215	0.28-13.87	20576-003	[81]

Table 4.7: Experimental measurements of the n+^{239}Pu PFNS used in [66] and in the present study of the UMC implementation.

In the evaluation of the uncertainties for the PFNS of the n(0.5 MeV)+^{239}Pu fission reaction, the average total kinetic energy, $\langle \text{TKE} \rangle$, the average energy release, $\langle E_r \rangle$, the binding energy of neutron inducing fission, B_n, and the level density parameter, C (seen in Eq. (2.36) as α_6), are considered to be uncertain. Table 4.8 displays the prior parameters and uncertainties used in all subsequent evaluation results.

Parameter	Prior Value	Prior Uncertainty
$\langle \text{TKE} \rangle$	177.56	2.00
$\langle E_r \rangle$	197.96	8.00
C	11.00	9.00
B_n	6.5342	9.00

Table 4.8: Prior LA model parameter values and uncertainties of the PFNS for the n(0.5 MeV)+^{239}Pu fission reaction. Note the $\langle \text{TKE} \rangle$, $\langle E_r \rangle$ and B_n parameters all have dimension of (MeV) and the C level density parameter is dimensionless and all uncertainties are given in percent.

UMC Implementation Excluding Experimental Data

The first test of the UMC implementation is to apply the UMC algorithm to the n(0.5 MeV)+^{239}Pu evaluation excluding the experimental data in Table 4.8 and assuming the LA model response is linear with respect to the parameters in Table 4.8. This test is useful to verify that the UMC implementation is working correctly, especially with respect to the sampling method chosen. If the model parameters are not sufficiently sampled from, the UMC method might underestimate the posterior uncertainties in the model parameters and the spectrum. In this particular case, given that the UMC results in Eqs. (3.45) and (3.44) are identical to the Kalman filter equations, the UMC posterior calculations should reflect exactly the prior model parameters and uncertainties in Table 4.8 within the Monte Carlo statistics.

Posterior	Kalman Filter		*UMC Uniform		*UMC Gaussian	
Parameter	Value	Uncertainty	Value	Uncertainty	Value	Uncertainty
$\langle$TKE$\rangle$	177.56	2.00	177.56	1.90	177.56	2.00
$\langle E_r \rangle$	197.96	8.00	197.89	7.62	197.88	8.03
C	11	9.00	10.996	8.55	10.995	9.04
B_n	6.5342	9.00	6.5316	8.57	6.5328	8.99
*10^5 UMC histories performed for reported results.						

Table 4.9: Posterior LA model parameter values and uncertainties of the PFNS for the n(0.5 MeV)+^{239}Pu fission reaction excluding experimental data with the LA model assumed linear for both UMC cases.

The resulting posterior parameter values and uncertainties calculated using the Kalman filter, uniformly sampled UMC approach and the normally sampled UMC approach are displayed in Table 4.9. From all of the approaches, the mean values calculated are in very good agreement. This is expected, given enough sampled histories, because both of the UMC sampling approaches are centered about the prior values. The major discrepancy between all three methods is seen in the calculation of the uncertainty of the parameters. While the UMC Gaussian approach and the

Kalman filter results are in extremely good agreement, the UMC uniform approach has significant differences in the computation of the parameter uncertainties. For all model parameters, the UMC uniform approach underestimates the uncertainties due to the truncation of the distribution of the parameters. By sampling one standard deviation away from the model parameters central value, the uniform sampling method does not capture all of the prior variance in the model parameters, leading to an underestimation of the calculated uncertainties.

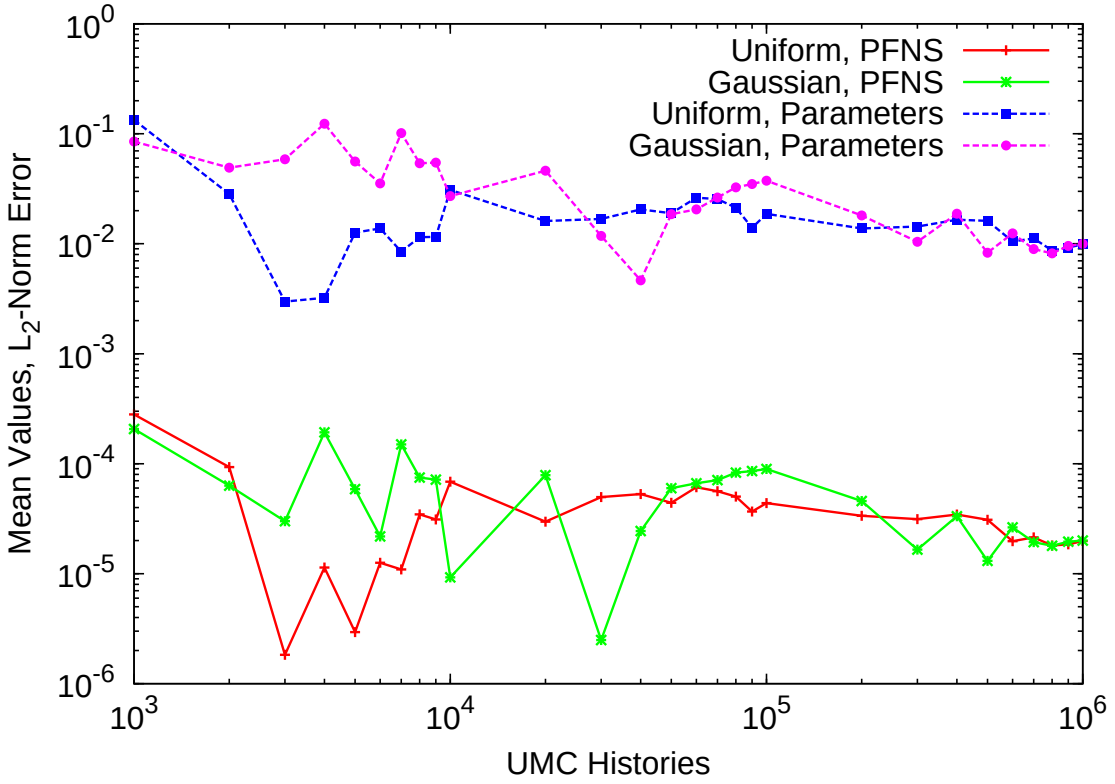

Figure 4.14: The L_2 norm errors of the mean values of the posterior model parameters and PFNS resulting form the UMC approaches compared with the Kalman filter results. Both UMC approaches converge toward the Kalman filter solution at a rate of $\sim 1/\sqrt{N}$.

In Fig. 4.14 the convergence of the posterior central values resulting from the UMC approaches compared to the Kalman filter are displayed. Even with the Monte

Carlo noise, there is a definite trend for all of the central value errors such that we observe roughly $1/\sqrt{N}$ convergence rates where N is the number of UMC histories.

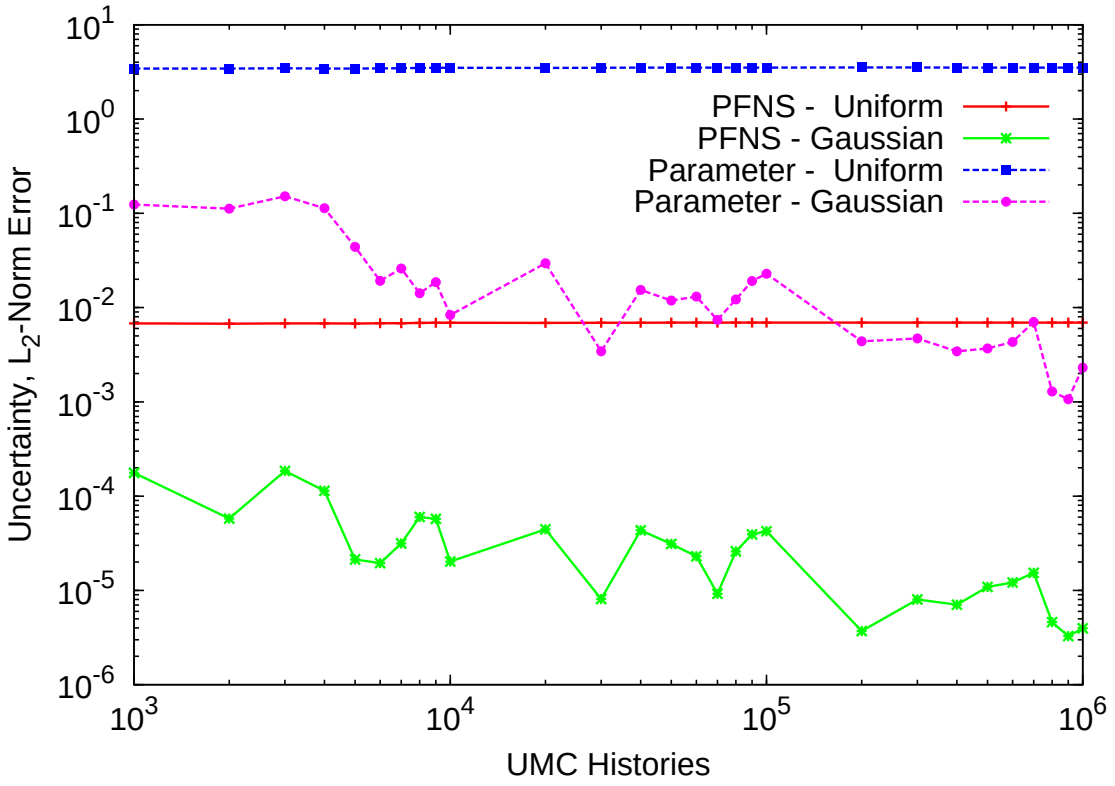

Figure 4.15: The L_2 norm errors of the standard deviations of the posterior model parameters and PFNS resulting form the UMC approaches compared with the Kalman filter results.

In Fig. 4.15 the convergence of the posterior standard deviation resulting from the UMC approaches compared to the Kalman filter are displayed. Much like in Table 4.9 the discrepancies between the UMC approaches show up in the computed uncertainties. The uncertainties computed using the UMC Gaussian approach show approximately the same convergence properties as with the central value convergence plots in Fig. 4.14 such that we once again observe roughly $1/\sqrt{N}$ convergence rates where N is the number of UMC histories. On the other hand, the UMC uniform errors remain nearly constant for increasing number of histories. This result was

expected due to the truncation of the sampled distribution used in the UMC uniform implementation.

The next test of the UMC algorithm is similar to the first test with the experimental data excluded and the linear model response assumption. The difference is that the sampled parameters are biased based on their physical and mathematical meaning in the context of the LA model calculations. When calculating the PFNS from a given set of model parameters using the LA model, the maximum temperature, T_m, in Eqs. (2.26) and (2.32) must remain positive to calculate the PFNS using the LA model. The only cases where the maximum temperature is not positive is when either the average excitation energy, $\langle E^* \rangle = \langle E_r \rangle + E_n + B_n - \langle \text{TKE} \rangle$, or the average level density, $\langle a \rangle = A/C$, are negative (see Eq. (2.30)). When sampling from the model parameters, especially from the Gaussian distribution, there is a nonzero probability that the parameters could be sampled in such a way that the maximum temperature is imaginary. Up until this point, because the LA model is not being directly used due to the linear assumption, all realizations of the model parameters are being utilized. However, because this limitation truly exists for the evaluation of the PFNS using the LA model, the amount of biasing that results from each sampling method is determined.

Posterior	Kalman Filter		*UMC Uniform		*UMC Gaussian	
Parameter	Value	Uncertainty	Value	Uncertainty	Value	Uncertainty
$\langle \text{TKE} \rangle$	177.56	2.00	177.56	1.90	177.49	1.99
$\langle E_r \rangle$	197.96	8.00	197.89	7.62	199.46	7.24
C	11	9.00	10.996	8.55	10.997	9.04
B_n	6.5342	9.00	6.5316	8.57	6.5347	8.99
*10^5 UMC histories performed for reported results.						

Table 4.10: Posterior LA model parameter values and uncertainties for the PFNS of the n(0.5 MeV)+^{239}Pu fission reaction excluding experimental data and the LA model parameters are biased by discarding unphysical samples of the model parameters.

When biasing the sampled parameters, whenever a sampled set of parameters leads to a negative excitation energy, the sample is discarded and a new sample is drawn. While enforcing this biased sampling method, the uniform UMC implementation skipped zero of the total histories because the prior uncertainties are chosen to be small enough such that a negative excitation energy or level density is not possible in the 1-σ range about the prior parameters. The Gaussian UMC implementation skipped $\sim$4.7% of the total histories due to the biasing of the sampled parameters where it is clearly possible to sample in the either of tails of the Gaussian distribution. The percentage of skipped histories is directly related to the prior central values and uncertainties chosen. Table 4.10 shows the posterior central values and uncertainties computed using the Kalman filter and both UMC approaches resulting from biasing the sampled model parameters. The UMC posterior mean values for both the $\langle \text{TKE} \rangle$ and $\langle E_r \rangle$ have some discrepancies from the Kalman filter that can be explained while the remaining parameter central values are computed very accurately. When sampling from the $\langle \text{TKE} \rangle$ and $\langle E_r \rangle$ parameter spaces, the $\langle \text{TKE} \rangle$ distribution will be slightly biased lower and the $\langle E_r \rangle$ will be slightly biased higher to avoid obtaining a negative excitation energy. Another result of biasing the sampled parameters is a small, 3% correlation is introduced between the $\langle \text{TKE} \rangle$ and $\langle E_r \rangle$ model parameters while all of the calculated correlations in the first test were less than 1%.

In Fig. 4.16 some significant differences in the computed posterior PFNS from the various methods are seen. First, the Kalman, linear UMC uniform and linear UMC Gaussian calculated spectra are nearly identical, therefore, only the Kalman filter PFNS is plotted. The biased Gaussian UMC solutions differ slightly from the Kalman filter results due to the increased average excitation energy resulting from the increased average energy release leading to a harder PFNS. The largest discrepancies from the Kalman filter prior PFNS come from the UMC nonlinear posterior PFNS calculations. In the nonlinear calculations, the model parameters are used in the LA

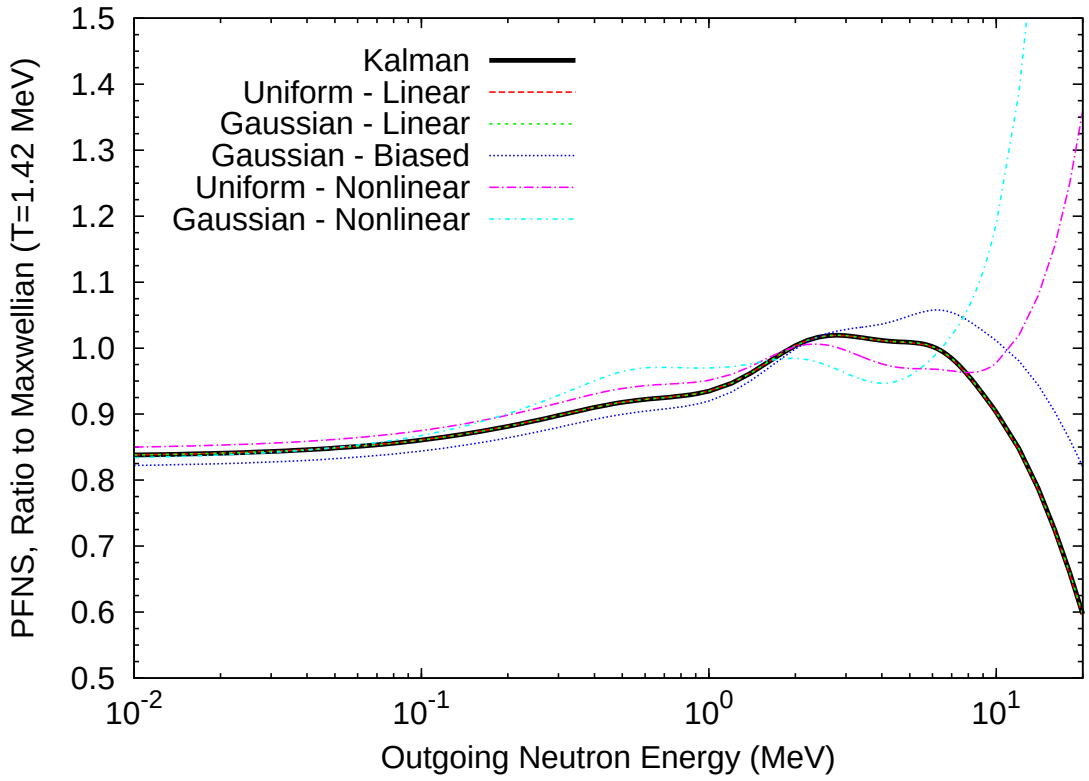

Figure 4.16: The posterior PFNS for the n(0.5 MeV)+^{239}Pu fission reaction while excluding experimental data in the evaluation.

model calculation for each realization unless the sampled parameters are unphysical in the context of the LA model.

The final test performed while excluding experimental data is using the suggested UMC implementation, allowing possible nonlinearities from the model calculations to be present in the evaluation. In this approach the model parameters are still biased, but the LA model is used to calculate response to the sampled model parameters. In Fig. 4.17 there are some differences in the computed PFNS uncertainty most noticeable between the linear and nonlinear methods. The Kalman filter and all of the linear UMC methods calculate nearly the same PFNS uncertainty. The biggest differences exist when the nonlinear UMC methods are implemented where a

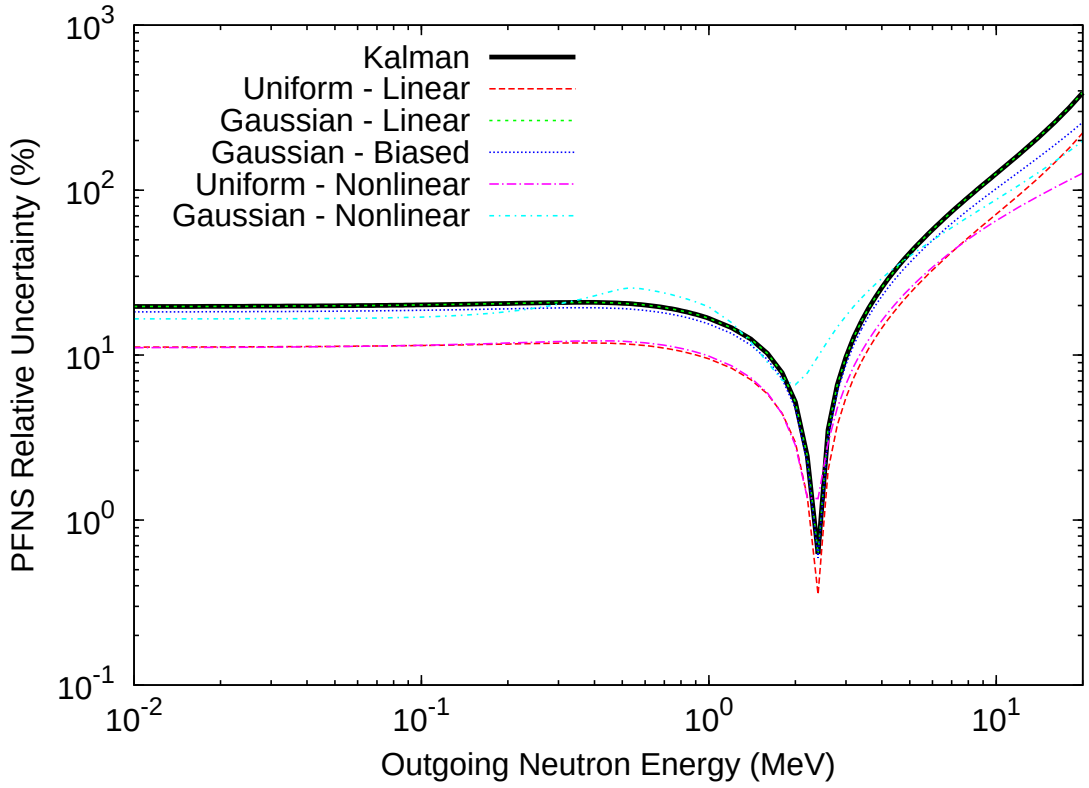

Figure 4.17: The posterior PFNS uncertainties for the n(0.5 MeV)+^{239}Pu fission reaction while excluding experimental data in the evaluation.

slight bump is introduced below about 1 MeV and the valley where the lowest uncertainty exists is shifted slightly lower in outgoing energy and increases by an order of magnitude. When experimental data is unavailable for an evaluation of the PFNS, the UMC method can be seen as an improvement over the Kalman filter because the resulting PFNS central values and uncertainties capture a significant amount of nonlinearity leading to a more appropriate evaluation of the PFNS.

In Fig. 4.18 the PFNS correlation matrices are presented using the Kalman filter and the nonlinear UMC Gaussian implementation. There are significant differences in the correlation matrices throughout the outgoing energy range all due to the nonlinearities present in the LA model. The Kalman filter and the UMC implemen-

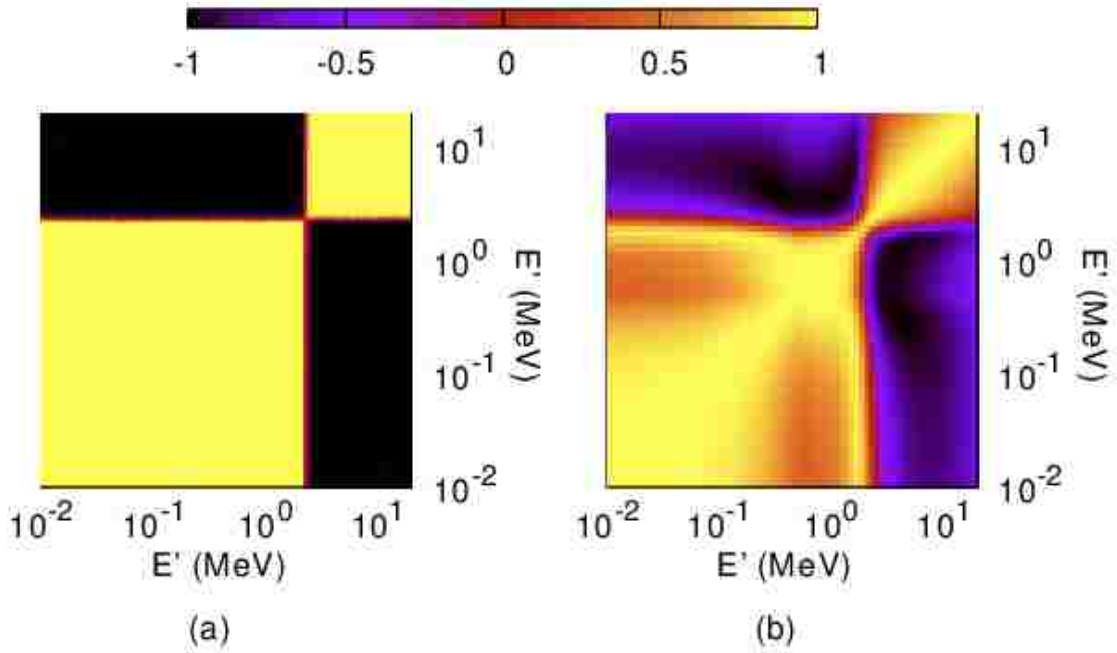

Figure 4.18: The posterior PFNS correlation matrices are calculated excluding the experimental data using the (a) Kalman filter and (b) nonlinear UMC Gaussian implementation.

tation results are inferred from the calculated covariance matrix using Eqs. (3.22) and (3.36), respectively.

So far the results presented on the UMC implementations have been useful to verify that the UMC results, without experimental data, are similar to the Kalman filter results. In cases where the UMC implementation assumes linearity of the LA model and the model parameters are left unbiased, the UMC Gaussian implementation returned exactly the Kalman filter results within the Monte Carlo statistics. When the nonlinear behavior of the LA model is included, the calculation of the prior model parameters and PFNS using the UMC implementations differ significantly from the Kalman filter.

UMC Implementation Including Experimental Data

Now, the experimental data in Table 4.7 is added to the evaluation of the PFNS for the n(0.5 MeV)+^{239}Pu fission reaction. First, because the Kalman filter and UMC implementations are found to agree in Eqs. (3.45) and (3.44) under the model linearity assumption, we keep the linear assumption of the LA model response in the UMC implementation. Once again, the Kalman filter and UMC results using the Gaussian distribution are expected to agree to within the Monte Carlo statistics.

Posterior	Kalman Filter		*UMC Uniform		*UMC Gaussian	
Parameter	Value	Uncertainty	Value	Uncertainty	Value	Uncertainty
$\langle$TKE$\rangle$	176.68	1.66	176.57	1.73	176.65	1.69
$\langle E_r \rangle$	194.33	1.67	194.08	1.69	194.15	1.64
C	10.823	8.84	10.871	8.44	10.877	8.83
B_n	6.5087	9.02	6.5390	8.71	6.5215	9.09
*10^5 UMC histories performed for reported results.						

Table 4.11: Posterior LA model parameter values and uncertainties of the PFNS for the n(0.5 MeV)+^{239}Pu fission reaction including experimental data with the LA model assumed linear for both UMC cases.

The posterior parameters and uncertainties calculated with the Kalman filter and linearized UMC implementations are shown in Table 4.11. For all parameters and uncertainties, the Kalman filter and linearized UMC Gaussian implementation agree extremely well, as is expected from the previous analysis. In the case of the linearized UMC uniform implementation, the agreement is very good as well with some slight underestimations of the uncertainties of both the C and B_n parameter uncertainties most likely due to the truncated sampling distribution.

Next, keeping the linear model assumption while biasing the calculation by discarding model parameter realizations that are outside of the bounds of the LA model does not affect the resulting calculation of the posterior parameters or spectrum. The model parameter realizations that are discarded have a calculated probability very

close to zero based on the likelihood PDF. In this case, the likelihood PDF has effectively discarded the model parameter realization because of disagreement with the experimental data.

Posterior	Kalman Filter		*UMC Uniform		*UMC Gaussian	
Parameter	Value	Uncertainty	Value	Uncertainty	Value	Uncertainty
$\langle \text{TKE} \rangle$	176.68	1.66	176.67	1.75	176.79	1.71
$\langle E_r \rangle$	194.33	1.67	194.18	1.79	194.38	1.71
C	10.823	8.84	10.937	8.53	10.917	8.96
B_n	6.5087	9.02	6.5546	8.64	6.5424	9.03
*10^5 UMC histories performed for reported results.						

Table 4.12: Posterior LA model parameter values and uncertainties of the PFNS for the n(0.5 MeV)+^{239}Pu fission reaction including the experimental data available. The LA model is used to calculate each realization of the model parameters that lead to a positive excitation energy.

The final case that is studied in the present work is the full implementation of the UMC method, including nonlinearities of the model response and utilizing the available experimental data. Table 4.12 shows the posterior parameters and uncertainties of the Kalman filter and both nonlinear UMC implementations, and the differences in all cases are minimal. In the case of the PFNS for the n(0.5 MeV)+^{239}Pu fission reaction, the experimental data are dominant and constrain the model parameters and uncertainties very well, leaving only slight differences in all of the evaluation methods presented.

Figure 4.19 shows the posterior PFNS calculated using the Kalman filter and the linearized, biased and nonlinear UMC implementations. The results for the Kalman filter and all of the linear UMC implementations are nearly identical within the Monte Carlo noise present in the UMC results while the nonlinear UMC implementations very well with each other with a slight difference in the high outgoing energy tail. This means, in the context of a typical evaluation of the PFNS using the LA model when experimental data is available, the posterior central value of the PFNS can

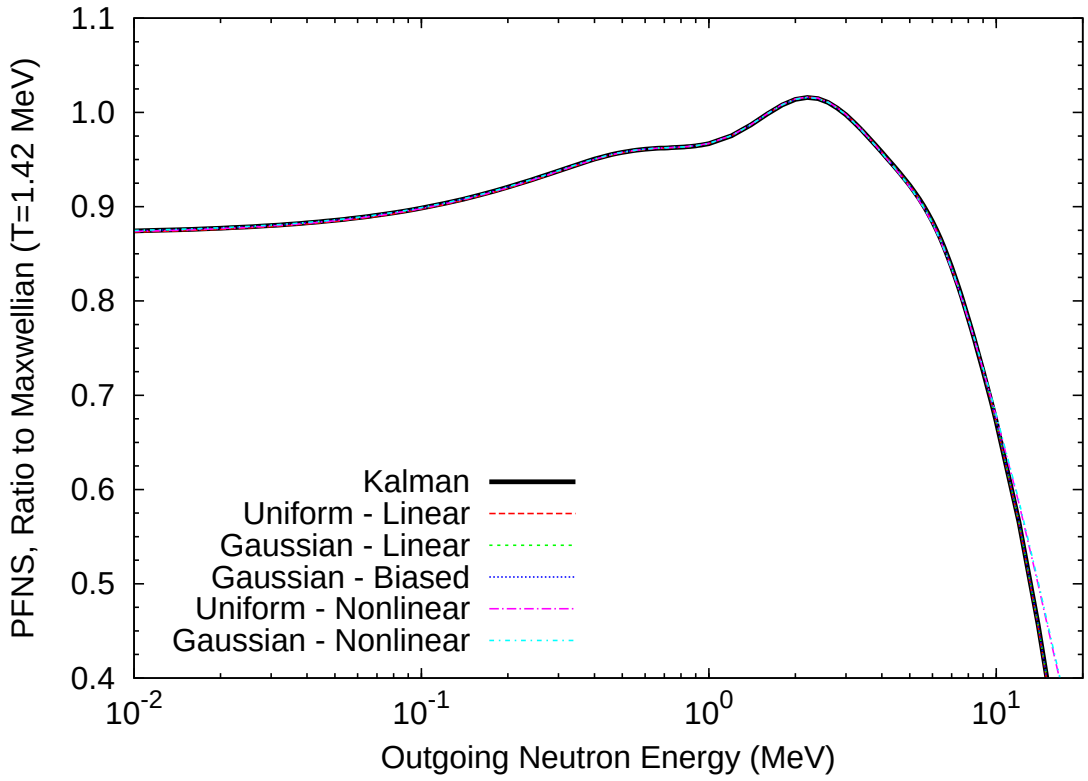

Figure 4.19: Evaluated posterior PFNS calculated utilizing the available experimental differential data. The posterior PFNS for the linear UMC implementations are calculated the same way the Kalman filter posterior PFNS is calculated using Eq. (3.21) while the nonlinear UMC implementations are calculated using Eq. (3.35).

be sufficiently calculated using the Kalman filter because the experimental data constrains the model parameters and PFNS within the linear regime of the LA model and discrepancies only exist in the high outgoing energy tail where the nonlinearities in the model and uncertainty in the spectrum are largest.

The posterior PFNS uncertainties, calculated using Eq. (3.22) for the Kalman filter results and using Eq. (3.36) for the UMC results, are shown in Fig. 4.20. In general the agreement with the Kalman filter is very good throughout the outgoing neutron energy for the Gaussian UMC implementations, except for some minor

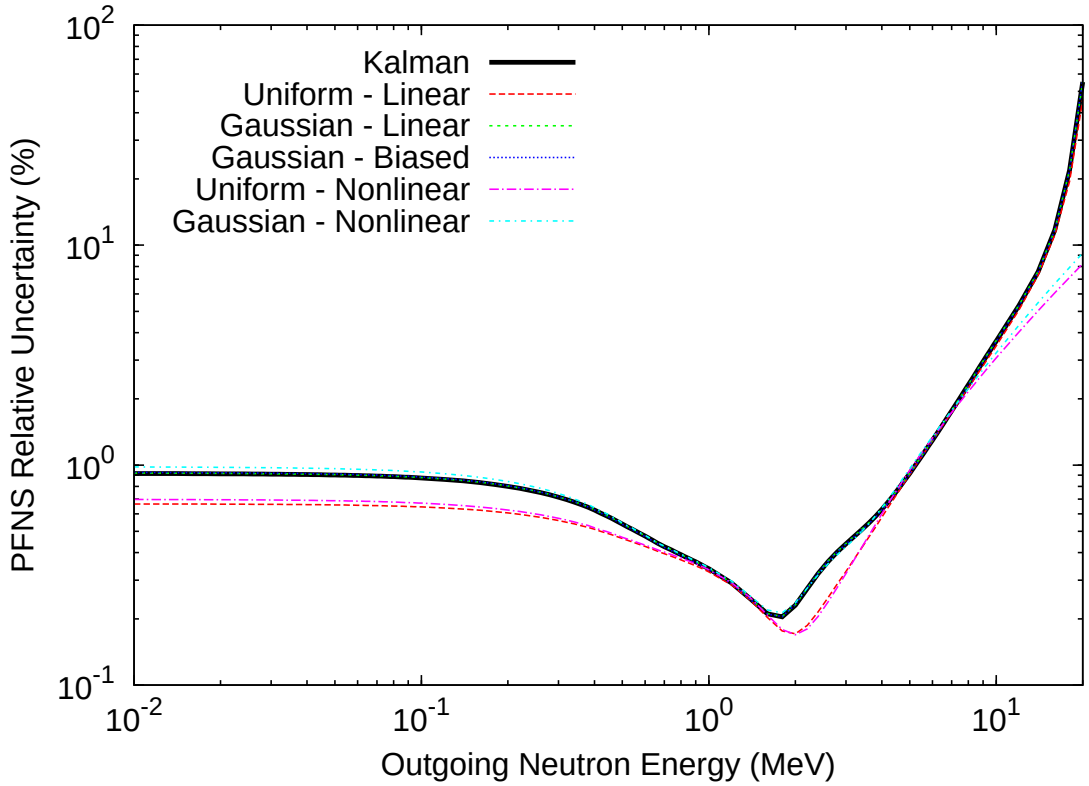

Figure 4.20: The posterior PFNS uncertainties calculated using all of the presented methods including the experimental data. The Kalman filter and the UMC implementation results are inferred from the calculated covariance matrix using Eqs. (3.22) and (3.36), respectively.

discrepancies above about 10 MeV. Like the posterior model parameters calculated using the uniform UMC implementations, the uncertainties in the PFNS are significantly under-predicted due to the inadequate sampling phase-space. While the Kalman filter is capable of capturing some of the nonlinearities in the central values of the PFNS, one advantage the UMC method has is in calculating the PFNS uncertainties in a more exact fashion, capturing nonlinearities in the LA model.

Table 4.13 shows the posterior parameter correlation matrices resulting from the Kalman filter implementation and the nonlinear UMC Gaussian implementation.

Kalman filter					UMC Gaussian				
Parameter	⟨TKE⟩	$\langle E_r \rangle$	C	B_n	Parameter	⟨TKE⟩	$\langle E_r \rangle$	C	B_n
⟨TKE⟩	100				⟨TKE⟩	100			
$\langle E_r \rangle$	66	100			$\langle E_r \rangle$	71	100		
C	14	-61	100		C	8	-59	100	
B_n	3	-14	-1	100	B_n	0	-14	-4	100

Table 4.13: Posterior parameters correlations of the LA model evaluation of the n(0.5 MeV)+^{239}Pu PFNS using the Kalman filter and the nonlinear UMC Gaussian implementation.

The correlations in the parameters are very similar in value with the largest discrepancy being about 6% in the correlation between the ⟨TKE⟩ and C parameters and about a 5% discrepancy in the correlation between ⟨TKE⟩ and $\langle E_r \rangle$.

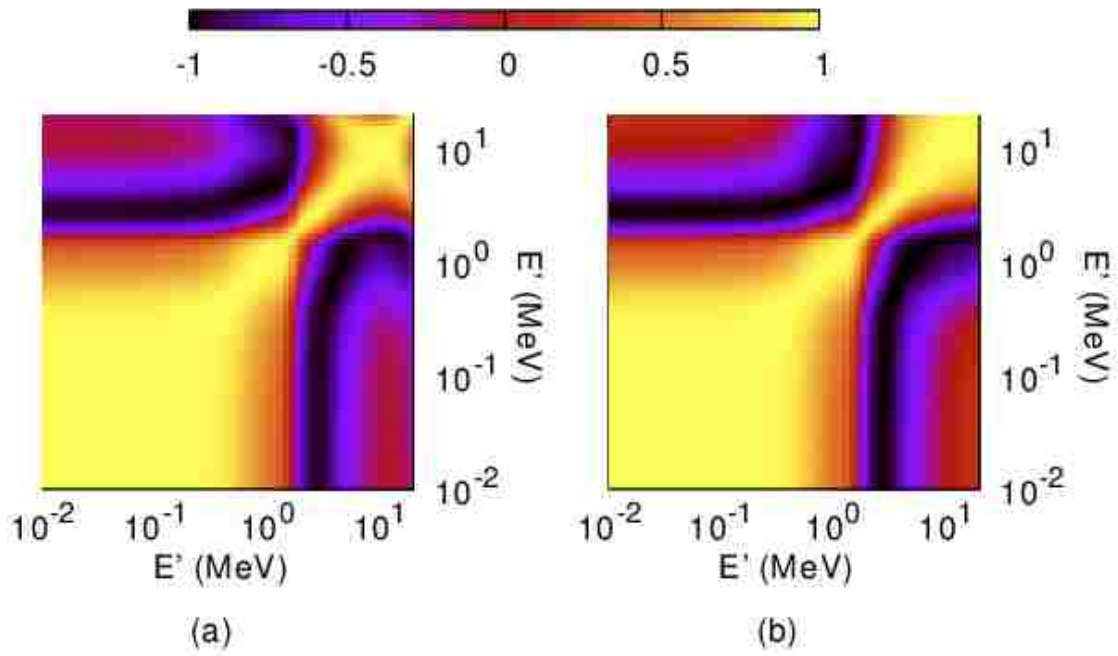

Figure 4.21: The posterior PFNS correlation matrices are calculated using experimental data applied to the (a) Kalman filter and (b) nonlinear UMC Gaussian implementation.

In Fig. 4.21 the PFNS correlation matrices are presented using the Kalman filter and the nonlinear UMC Gaussian implementation. The Kalman filter and the UMC implementation results are inferred from the calculated covariance matrix using Eqs. (3.22) and (3.36), respectively. There are a couple of very slight differences in the correlation matrices, mostly in the higher outgoing energy parts of the correlation matrices where the largest nonlinearities exist in the LA model. Overall, the evaluated PFNS central values, uncertainties and correlations are very similar between the linear Kalman filter and the nonlinear UMC implementations with some small nonlinearities causing some subtle differences in the calculated uncertainties and correlation matrices.

4.2.2 Summary

Various implementations of the UMC method were studied in an effort to compare against the first-order, linear Kalman filter in the evaluation of the PFNS for the n(0.5 MeV)+^{239}Pu fission reaction. First, the UMC methods were implemented while excluding experimental data in the evaluation in an attempt to determine the convergence of the UMC method to the Kalman filter in this simplified case. Many interesting results were found:

- In the original UMC implementation by Capote [10], the prior parameters were sampled from a uniform distribution about their central values leading to an under-prediction of the uncertainties in the prior PFNS with no detectable convergence toward the Kalman filter results.
- A new implementation of the UMC method, sampling from a Gaussian distribution about the parameter central values, was shown to converge to the Kalman filter results when the linear assumption in the LA model was introduced to the UMC method.

- The nonlinearities in the LA model were evident in the calculation of the mean, relative uncertainty and the correlation matrix of the PFNS showing significant differences between the Kalman filter and the nonlinear UMC implementations.

When the experimental data was used in the evaluation of the PFNS there was generally good agreement between the Kalman filter and the UMC uniform and Gaussian implementations with some notable observations made:

- The uniform UMC implementations under-predicted the uncertainties in the PFNS.
- The Gaussian UMC implementation with the LA model forced to be linear performed very well and converged to the Kalman filter results as expected.
- The Gaussian UMC implementation with nonlinearities in the LA model obtained a very similar PFNS central value, uncertainty and correlation matrix to the Kalman filter with some small difference in the high energy tail where the uncertainties are largest and the LA model is most nonlinear.

For the evaluation of the PFNS using the LA model, the Kalman filter is shown to be computationally efficient and accurate enough because the linear assumptions made are very reasonable especially when enough experimental data is used to constrain the model parameters. The Gaussian UMC method agrees very nicely with the Kalman filter results while demonstrating the ability to retain the nonlinearities present in the LA model. To be able to implement the UMC method on a much larger scale to be used for other nuclear data evaluations, the robustness of the implementation needs to be improved, especially to take advantage of the obvious parallel computing capabilities.

Chapter 5

Uncertainty Propagation: Theory

With the availability of massively parallel supercomputing machines, there has been increased attention on both nuclear data uncertainty quantification and propagation through nuclear engineering simulations for many applications including reactor physics, criticality safety, radiation shielding, dosimetry and dose deposition calculations, etc. Chapters 3 and 4 described a few examples of the theory and recent work on uncertainty quantification of nuclear data that is presently underway in the nuclear data community. While this work is important, the uncertainties in nuclear data are not a physical quantity and are meaningless unless they are propagated through nuclear engineering applications shedding light on the impact the uncertainties have on the measurable integral quantities that are of great importance to designing, maintaining and engineering both new and old nuclear facilities.

Generally, when discussing uncertainty quantification in the context of the nuclear applications community, the methods available that have been used include perturbation theory, sensitivity analysis and direct sampling methods. Much like the methods used in solving transport problems and the techniques used to quantify uncertainties in nuclear data, each of the methods available for the uncertainty

propagation and subsequent quantification of the integral quantities of interest have their own advantages and disadvantages. Depending on the application of interest, the method used to quantify uncertainties needs to be chosen with respect to the computational expense, accuracy and the tools already available.

One method that can be used to quantify uncertainties, originally applied in the nuclear application community to the study of pile reactors, is first-order perturbation theory [82]. In this early study of fission chains and nuclear reactors done by Wigner, the basic concepts of perturbation theory were applied to study what impact small changes in the geometry, mass and density of the pile reactor core had on the integral quantities that were measured. The generalized perturbation theory (GPT) and the equivalent generalized perturbation theory (EGPT) developed by Gandini *et al.* [83, 84] has had a major impact on some of the more recent perturbation studies and sensitivity analyses in the field of nuclear engineering. GPT and EGPT each require solving the forward solution and adjoint solution of the transport problem in order to characterize the flux sensitivities with respect to the perturbed input quantities. Most of the original work on solving the adjoint solution of the transport equation used in calculating the sensitivities in the integral quantities was done using deterministic methods and until recently [85, 86, 87], the adjoint solution, specifically related to criticality problems, was difficult to solve using Monte Carlo methods.

Unfortunately, perturbation theory methods for quantifying uncertainties have a couple of downsides. First, they are only valid for small perturbations in the input quantities, where nuclear data uncertainties, in some situations, might be too large to benefit from these powerful methods. And the second is that the perturbation methods are not capable of calculating the higher order moments or probability distributions of the integral quantities of interest. For these reasons, this research focuses on direct sampling-based methods and other forward uncertainty propagation methods where the integral quantity uncertainties can be fully characterized by the

uncertainties present in the nuclear data.

In the present work, the integral quantities that we want to characterize in terms of uncertainty quantification are the solutions to the transport equation introduced in Ch. 2.2, namely the effective multiplication factor, the leakage, and the particular spectral indices described in Eqs. (2.5)–(2.7). The uncertainties present in the PFNS of the fissioning nuclides, in the form of the covariance matrix, will be used to define the random space of the input quantities. In the following section, the methods available to manipulate the covariance matrix and in general, a covariance function, will be discussed in the context of preparing the uncertain input data for use in the uncertainty propagation methods. Next, the sampling-based methods will be introduced, with concentration on the methods that are used in the present work. Finally, the application of the polynomial chaos expansion method is discussed along with the quadrature-based "sampling" method, the stochastic collocation method.

5.1 Covariance Manipulation

Previous work concentrated on the use of the Karhunen-Loéve (KL) transform or expansion [88, 89], representing a second-order random process in a generalized Fourier series in terms of eigenfunctions of its covariance function. In this context, the covariance function is known and continuous where the moments of the random variable or process, y, can be defined. Recall that the moments are,

$$E[y^m] = \int_Y y^m P(y) dy \,, \tag{5.1}$$

over the domain Y given the probability density $P(y)$. If the randomness exists continuously in a dimension x, y is considered a random process where the mean and

covariance are defined as,

$$\langle y(x) \rangle = E[y(x)]\,, \tag{5.2}$$

and

$$C_y(x_1, x_2) = E\Big[\Big(y(x_1) - E\left[y(x_1)\right]\Big)\Big(y(x_2) - E\left[y(x_2)\right]\Big)\Big]\,, \quad x_1, x_2 \in X\,, \tag{5.3}$$

respectively, continuous throughout the domain X. In this notation, we define the expected covariance to be shifted about the expected mean values. The KL expansion relies on the fact that the covariance function, by definition, is bounded, symmetric and positive definite and due to Mercer's theorem [88] can therefore be expressed in an infinite expansion,

$$C_y(x_1, x_2) = \sum_{k=1}^{\infty} \lambda_k \varphi_k(x_1)\varphi_k(x_2)\,, \tag{5.4}$$

where λ_k and $\varphi_k(x)$ are the eigenvalues and orthogonal eigenfunctions of the covariance function. This result is significant because the second order random process defined by the mean and covariance functions in Eqs. (5.2) and (5.3) can be expressed in terms of a generalized Fourier series expansion of the eigenvalues and eigenfunctions of its covariance function.

Previous work done by Fichtl [90] assumed that the total cross section in a slab geometry neutron transport setting was considered a second order random process with a known covariance function. Using a KL transform truncated to include only K components, the eigenvalues and eigenfunctions were used to compute spatially dependent realizations of the cross section,

$$\sigma(x, \omega) = \langle \sigma(x) \rangle + \sum_{k=1}^{K} \sqrt{\lambda_k}\varphi_k(x)\xi_k(\omega)\,, \tag{5.5}$$

using zero-mean, unit-variance, uncorrelated random variables, $\xi_k(\omega)$. Although this work focused on covariances in the form of a known continuous function (i.e. exponentially distributed correlation function), the roadmap was established for transforming a random process into a useful form to compute realizations of the input quantities for use in uncertainty propagation applications.

Another aspect of the previous work done by Fichtl [90] concentrated on propagating uncertainties given in the form of a single random variable. This can be considered as a limiting case in the random process formulation, where all of the spatially varying cross section uncertainties are considered fully correlated leading to just a single spatially-independent random cross section, $\sigma(\omega)$. In this case, given the mean and variance of the cross section, computing realizations of a random variable are straight forward,

$$\sigma(\omega) = \langle\sigma\rangle + \sqrt{v_\sigma}\xi(\omega)\,, \tag{5.6}$$

where v_σ is the variance of the cross section and $\xi(\omega)$ remains a zero-mean, unit-variance, random variable. An extension to include multiple uncorrelated and independent random variables is straightforward where each random variable is independently sampled in the same fashion as in Eq. (5.6). Although these concepts are generally simple, they are important to understanding the covariance and how to sample from random variables and processes.

In the present work, the covariance of the PFNS is assumed to be known, given in the nuclear data libraries such as ENDF/B-VII.1 [1] in a discrete matrix form. The concepts introduced to handle a continuous covariance function are analogous to the methods used to manipulate a discrete covariance matrix, which are discussed in greater detail in the following sections.

5.1.1 Cholesky Decomposition

One method of manipulating the covariance matrix of an uncertain quantity is to perform a Cholesky decomposition on the covariance matrix [91]. Unlike the expected values shown in a continuous sense in Eqs. (5.2) and (5.3), the mean values in the discrete sense have slightly different notation, although the essence of the values remain the same. In the context of the PFNS, the covariance matrix is described by,

$$\mathbf{C} = \left\langle \vec{\chi}\,\vec{\chi}^{T} \right\rangle - \left\langle \vec{\chi} \right\rangle \left\langle \vec{\chi} \right\rangle^{T}, \tag{5.7}$$

where the PFNS is in now a vector quantity rather than a continuous function. Performing a Cholesky decomposition on the PFNS covariance matrix leads to,

$$\mathbf{C} = \mathbf{L}\mathbf{L}^{*}, \tag{5.8}$$

where $\mathbf{L}$ is a lower triangular matrix and $\mathbf{L}^{*}$ is its conjugate transpose. This decomposition of the covariance matrix is analogous to the single random variable example seen in Eq. (5.6) where the square root of the variance defines the range that the single random variable is sampled from. In the case where the covariance matrix in Eq. (5.8) is fully diagonal, the lower triangular matrix $\mathbf{L}$ would be fully diagonal with the square root of the variance occupying each of the diagonal entries. When off-diagonal entries exist in the covariance matrix, the Cholesky decomposition can be considered to be the square root of the covariance matrix where the correlations between the PFNS uncertainties are taken into account. Realizations of the PFNS using the Cholesky decomposition of the covariance matrix can be computed by,

$$\vec{\chi} = \left\langle \vec{\chi} \right\rangle + \mathbf{L}\vec{\xi}, \tag{5.9}$$

where $\vec{\xi}$ is a vector of independently sampled zero-mean, unit-variance, random variables.

In recent work by Fichtl and Prinja [99] and Rising *et al.* [92] the Cholesky decomposition has been shown to work for uncertainty quantification in a transport setting where the spatially dependent total cross section is assumed uncertain with a known covariance matrix. In Fig. 5.1 a few sample realizations of the total cross

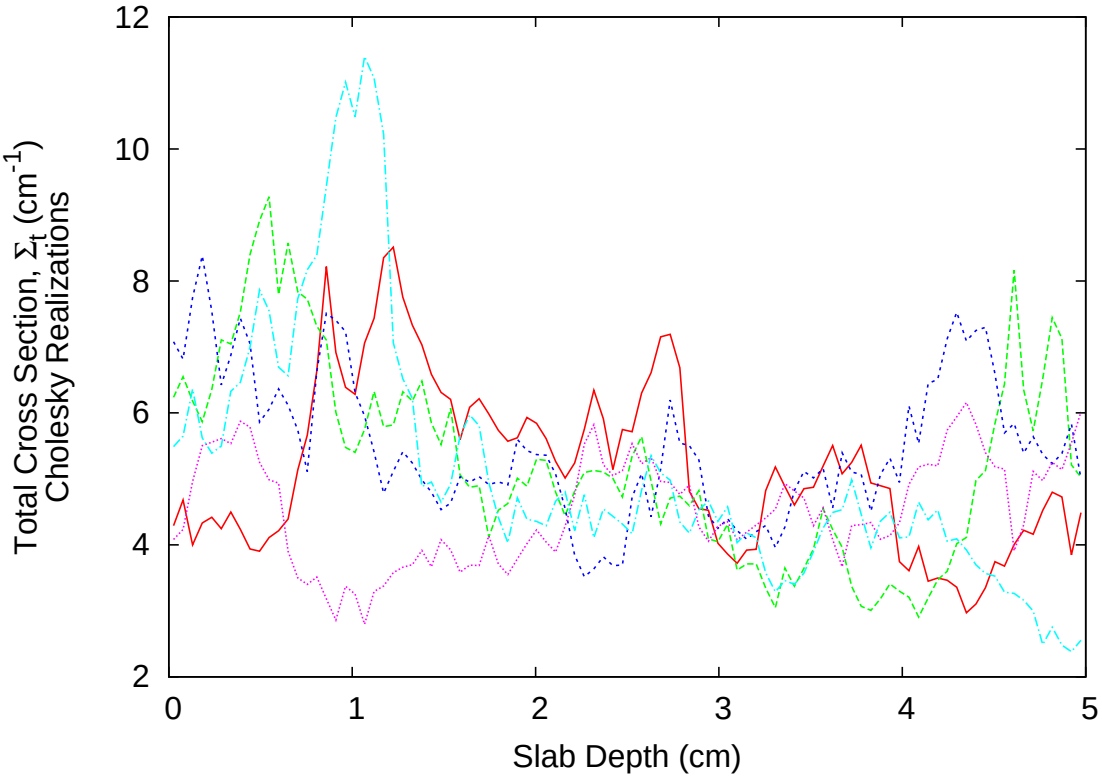

Figure 5.1: Sample realizations of the spatially uncertain total cross section used to propagate uncertainties in recent work [92].

section are shown from the previous work [92]. In that work, the total cross section is taken to be uncertain with a spatially constant mean and variance, and a spatially dependent correlation matrix in the form of an exponential distribution. The samples are computed using the same relationship in Eq. (5.9) for the total cross section after performing a Cholesky decomposition of the spatially varying covariance matrix and the random variables are sampled from a log-normal distribution. As can be seen in

Fig. 5.1, the random samples are very distinct in that they have some highly varying cross section values in neighboring spatial locations. Because the uncertainties in the previous work are considered to be present due to spatially varying material densities, the rapid variation in cross section values are acceptable and considered valid "realizations".

For the present work, applying the Cholesky decomposition to the PFNS covariance matrix is not considered an appropriate method for two reasons. First, the correlations in the uncertainties of the PFNS are present in the outgoing neutron energy grid, where the PFNS is expected to be smoothly varying and generally predictable in shape and magnitude. Therefore, realizations should not behave similarly to the cross section realizations in Fig. 5.1. The second reason why the Cholesky decomposition is not considered in the present work is because the number of random variables present in the uncertainties is determined entirely by the rank of the covariance matrix. In the present work, the size of the evaluated PFNS covariance matrix is up to a 643-by-643 matrix on the outgoing energy grid. Performing a Cholesky decomposition on a 643-by-643 covariance matrix would require 643 independent, uncorrelated random samples to populate the $\vec{\xi}$ vector in Eq. (5.9). As we will discuss in the following section, this kind of decomposition is overkill and we seek a dimension reduction method to use to propagate uncertainties.

5.1.2 Principal Component Analysis

An alternative method that can be used to decompose the covariance matrix is to perform a principal component analysis (PCA) [93, 94]. The PCA is an efficient dimension-reducing method by decomposing the covariance matrix into pairs of eigenvalues and eigenvectors ordering them from largest to smallest eigenvalue. The largest eigenvalue corresponds to the eigenvector with the largest uncertainty

and the smallest eigenvalue corresponds to the eigenvector with the smallest uncertainty. The advantage of using the PCA is that eigenvectors with very small corresponding eigenvalues can be neglected without excessively biasing the results. The PCA decomposition leads to a realization, χ_m, of the PFNS

$$\chi_m = \langle \chi \rangle + \sum_{k=1}^{K} \sqrt{\lambda}_k \vec{\varphi}_k \xi_{k,m} \,, \tag{5.10}$$

where λ_k is the k-th eigenvalue of the covariance matrix, $\vec{\varphi}_k$ is the k-th eigenvector of the covariance matrix, and $\xi_{k,m}$ is the k-th zero-mean, unit-variance, uncorrelated random variable for the m-th realization. The PCA expansion requires K independent samples for each realization where K is the number of eigenmodes kept in the expansion. This method can be considered to be analogous to the discrete form of the continuous KL expansion making it possible to decompose discrete covariance matrices that are generally the result of the nuclear data uncertainty quantification efforts.

In recent work by Rising *et al.* [92, 95] the PCA technique has been shown to work for uncertainty quantification in a transport setting where the spatially dependent total cross section is assumed uncertain with a known covariance matrix. In Fig. 5.2 some sample realizations of the total cross section are shown from the previous work [92]. The total cross section is taken to be uncertain with a spatially constant mean and variance, and a spatially dependent correlation matrix in the form of an exponential distribution. The samples are computed using the same relationship in Eq. (5.10) for the total cross section after performing a PCA on the spatially varying covariance matrix and the random variables are sampled from a log-normal distribution. As can be seen in Fig. 5.2, the random samples are much smoother in their variation throughout the slab compared with the Cholesky decomposition realizations in Fig. 5.1.

In the present work, the PCA is the chosen method to decompose both the

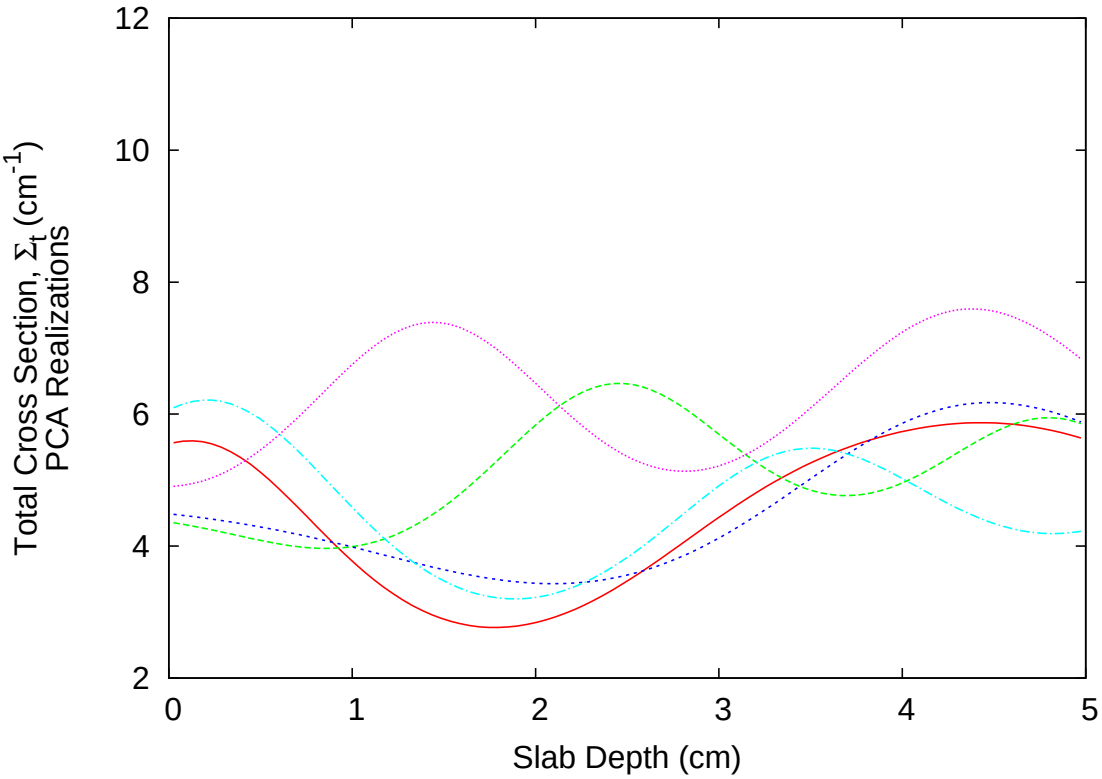

Figure 5.2: Sample realizations of the spatially uncertain total cross section used to propagate uncertainties in recent work [92].

PFNS and model parameter covariance matrices to obtain realizations either directly or through the sampled LA model parameters. This method will also allow the dimensionality of the random PFNS to be reduced significantly to only a handful of principal components while retaining nearly all of the uncertainty in the original formulation of the covariance matrices.

5.2 Forward Propagation Methods

5.2.1 Sampling-based Methods

In the present research, sampling-based methods [96] are chosen as the primary method to quantify uncertainties in the integral quantities for the fast-critical assemblies described in Ch. 2.1. Unlike perturbation methods and sensitivity analyses, the sampling-based methods are capable of propagating large input uncertainties while quantifying the uncertainties in the higher-order moments and probability density functions of the output quantities. Within the field of sampling-based methods there exists many variants of the Monte Carlo method including the standard "brute force" approach, Markov Chain methods [61, 62], and the more recently studied approach, the Latin Hypercube sampling method [97, 91]. All of these methods have been used in various applications to propagate uncertainties in a forward manner by sampling from underlying uncertainty distributions of the input quantities with the goal of adequately characterizing the response of some integral quantities of interest.

In the present work, the standard "brute force" Monte Carlo direct sampling approach will be the method of choice among the sampling-based methods because this method is generally taken to be the "gold" standard in terms of comparisons made to other more computationally inexpensive methods.

5.2.2 Unified Monte Carlo and Total Monte Carlo

This work is a combination of the unified Monte Carlo (UMC) method being used for uncertainty quantification with the total Monte Carlo (TMC) method described earlier in the Ch.3. Mentioned previously, the problem with the TMC method, that has been developed making use of the TALYS code package, is that the experimental

data are not explicitly used like in the generalized least-squares approach. The use of the UMC method in combination with the TMC method would offer a great comparison to the covariance sampling method, described in the previous section, which samples from the posterior covariance matrix to obtain individual realizations of a nuclear reaction. This new, UMC+TMC, method samples from the prior parameter covariance matrix and then takes the experimental data into account in the same way that the UMC approach works. Then, instead of calculating the mean and covariance matrix right away, the sampled realization will be propagated through the critical assembly transport simulation. This method bypasses the covariance matrix which requires an assumption to be made on the shape of the underlying PDF. Therefore the UMC+TMC method will only differ from the covariance matrix sampling when the LA model calculation is sufficiently nonlinear or the underlying shape of the covariance matrix is not a multivariate Gaussian distribution.

Using this new approach on propagating uncertainties in the PFNS using the LA model on a real transport simulation is a unique contribution to the field of uncertainty quantification and propagation.

5.2.3 Polynomial Chaos Expansion

Use of stochastic spectral methods for representing both input and output variable uncertainties has come to be recognized as a powerful uncertainty quantification (UQ) approach that integrates well with both deterministic and stochastic (Monte Carlo) numerical techniques and codes that have been developed for applications in the absence of uncertainty [89, 98, 99, 100, 101]. In this approach, given a finite dimensional input random vector representing the uncertain data or model parameters, output variables are expanded in an appropriate family of random polynomials, so-called polynomial chaos expansions, and collocation or projection methods applied

to generate independent or coupled equations for the deterministic expansion coefficients. Existing codes are then directly used or modified somewhat to solve for the expansion coefficients and the polynomial chaos representation then provides a complete statistical characterization of the output uncertainty. Means, variances, auto- and cross-covariances, as well as probability densities, all associated with output variables, are obtained by fairly routine post-processing of the output statistics.

One method that has been known to be very efficient in characterizing uncertainties in the integral quantities for various types of problems is the Polynomial Chaos Expansion (PCE) method. It is used to expand the unknowns in the random transport problem (i.e. flux, multiplication factor, spectral indices, etc.) in terms of the same statistical distributions chosen to describe the uncertain input quantities. The original Wiener polynomial chaos, or homogeneous polynomial chaos [102], employed Hermite polynomials when the random process is described by a multivariate Gaussian distribution. Later, the Wiener-Askey polynomial chaos, or generalized polynomial chaos (gPC) [89, 98] was expanded to employ other orthogonal polynomials for a broad class of non-Gaussian multivariate random variable distributions. The most suitable choice of polynomials to expand the unknowns is determined from the distribution of the uncertain input quantities. For example, with the random variables having a normal distribution, the optimal gPC expansion choice is Hermite chaos, while for random variables having a uniform distribution, the gPC expansion choice is Legendre chaos. The remainder of this section will describe the gPC expansion methodology applied to the problem of interest in terms of a set of general multivariate orthogonal polynomials, $\mathbf{G}$, used to characterize the distribution of the solution given the uncertainties are described by a known distribution.

The output quantities of interest, the multiplication factor, k_{eff}, and the angular flux, ψ, in the transport equation can be expressed as multidimensional functions of

the underlying random variables,

$$k_{eff}(\omega) = k_{eff}\left(\xi_1(\omega), \xi_2(\omega), \cdots, \xi_K(\omega)\right) , \tag{5.11}$$

$$\psi(\vec{r}, E, \hat{\Omega}, \omega) = \psi\left(\vec{r}, E, \hat{\Omega}, \xi_1(\omega), \xi_2(\omega), \cdots, \xi_K(\omega)\right) , \tag{5.12}$$

where the statistics of the multiplication factor and angular flux can be expressed in terms of some general multivariate orthogonal polynomials, $\mathbf{G}_n$. The expansion of the effective multiplication factor is then,

$$\begin{aligned} k_{eff}(\omega) = & k_0\mathbf{G}_0 + \sum_{i_1=1}^{\infty} k_{i_1}\mathbf{G}_1(\xi_{i_1}) + \sum_{i_1=1}^{\infty}\sum_{i_2=1}^{i_1} k_{i_1,i_2}\mathbf{G}_2(\xi_{i_1},\xi_{i_2}) \\ & + \sum_{i_1=1}^{\infty}\sum_{i_2=1}^{i_1}\sum_{i_3=1}^{i_2} k_{i_1,i_2,i_3}\mathbf{G}_3(\xi_{i_1},\xi_{i_2},\xi_{i_3}) + \cdots , \end{aligned} \tag{5.13}$$

while the expansion of the angular flux is then,

$$\begin{aligned} \psi(\vec{r}, E, \hat{\Omega}, \omega) = & \psi_0(\vec{r}, E, \hat{\Omega})\mathbf{G}_0 + \sum_{i_1=1}^{\infty} \psi_{i_1}(\vec{r}, E, \hat{\Omega})\mathbf{G}_1(\xi_{i_1}) \\ & + \sum_{i_1=1}^{\infty}\sum_{i_2=1}^{i_1} \psi_{i_1,i_2}(\vec{r}, E, \hat{\Omega})\mathbf{G}_2(\xi_{i_1},\xi_{i_2}) \\ & + \sum_{i_1=1}^{\infty}\sum_{i_2=1}^{i_1}\sum_{i_3=1}^{i_2} \psi_{i_1,i_2,i_3}(\vec{r}, E, \hat{\Omega})\mathbf{G}_3(\xi_{i_1},\xi_{i_2},\xi_{i_3}) + \cdots . \end{aligned} \tag{5.14}$$

The infinite expansion of the unknowns needs to be truncated with respect to the number of random variables, K, and the number of polynomials, P, used to describe the random dimension, leading to,

$$\begin{aligned} k_{eff}(\omega) = & k_0\mathbf{G}_0 + \sum_{i_1=1}^{K} k_{i_1}\mathbf{G}_1(\xi_{i_1}) + \sum_{i_1=1}^{K}\sum_{i_2=1}^{i_1} k_{i_1,i_2}\mathbf{G}_2(\xi_{i_1},\xi_{i_2}) + \cdots \\ & + \sum_{i_1=1}^{K}\sum_{i_2=1}^{i_1}\cdots\sum_{i_P=1}^{i_{P-1}} k_{i_1,\cdots,i_P}\mathbf{G}_P(\xi_{i_1},\cdots,\xi_{i_P}) , \end{aligned} \tag{5.15}$$

for the effective multiplication factor and,

$$\begin{aligned}\psi(\vec{r},E,\hat{\Omega},\omega) &= k_0\mathbf{G}_0+\sum_{i_1=1}^{K}\psi_{i_1}(\vec{r},E,\hat{\Omega})\mathbf{G}_1(\xi_{i_1})\\ &\quad+\sum_{i_1=1}^{K}\sum_{i_2=1}^{i_1}\psi_{i_1,i_2}(\vec{r},E,\hat{\Omega})\mathbf{G}_2(\xi_{i_1},\xi_{i_2})+\cdots\\ &\quad+\sum_{i_1=1}^{K}\sum_{i_2=1}^{i_1}\cdots\sum_{i_P=1}^{i_{P-1}}\psi_{i_1,\cdots,i_P}(\vec{r},E,\hat{\Omega})\mathbf{G}_P(\xi_{i_1},\cdots,\xi_{i_P})\,, \qquad (5.16)\end{aligned}$$

for the angular flux. By truncating the number of random variables to K, some information about the random process is lost, whereas truncating the polynomial expansion order to P, limits the ability to capture higher moment features of the unknowns. The total number of terms in the expansion of the multiplication factor grows as the values chosen for K and P increase,

$$(P_t+1)=\frac{(K+P)!}{K!P!}\,, \qquad (5.17)$$

where P_t is defined in this manner such that with a single random variable it is the maximum polynomial order. A compact form of the gPC expansion of the unknowns can be written as

$$k_{eff}(\omega) = \sum_{i=0}^{P_t} k_i\tilde{\mathbf{G}}_i(\vec{\xi}(\omega))\,, \qquad (5.18)$$

$$\psi(\vec{r},E,\hat{\Omega},\omega) = \sum_{i=0}^{P_t}\psi_i(\vec{r},E,\hat{\Omega})\tilde{\mathbf{G}}_i(\vec{\xi}(\omega))\,. \qquad (5.19)$$

To proceed further, some properties of the multivariate orthogonal polynomials need to be established. The inner product of two functions, f and g, depending on the random variables, $\vec{\xi}$, with support from $\vec{a}$ to $\vec{b}$, is defined as

$$\langle f,g\rangle=\int_{a_1}^{b_1}d\xi_1\cdots\int_{a_K}^{b_K}d\xi_K P(\vec{\xi})f(\vec{\xi})g(\vec{\xi})\,, \qquad (5.20)$$

where $P(\vec{\xi})$ is the weight function and is defined as the joint probability distribution of the random variables. Given that the random variables, $\vec{\xi}$, are independent from one another, the joint probability distribution factors into a product of univariate probability distributions,

$$P(\vec{\xi}) = P(\xi_1)P(\xi_2)\cdots P(\xi_K)\,, \tag{5.21}$$

leading to,

$$\langle f, g\rangle = \int_{a_1}^{b_1} d\xi_1 P(\xi_1)\cdots\int_{a_K}^{b_K} d\xi_K P(\xi_K) f(\vec{\xi}) g(\vec{\xi})\,. \tag{5.22}$$

In the case when f and g are both in the same family of general multivariate orthogonal polynomials, $\mathbf{G}$, then the orthogonality condition is

$$\langle \mathbf{G}_i, \mathbf{G}_j\rangle = \left\langle \mathbf{G}_i^2\right\rangle \delta_{ij}\,. \tag{5.23}$$

The expansion of the unknowns, specifically the multiplication factor, k_{eff}, and angular flux, ψ, shown in Eqs. (5.18) and (5.19), respectively, can be directly substituted into the transport equation in Eq. (2.1) leading to an unfamiliar transport-like equation. By taking Galerkin projections of the new transport equation in the random dimension, a coupled set of transport equations results, leading to the stochastic finite element method (SFEM) [89]. Because this method is intrusive by requiring a new algorithm for solving the SFEM equations, we seek an alternative approach that can utilize the existing transport solvers available.

Stochastic Collocation Method

Polynomial chaos expansions (PCE) in conjunction with the stochastic collocation method (SCM) [103] was recently demonstrated [100, 92] to be a highly a effective

method of propagating uncertainty in the total cross section modeled as a statistically well-characterized spatial random process. A truncated Karhunen-Loéve (KL) expansion [89] was used to replace this infinite dimensional spatial stochastic process by a finite number of random variables for a given covariance function. The angular flux was expanded in a homogeneous chaos, corresponding to an expansion in terms of multidimensional random Hermite polynomials [102, 89] and direct random sampling as well as tensor and sparse grid quadrature based stochastic collocation techniques were used to relate the expansion coefficients to solutions of independent deterministic transport equations. Post-processing of the random polynomial representation then provided means, variances and probability densities of various output quantities of interest, and the computational advantages of PCE-SCM over direct random sampling demonstrated with respect to polynomial chaos expansion order and quadrature order.

The SCM is a non-intrusive method to propagate uncertainties, without changing the underlying solution method of the transport problem. The inner product of the expansion in Eqs. (5.18) and (5.19) is taken before it is inserted into the transport equation. Utilizing the orthogonality of the chosen general orthogonal polynomial basis functions in Eqs. (5.20)–(5.23), the unknown coefficients of the expanded multiplication factor and angular flux can be found by computing the inner products,

$$k_p = \frac{\left\langle \mathbf{G}_p, k_{eff}(\omega) \right\rangle}{\left\langle \mathbf{G}_p^2 \right\rangle}, \tag{5.24}$$

$$\psi_p(\vec{r}, E, \hat{\Omega}) = \frac{\left\langle \mathbf{G}_p, \psi(\vec{r}, E, \hat{\Omega}, \omega) \right\rangle}{\left\langle \mathbf{G}_p^2 \right\rangle}. \tag{5.25}$$

Based on the expansion of the average PFNS in the random dimension, ω, in Eq. (5.10), the transport solution unknowns can be computed. These transport solution unknowns are then used to compute the SCM coefficients in Eqs. (5.24) and (5.25). Either a Monte Carlo method or an appropriate quadrature method can

be used to approximate the integral quantity coefficients of the transport solution unknowns.

Note that the effective multiplication factor and the angular flux have been used as just an example of the unknown integral quantities of interest in the random transport problem. This very same procedure for obtaining the coefficients in Eqs. (5.24) and (5.25) can be used for calculating the coefficients of many more quantities of interest including the scalar flux, current, reaction rates, spectral indices, leakage, point reactor kinetics equation parameters, etc.

Tensor Product Gauss Quadrature

Gauss quadrature methods are optimal in the sense that for a Gauss quadrature set of order M, the integral of a univariate polynomial up to order $2M-1$ will be exactly computed. The Gauss quadrature methods that we are interested in will accurately compute an integral of the form,

$$\int_a^b dx\, w(x) f(x) \approx \sum_{i=1}^{M} w_i f(x_i)\,, \tag{5.26}$$

given the function $f(x)$ can be well approximated by an order $2M-1$ polynomial and that $w(x) = e^{-x^2/2}$, $a = -\infty$ and $b = \infty$ for a Gauss-Hermite quadrature and $w(x) = 1$, $a = -1$ and $b = 1$ for a Gauss-Legendre quadrature. In this work we rely on the fact that each multivariate polynomial can be expanded into a product of several univariate polynomials (Eq. (5.21)) and that the arguments of the multivariate polynomial are independent and uncorrelated. This allows the inner product shown in Eq. (5.22) to be well approximated as a tensor product of Gauss quadrature sets,

$$\int_{a_1}^{b_1} d\xi_1 w(\xi_1) \cdots \int_{a_K}^{b_K} d\xi_K w(\xi_K) f(\vec{\xi}) g(\vec{\xi}) \approx \sum_{i_1=1}^{M_1} w_{i_1} \cdots \sum_{i_K=1}^{M_K} w_{i_K} f(\vec{\xi}) g(\vec{\xi})\,, \tag{5.27}$$

given that the quantity $f(\vec{\xi})g(\vec{\xi})$ is well approximated by an order $2M_i - 1$ polynomial in the i-th dimension for $i = 1, ..., K$. Note that in this work, only a single distribution type at a time will be used for all random variables while in theory it is possible to simultaneously use separate distributions in each random dimension.

Chapter 6

Uncertainty Propagation: Numerical Results

Currently, with the availability of newly evaluated nuclear data uncertainties and the amount of computing power needed to propagate uncertainties through complex simulations, the next step is to quantify the uncertainties of the integral quantities of the critical assemblies described in Chapter 2.1. In Chapter 5 the methods available for uncertainty propagation were reviewed with the primary focus on the methods utilized in the present work.

In the following section we study the recently released PFNS covariance matrices for the n+^{235}U, calculated by the author of this work, and the n+^{239}Pu fission reactions in the ENDF/B-VII.1 [1] nuclear data library. The evaluated uncertainties in these two major actinides are propagated through two very well known critical assemblies, Lady Godiva and Jezebel, and several integral quantities of each assembly are investigated using both the standard brute force Monte Carlo approach and polynomial chaos expansion with the stochastic collocation method. In Chapter 6.2.1, the uncertainties quantified in Chapter 4.1 for the suite of uranium isotopes are prop-

agated through the Big Ten critical assembly where the focus is on comparing the differences when the actinides are considered correlated and uncorrelated. Last, the results of the implemented Unified Monte Carlo approach combined with the Total Monte Carlo approach (UMC+TMC) is shown for the Flattop assemblies. This new method is compared with the standard brute force approach where the samples are calculated from the posterior model parameter covariance matrices that were quantified for the uranium and plutonium actinide suites described in Chapter 4.1.

6.1 ENDF/B-VII.1 PFNS Uncertainty Propagation

The present work focuses on a couple of very well known fast critical assemblies including the solid, bare, highly enriched uranium (HEU) sphere, Lady Godiva [15] and the solid, bare, plutonium sphere, Jezebel [16]. Of course, for the neutron transport codes to perform adequately the nuclear data needs to be well known for the materials in each assembly. Recently, the ENDF/B-VII.1 nuclear data library [1] was released including the evaluated covariance matrices of the PFNS for the n+^{235}U, n+^{238}U and n+^{239}Pu reactions below the second-chance fission threshold energy. In the evaluation work to quantify the uncertainties, the mean value of the PFNS was left unchanged from the previous ENDF/B-VII.0 data library release [63]. Because the MCNP5-1.60 [30] transport code release includes the ENDF/B-VII.0 nuclear data, the given data will be used for all transport calculations utilizing the ENDF/B-VII.1 covariance matrices for computing realizations of the PFNS.

Without a significant neutron moderating mechanism in place, both the Lady Godiva and Jezebel assemblies are considered fast neutron critical assemblies. In order to determine if these experiments are well suited to demonstrate the impact

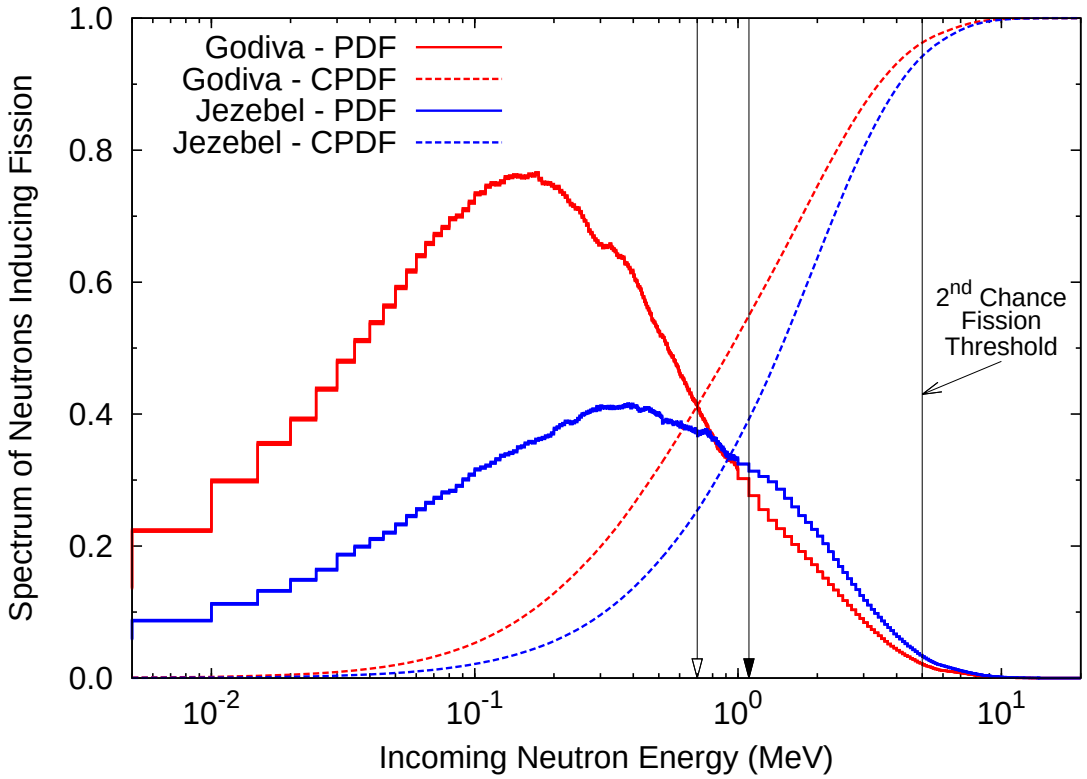

Figure 6.1: The MCNP5-1.60 calculated probability density function (PDF) and cumulative probability density function (CPDF) of neutrons inducing fission in each of the Lady Godiva and Jezebel assemblies using the ENDF/B-VII.0 nuclear data library. The vertical unfilled arrow marks approximately where the n+^{237}Np(n,f) threshold exists and the vertical filled arrow marks approximately where the n+^{238}U(n,f) threshold exists.

of the uncertainties coming from the average PFNS below the second chance fission threshold energy the assemblies were run through the MCNP5-1.60 calculation to obtain the spectrum of neutrons inducing fission, shown in Fig. 6.1. The probability that a fission event is induced by a neutron with less than 5-MeV energy is calculated to be 96.3% and 94.2% for the Lady Godiva and Jezebel assemblies, respectively. Therefore, the Lady Godiva and Jezebel benchmarks are considered appropriate critical assemblies for the propagation of the average PFNS uncertainties below the second-chance fission threshold energy.

For the Lady Godiva fast critical assembly the n+^{235}U PFNS uncertainties are propagated and for the Jezebel fast critical assembly the n+^{239}Pu PFNS uncertainties are propagated through MCNP5-1.60 and several integral quantities are computed. First, the effective multiplication factor, k_{eff} in Eq. (2.1), and the total leakage defined in Eq. (2.3) are computed. The value for k_{eff} is an extremely important quantity in reactor physics and criticality safety applications. The value for the leakage is also important in reactor physics applications as well as in radiation shielding applications for health safety reasons. Along with the effective multiplication factor and the total leakage, several spectral indices have been calculated. These quantities are computed at the very center of the Lady Godiva and Jezebel spheres and are the result of folding the neutron spectrum in the angular flux into the neutron-induced fission cross section reaction in Eqs. (2.5)–(2.7). Because the neutron induced fission cross section is very well known for the ^{235}U(n,f) reaction, the spectral indices are defined as ratios to the ^{235}U(n,f) reaction. These reactions are of particular interest because both the ^{238}U and ^{237}Np fission reactions are threshold reactions that require a minimum incident energy for the reactions to even occur, and the ^{239}Pu fission reaction is well known much like the ^{235}U fission reaction. By studying these reactions we can infer information about the magnitude of the neutron spectrum for different energy ranges inside the critical assembly.

6.1.1 Principal Component Analysis

By studying the eigenvalues of the PFNS covariance matrix shown in Fig. 6.2, the number of principal components needed in the expansion can be estimated. In this case, because the evaluation of the uncertainties uses the LA model with very few tunable parameters, it isn't surprising that the evaluated covariance matrix only has a few dominant eigenvalues. From Fig. 6.2, we can say that a maximum of 3 to 4 eigenmodes is needed.

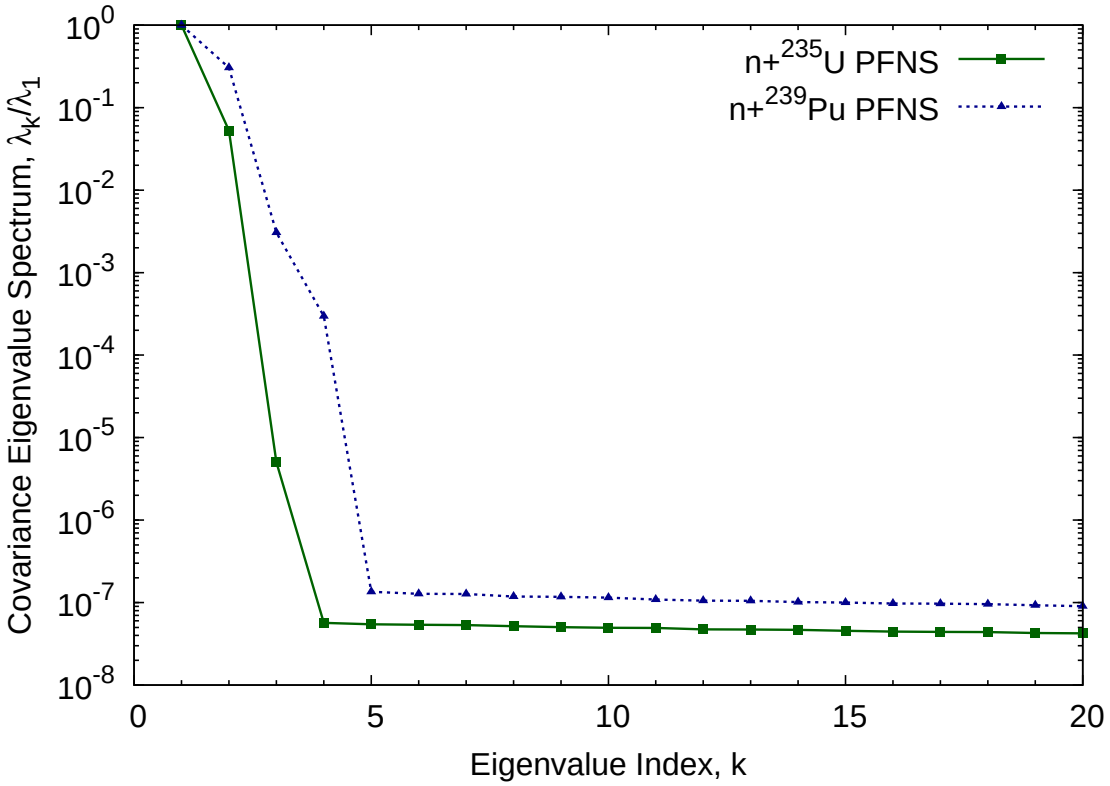

Figure 6.2: The first several eigenvalues, λ_k, of the PFNS covariance matrix for the n+^{235}U and n+^{239}Pu reactions.

A more quantitative manner to determine the appropriate number of principal components needed in the expansion is to compute the relative standard deviation and the correlation matrix of the PCA expansion depending on the expansion order, K. Because the $\xi_{k,m}$ are zero-mean, unit-variance, uncorrelated random variables, the relative standard deviation of the PFNS, $\vec{\sigma}_\chi$, can be computed exactly,

$$\vec{\sigma}_\chi = \frac{\sum_{k=1}^{K} \sqrt{\lambda}_k \vec{\varphi}_k}{\langle \vec{\chi} \rangle} \,. \tag{6.1}$$

In the case of n+^{235}U PFNS, the resulting relative uncertainties in Fig. 6.3 have already converged for $K = 2$ principal components and the remaining differences are

negligible and are not expected to effect the uncertainties in the computed integral quantities. Also, in the case of the n+^{239}Pu PFNS, an expansion up to $K = 3$ is needed. The differences between the n+^{235}U and n+^{239}Pu PFNS relative uncertainties are due to the "model uncertainty" corrections applied during the n+^{239}Pu PFNS uncertainty evaluation [66] effectively adding an additional eigenmode to the evaluated covariance matrix.

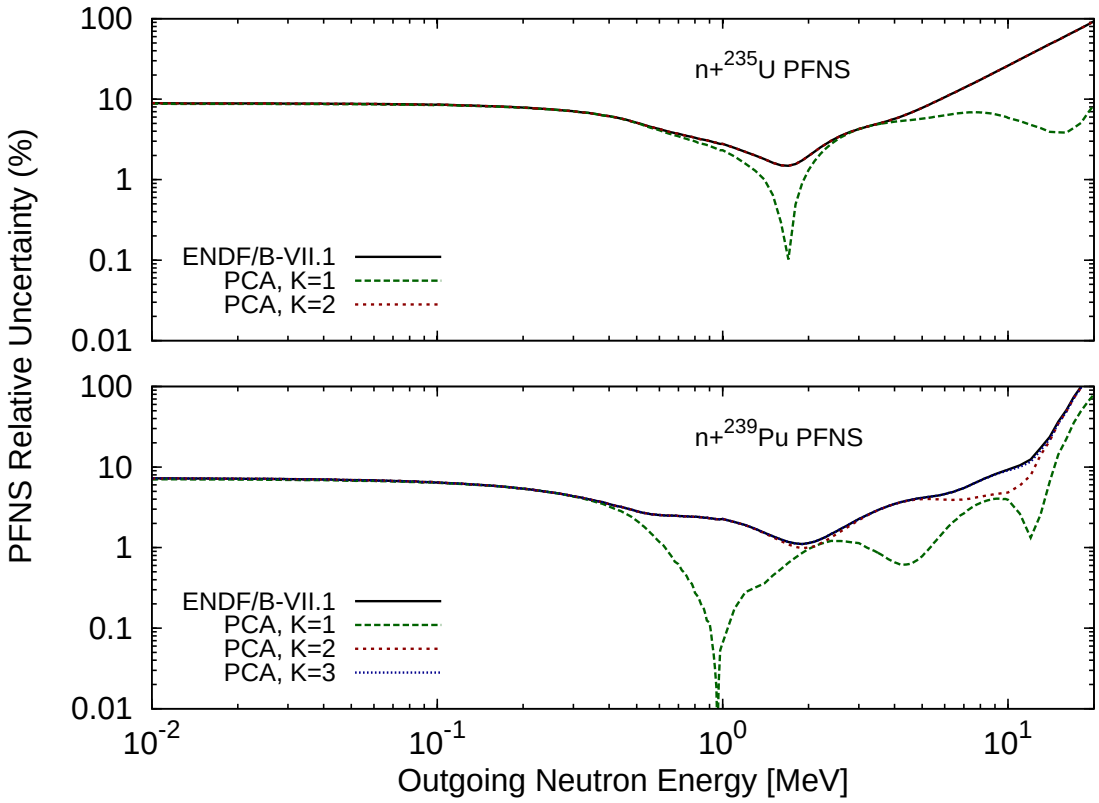

Figure 6.3: The reconstructed relative standard deviation of the n+^{235}U and n+^{239}Pu PFNS reactions depending on the PCA expansion order, K.

The correlation matrix of the PFNS, ρ, can also be reconstructed based on the expansion order, K. The elements of the correlation matrix are defined in terms of

the elements of the covariance matrix,

$$\rho_{ij} = \frac{C_{ij}}{\sqrt{C_{ii}C_{jj}}}\,, \tag{6.2}$$

where the values are bounded, $-1 \leq \rho_{ij} \leq 1$. Similar to the total PFNS uncertainty in Eq. (6.1), the covariance matrix of the PFNS, $\mathbf{C}$, can be exactly computed by,

$$\mathbf{C} = \sum_{k=1}^{K} \lambda_k \vec{\varphi}_k \vec{\varphi}_k^T\,, \tag{6.3}$$

depending on the PCA order, K. In Fig. 6.4, the correlation matrices for the n+^{235}U

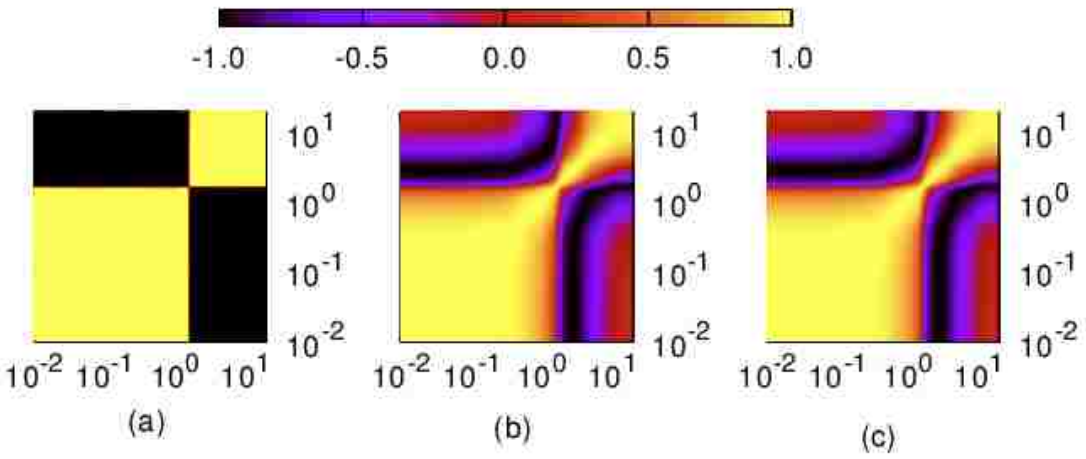

Figure 6.4: The reconstructed correlation matrix of the n+^{235}U PFNS depending on the PCA expansion order; (a) $K = 1$, (b) $K = 2$ and (c) ENDF/B-VII.1 library. Note that the axes on all plots are for the outgoing neutron energy in MeV.

PFNS for $K = 1$ (a) and $K = 2$ (b) are compared to the original ENDF/B-VII.1 matrix (c). Again, the result for $K = 2$ is nearly identical to the original evaluated matrix. By qualitatively looking at the eigenvalue spectrum of the covariance matrix, the total PFNS uncertainties and the correlation matrix resulting from the PCA decomposition, we can be certain that the most important components of the

uncertainties in the PFNS covariance matrix are being faithfully propagated through the transport simulations given a sufficient number of principal components are kept in the expansion.

The n+^{239}Pu PFNS covariance matrix yields the same general results from the qualitative analysis shown in this section for the n+^{235}U PFNS reaction, except that 3 eigenmodes are needed instead of 2. In conclusion, the number of principal components necessary to model the evaluated uncertainties in the ENDF/B-VII.1 library is between 2–3 for the n+^{235}U PFNS reaction and is between 2–4 for the n+^{239}Pu PFNS reaction. To benefit from effectively reducing the dimensionality of the PFNS covariance matrix, an efficient uncertainty propagation method when few random variables are present is utilized and compared against the computationally expensive direct sampling methods.

6.1.2 Sampling PFNS Covariance Matrices

One difficulty in sampling from the PFNS covariance matrices is the fact that the relative uncertainties are large for very high outgoing energies. Figure 6.3 shows that the relative standard deviation reaches 100% or greater at 20 MeV outgoing neutron energies. When sampling from a Gaussian or uniform distribution, any PFNS realization could become negative with such large relative uncertainties. Unfortunately, because of the mathematical properties of a probability density function, and the fact that negative values for a PFNS are unphysical, an alternate method for propagating these uncertainties must be utilized.

The first option would be to choose a distribution that would lead to positive realizations only. One such distribution would be the log-normal distribution which has been heavily studied previously in uncertainty propagation work when large uncertainties exist [100, 65]. As will be discussed next, this option would give positive

realizations only.

Two other options include biasing either the Monte Carlo or SCM sampling methods. The first biasing method that we consider is throwing out any realization with negative PFNS values. The problem with this method arises for the SCM sampling methods because the quadrature sets are generally small compared with the brute force sampling. If we throw out quadrature points in the SCM quadrature, then the coefficients in Eqs. (5.24) and (5.25) quickly begin skewing away from their intended meaning and would lead to significantly different results for the moments and distributions of the integral quantities. Therefore, this method is considered unacceptable and will not be used in the present work.

To avoid changing the underlying distribution from which the realizations are being computed and to avoid heavily biasing the sampling method we choose to slightly bias the sampling method by setting the PFNS to zero where the realization is negative in the outgoing energy spectrum and renormalizing over the entire range of the PFNS. The justification for this sampling method can be seen in Fig. 6.5 where the sampled mean and standard deviations are only slightly altered from their exact mean and standard deviations. Also, this biasing only effects the high outgoing energies (> 10 MeV) where the absolute PFNS values are several orders of magnitude lower than the average PFNS in the 1–3 MeV outgoing energy range and the relative uncertainties are large indicating that the actual values for the PFNS at high energies are very uncertain.

6.1.3 Lady Godiva Critical Assembly

The Lady Godiva fast critical assembly [15] is a metallic, spherical assembly with an approximate radius of 8.7407 cm highly enriched in ^{235}U with small amounts of ^{238}U and ^{234}U. The n+^{235}U PFNS uncertainties are propagated through the Lady Godiva

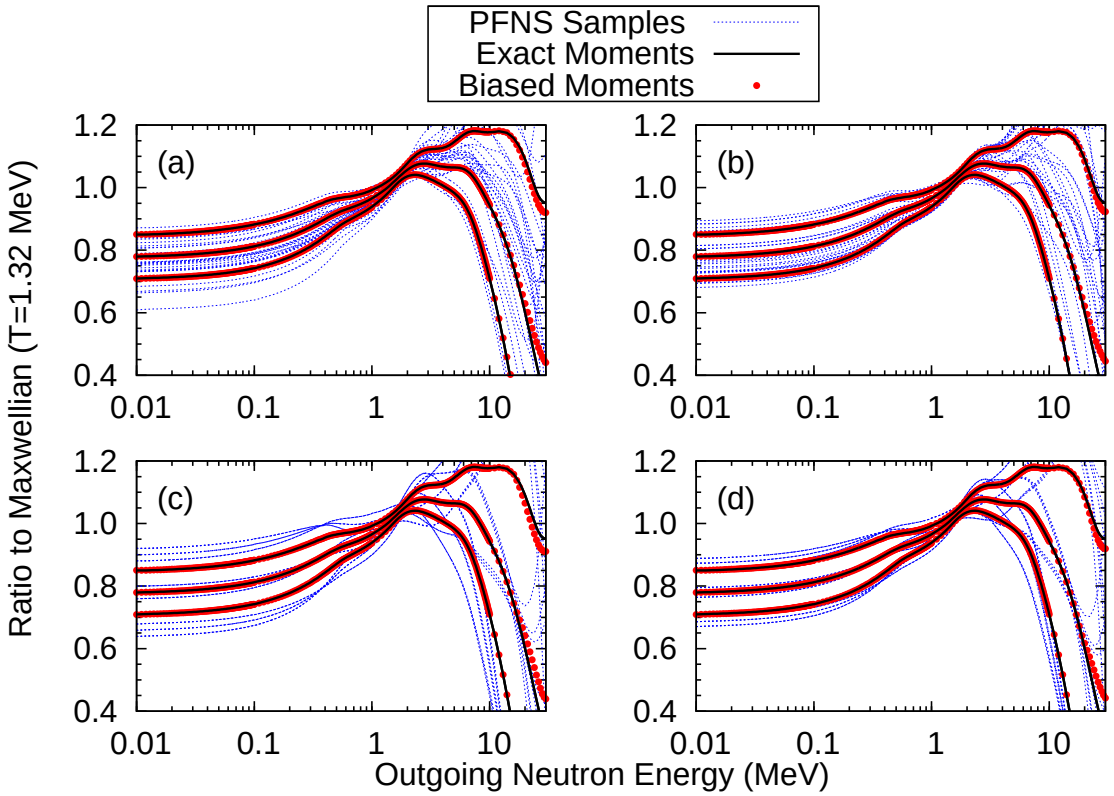

Figure 6.5: PFNS realizations, exact mean and standard deviations, and biased mean and standard deviations for (A) Gaussian distribution with Monte Carlo realizations, (B) uniform distribution with Monte Carlo realizations, (C) Gaussian distribution with Gauss-Hermite quadrature realizations and (D) uniform distribution with Gauss-Legendre quadrature realizations.

critical assembly and from Fig. 6.3 the necessary number of principal components needed to adequately propagate the modeled uncertainties is estimated to be $K = 2$.

Table 6.1 shows the results of propagating the uncertainties in the n+^{235}U PFNS using up to three principal components and assuming the principal components are independent random variables with a Gaussian distribution. The direct sampling results were obtained by computing 10,000 realizations of the PFNS where the stochastic collocation method results were obtained using the Gauss-Hermite quadrature with 4^K quadrature points. Because the integral values computed using

Integral Quantitiy	Direct Sampling (10^4) MC Statistics*	Principal Components $K=1$	$K=2$	$K=3$
k_{eff}	0.0001%	0.1037%	0.2347%	0.2345%
Leakage	0.0001%	0.2079%	0.2140%	0.2144%
$\mathcal{I}^{(238f)}$	0.0032%	3.1290%	3.3595%	3.3572%
$\mathcal{I}^{(239f)}$	0.0020%	0.2420%	0.2435%	0.2433%
$\mathcal{I}^{(237f)}$	0.0023%	1.3296%	1.3343%	1.3323%
Integral Quantitiy	Stochastic Collocation Method (4^K) MC Statistics*	Principal Components $K=1$	$K=2$	$K=3$
k_{eff}	0.0053%	0.1069%	0.2386%	0.2327%
Leakage	0.0042%	0.2123%	0.2100%	0.2128%
$\mathcal{I}^{(238f)}$	0.1320%	3.0891%	3.4052%	3.3884%
$\mathcal{I}^{(239f)}$	0.0818%	0.2409%	0.2501%	0.2437%
$\mathcal{I}^{(237f)}$	0.0944%	1.3023%	1.3627%	1.3401%
* Calculation based on $K=2$ principal components.				

Table 6.1: Lady Godiva relative uncertainties: k_{eff}, total leakage, and $\mathcal{I}^{(238f)}$, $\mathcal{I}^{(237f)}$ and $\mathcal{I}^{(239f)}$ spectral indices assuming a Gaussian distribution for the principal components. Note that the number of transport solutions for each method are indicated in parentheses.

MCNP5-1.60 inherently have some statistical noise, the Monte Carlo statistics column displays the statistical uncertainty in the calculation of each integral value. In all of the following cases the direct sampling statistics are much smaller compared with the SCM statistics because of disparity in the number of realizations used in calculating the moments of each integral value. The remaining columns in Table 6.1 present the ratio of the standard deviation to the mean based on the PFNS uncertainties. In general, as long as the standard deviation of the integral value distribution is large compared with the Monte Carlo statistics, the uncertainties in the data can be propagated using a Monte Carlo transport code such as MCNP5-1.60.

The probability density function of the k_{eff} integral value resulting from the propagation of the Gaussian distributed n+^{235}U PFNS uncertainties can be seen in

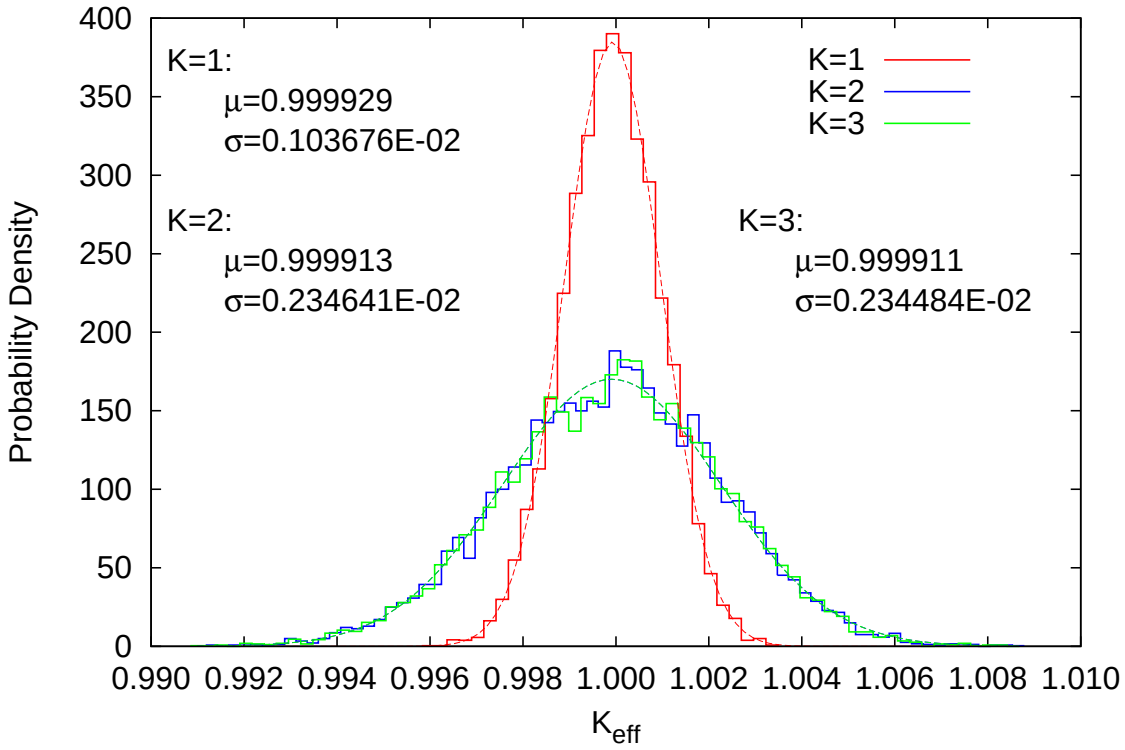

Figure 6.6: The probability density function of the effective multiplication factor, k_{eff}, for the Lady Godiva fast critical assembly resulting from propagating the n+^{235}U PFNS uncertainties through MCNP5-1.60 with 10,000 PFNS realizations.

Fig. 6.6. Along with the plotted probability density functions, all of the mean and standard deviation values are listed in Fig. 6.6 with the dashed lines representing Gaussian distributions with the computed mean and standard deviations listed. Out of all of the integral parameters listed in Table 6.1, the k_{eff} uncertainty has the largest relative change from $K = 1$ to $K = 2$ principal components. This can be explained by the difference in modeled uncertainties in $K = 1$ and $K = 2$ principal components (see Fig. 6.3), where in the 1–3-MeV outgoing neutron energy range the majority of neutrons are born, the k_{eff} can be significantly altered by a change in the PFNS shape or magnitude. When the second principal component is added to the total uncertainty, the PFNS uncertainties in the 1–3-MeV energy range are given

larger uncertainties significantly impacting the k_{eff} uncertainties.

The remaining integral quantities have a much smaller relative change in calculated uncertainties when more principal components are added to the PFNS uncertainty. Both the leakage and the $\mathcal{I}^{(238f)}$ spectral index have slight increases in calculated uncertainties while the $\mathcal{I}^{(239f)}$ and $\mathcal{I}^{(237f)}$ spectral indices have no discernible change. The latter integral quantities show no real difference because they are ratio quantities of the n+^{239}Pu and n+^{237}Np fission reactions to the n+^{235}U fission reaction. When the second principal component is added, the uncertainties in all of these fission reactions increases by nearly the same amount leaving the uncertainties in the ratio quantities the same. In the case of the $\mathcal{I}^{(238f)}$ spectral index, there is very slight amount of uncertainty added below the threshold for the n+^{238}U(n,f) reaction (see Fig. 6.3 below 1 MeV) contributing to the increase of uncertainty in the integral quantity.

Table 6.2 displays the results of propagating the uncertainties in the n+^{235}U PFNS using up to three principal components and assuming the principal components are independent random variables with a uniform distribution, instead of a Gaussian distribution. Once again, the brute force results were computed using 10,000 realizations and the stochastic collocation results were computed using a tensor product quadrature set with 4^K quadrature points. There is good agreement between the relative uncertainties computed using the brute force approach and stochastic collocation method within the Monte Carlo statistics.

The only difference between the relative uncertainty values in Tables 6.1 and 6.2 is the PFNS realizations are sampled from Gaussian and uniform distributions, respectively. In Fig. 6.5 the moments of the PFNS samples from both Gaussian and uniform distributions are in very close agreement. Figure 6.7 shows that while the dominant moments of the input uncertainties remain the same for different distributions and the dominant moments of the output integral distributions remain the same

	Direct Sampling (10^4)			
Integral	MC	Principal Components		
Quantitiy	Statistics*	$K=1$	$K=2$	$K=3$
k_{eff}	0.0001%	0.1042%	0.2337%	0.2335%
Leakage	0.0001%	0.2085%	0.2141%	0.2139%
$\mathcal{I}^{(238f)}$	0.0032%	3.1389%	3.3421%	3.3412%
$\mathcal{I}^{(239f)}$	0.0020%	0.2434%	0.2445%	0.2446%
$\mathcal{I}^{(237f)}$	0.0023%	1.3334%	1.3346%	1.3339%
	Stochastic Collocation Method (4^K)			
Integral	MC	Principal Components		
Quantitiy	Statistics*	$K=1$	$K=2$	$K=3$
k_{eff}	0.0035%	0.0958%	0.2364%	0.2338%
Leakage	0.0027%	0.2128%	0.2132%	0.2132%
$\mathcal{I}^{(238f)}$	0.0860%	3.0370%	3.3403%	3.3826%
$\mathcal{I}^{(239f)}$	0.0533%	0.2280%	0.2458%	0.2465%
$\mathcal{I}^{(237f)}$	0.0616%	1.2835%	1.3350%	1.3526%
* Calculation based on $K=2$ principal components.				

Table 6.2: Lady Godiva relative uncertainties: k_{eff}, total leakage, and $\mathcal{I}^{(238f)}$, $\mathcal{I}^{(237f)}$ and $\mathcal{I}^{(239f)}$ spectral indices assuming an uniform distribution for the principal components. Note that the number of transport solutions for each method are indicated in parentheses.

for different distributions, the distribution shapes propagate through the transport problem in a different manner. While the Gaussian distribution propagates through to the integral values maintaining a Gaussian shape, the uniform distribution propagates through to the integral values having some features of the uniform distribution with some other distinct features. Because the distribution of the PFNS realizations is a linear combination of uniform distributions, this non-uniform input distribution shape propagates through to all of the integral parameter distributions.

To understand the importance of the uncertainties in the integral quantities, the uncertainty in the experimental measurement of k_{eff} is compared with the calculations shown in Tables 6.1 and 6.2. The uncertainty in the experimental benchmark of Lady Godiva for k_{eff} has been reported in the ICSBEP handbook [13] to be 0.1%

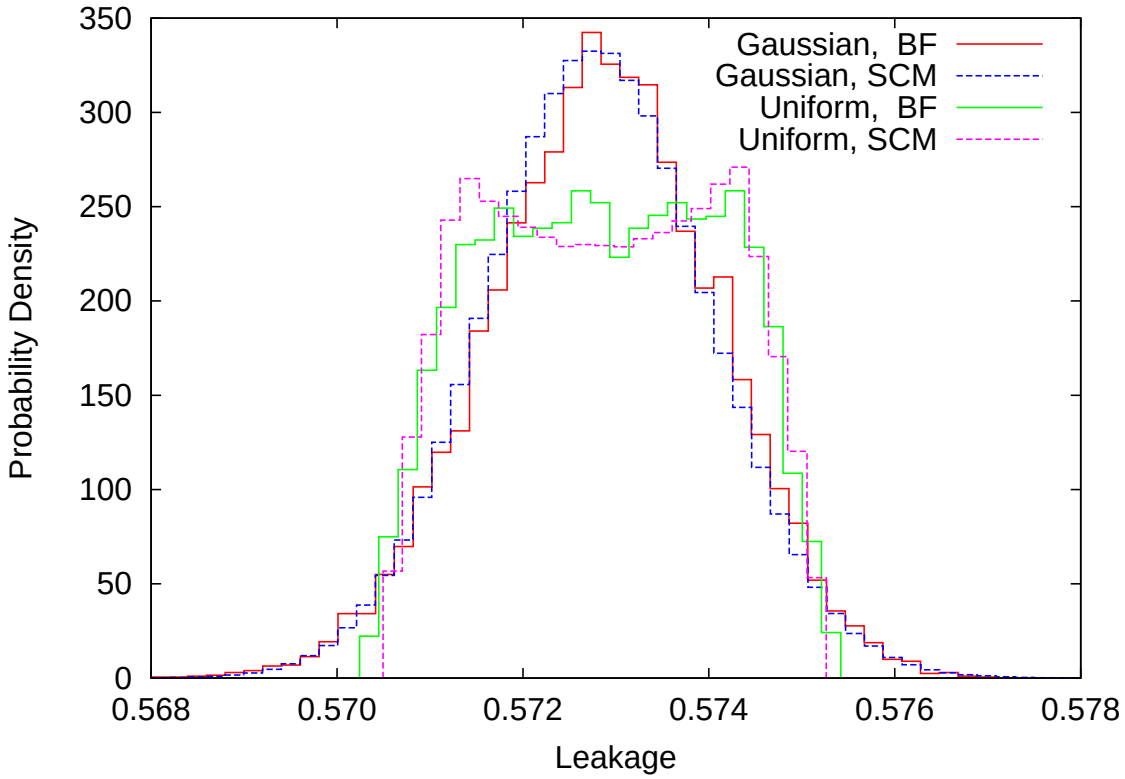

Figure 6.7: The probability density function of the leakage for the Lady Godiva fast critical assembly resulting from propagating the n+^{235}U PFNS uncertainties through MCNP5-1.60. The probability density functions were computed using $K = 2$ principal components with 10,000 PFNS realizations used for the brute force case and 16 PFNS realizations using the Gauss-Hermite and Gauss-Legendre quadrature sets for the Gaussian and uniformly distributed cases, respectively.

compared with the $\approx 0.23\%$ calculated in the present work. Because the PFNS uncertainties lead to larger uncertainties compared with the experimental benchmark, the precise evaluation of the n+^{235}U PFNS is very important and should continue to be studied in both the areas of theoretical modeling and experimental measurements to lower the evaluated uncertainties.

In order to compare the performance between the direct sampling approach and the SCM uncertainty propagation methods the minimum number of brute force trans-

port calculations to minimize the statistical noise can be estimated. Assuming that with 10,000 PFNS realizations the relative uncertainties in Tables 6.1 and 6.2 have converged and assuming that the $K = 2$ principal components adequately capture the PFNS uncertainties, the difference in the relative uncertainty of the SCM and direct sampling method is computed. Table 6.3 shows the estimated number of Monte

	Gaussian			Uniform		
Integral		Transport Solves			Transport Solves	
Quantitiy	Error	SCM	BF	Error	SCM	BF
k_{eff}	1.68%	16	1,240	1.16%	16	5,560
Leakage	1.86%	16	1,105	*0.42%	16	2,330
$\mathcal{I}^{(238f)}$	1.36%	16	5,745	*0.05%	16	2,795
$\mathcal{I}^{(239f)}$	2.72%	16	1,555	*0.53%	16	1,790
$\mathcal{I}^{(237f)}$	2.13%	16	1,545	*0.03%	16	1,790
* Minimum of 1.00% is used in estimation of BF transport solves.						

Table 6.3: Lady Godiva: Convergence of k_{eff}, total leakage, and $\mathcal{I}^{(238f)}$, $\mathcal{I}^{(237f)}$ and $\mathcal{I}^{(239f)}$ spectral indices. The errors computed are the relative difference between the direct sampling and the SCM relative uncertainties with the number of brute force transport calculations being the last realization outside of the 1-σ error band.

Carlo transport calculations necessary to be as accurate as the SCM calculated uncertainties for each of the integral quantities. The accuracy measure is established by computing the relative difference between the direct sampling relative uncertainties and the SCM relative uncertainties. In some cases the integral quantity relative uncertainties computed using SCM are in extremely good agreement with the direct sampling relative uncertainties causing the estimated minimum number of brute force transport calculations to be prohibitively large. Therefore, the error bands are increased to a minimum of 1.00%, resulting in a more reasonable estimation of the minimum number of brute force transport calculations. Note that the majority of the computation time needed to propagate the uncertainties through the critical assemblies is spent on solving each transport problem therefore the number of PFNS realizations used in each calculation is an appropriate measure of the compu-

tational cost. While propagating the n+^{235}U PFNS uncertainties through the Lady Godiva critical assembly the SCM results computationally cost between 1–2 orders of magnitude less compared to the direct sampling approach.

6.1.4 Jezebel Critical Assembly

The Jezebel fast critical assembly [16] is a metallic, spherical assembly with an approximate radius of 6.3849 cm composed mostly of ^{239}Pu with smaller amounts of ^{240}Pu and ^{241}Pu. The n+^{239}Pu PFNS uncertainties are propagated through the Jezebel critical assembly. From Fig. 6.3 the necessary number of principal components needed to adequately propagate the modeled uncertainties is estimated to be $K = 3$.

Table 6.1 shows the results of propagating the uncertainties in the n+^{239}Pu PFNS using up to three principal components and assuming the principal components are independent random variables with a Gaussian distribution. Once again the direct sampling results were obtained by computing 10,000 realizations of the PFNS where the stochastic collocation method results were obtained using the Gauss-Hermite quadrature with 8^K quadrature points. The resulting relative uncertainties from the SCM method are in extremely good agreement with the direct sampling results demonstrating the convergence capability of the SCM method with a larger quadrature set. With a higher quadrature order, the Monte Carlo statistics for the SCM relative standard deviations in Tables 6.4 and 6.5 are smaller in comparison to the statistics in Tables 6.1 and 6.2, leading to smaller errors with respect to the direct sampling results.

Once again, the uncertainties in the k_{eff} integral quantity increases the most from the addition of the remaining principal components which contribute more to the PFNS uncertainties in the 0.5–5-MeV outgoing neutron energy range. Com-

Integral Quantitiy	Direct Sampling (10^4) MC Statistics*	Principal Components $K=1$	$K=2$	$K=3$
k_{eff}	0.0001%	0.1063%	0.1576%	0.1634%
Leakage	0.0001%	0.0184%	0.0198%	0.0208%
$\mathcal{I}^{(238f)}$	0.0026%	1.1406%	1.6976%	1.7110%
$\mathcal{I}^{(239f)}$	0.0018%	0.1670%	0.1675%	0.1681%
$\mathcal{I}^{(237f)}$	0.0021%	0.7530%	0.7833%	0.7838%
Integral Quantitiy	Stochastic Collocation Method (8^K) MC Statistics*	Principal Components $K=1$	$K=2$	$K=3$
k_{eff}	0.0021%	0.1108%	0.1531%	0.1623%
Leakage	0.0017%	0.0170%	0.0215%	0.0201%
$\mathcal{I}^{(238f)}$	0.0445%	1.2171%	1.6331%	1.6908%
$\mathcal{I}^{(239f)}$	0.0311%	0.1660%	0.1666%	0.1688%
$\mathcal{I}^{(237f)}$	0.0349%	0.7682%	0.7662%	0.7862%

* Calculation based on $K = 3$ principal components.

Table 6.4: Jezebel relative uncertainties: k_{eff}, total leakage, and $\mathcal{I}^{(238f)}$, $\mathcal{I}^{(237f)}$ and $\mathcal{I}^{(239f)}$ spectral indices assuming a Gaussian distribution for the principal components. Note that the number of transport solutions for each method are indicated in parentheses.

pared with the analysis done for the Lady Godiva integral quantity uncertainties, the remaining integral quantities have a larger relative change in calculated uncertainties when more principal components are added to the PFNS uncertainty. This is attributed to the magnitude and outgoing energy range of the remaining principal components for the n+^{239}Pu PFNS compared with the n+^{235}U PFNS. In particular, the $\mathcal{I}^{(238f)}$ spectral index in the Jezebel assembly has a larger increase in calculated uncertainties compared to Lady Godiva because the second principal component in Fig. 6.3 ranges to a lower outgoing neutron energy, farther below the fission threshold than the second principal component of the n+^{235}U PFNS. Similarly, the $\mathcal{I}^{(237f)}$ spectral index shows a small but definite change with the addition of the second principal component because the uncertainties are increased below the $\approx$ 0.7-MeV

n+^{237}Np(n,f) reaction threshold contributing to the increase of uncertainty in the integral quantity.

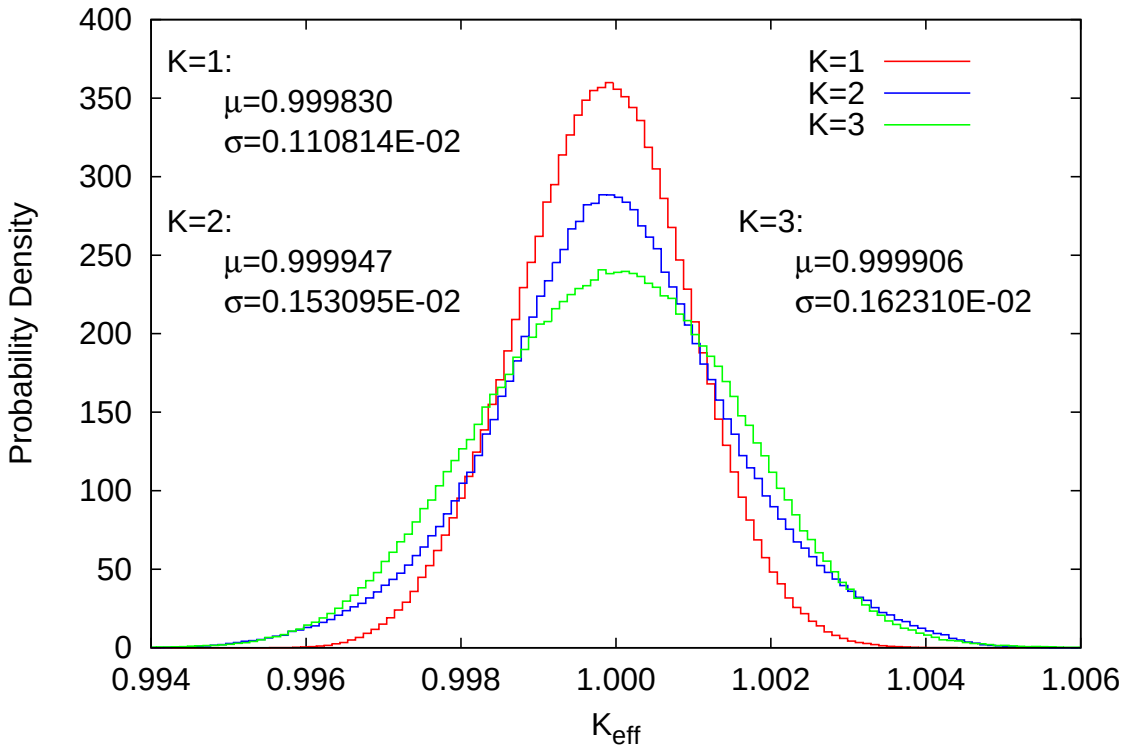

Figure 6.8: The probability density function of the effective multiplication factor, k_{eff}, for the Jezebel fast critical assembly resulting from propagating the n+^{239}Pu PFNS uncertainties through MCNP5-1.60 with a Gauss-Hermite quadrature set of order 8 with 8^K tensor product quadrature points.

The probability density function of the k_{eff} integral value resulting from the propagation of the Gaussian distributed n+^{239}Pu PFNS uncertainties can be seen in Fig. 6.8. As expected from the qualitative analysis of the PCA (see Fig. 6.3) three principal components are needed in order to adequately propagate the uncertainties in the PFNS. Along with the plotted probability density functions, all of the mean and standard deviation values are listed in Fig. 6.8.

	Direct Sampling (10^4)			
Integral	MC	Principal Components		
Quantitiy	Statistics*	$K=1$	$K=2$	$K=3$
k_{eff}	0.0001%	0.1069%	0.1563%	0.1621%
Leakage	0.0001%	0.0183%	0.0199%	0.0207%
$\mathcal{I}^{(238f)}$	0.0026%	1.1424%	1.6902%	1.6978%
$\mathcal{I}^{(239f)}$	0.0018%	0.1671%	0.1678%	0.1687%
$\mathcal{I}^{(237f)}$	0.0021%	0.7542%	0.7827%	0.7826%
	Stochastic Collocation Method (8^K)			
Integral	MC	Principal Components		
Quantitiy	Statistics*	$K=1$	$K=2$	$K=3$
k_{eff}	0.0007%	0.1041%	0.1584%	0.1611%
Leakage	0.0006%	0.0180%	0.0189%	0.0198%
$\mathcal{I}^{(238f)}$	0.0145%	1.1936%	1.7023%	1.7034%
$\mathcal{I}^{(239f)}$	0.0101%	0.1606%	0.1707%	0.1693%
$\mathcal{I}^{(237f)}$	0.0114%	0.7513%	0.7922%	0.7847%
* Calculation based on $K=3$ principal components.				

Table 6.5: Jezebel relative uncertainties: k_{eff}, total leakage, and $\mathcal{I}^{(238f)}$, $\mathcal{I}^{(237f)}$ and $\mathcal{I}^{(239f)}$ spectral indices assuming an uniform distribution for the principal components. Note that the number of transport solutions for each method are indicated in parentheses.

Table 6.5 displays the results of propagating the uncertainties in the n+^{235}U PFNS using up to three principal components and assuming the principal components are independent random variables with a uniform distribution. Once again, the direct sampling results were computed using 10,000 realizations and the stochastic collocation results were computed using a tensor product quadrature set with 8^K quadrature points. There is good agreement between the relative uncertainties computed using the direct sampling approach and SCM within the Monte Carlo statistics.

The probability density functions of the spectral indices are plotted in Fig. 6.9 utilizing all 3 principal components in the n+^{239}Pu PFNS uncertainty. Both the uniform and Gaussian PCE spectral index coefficients have been computed using

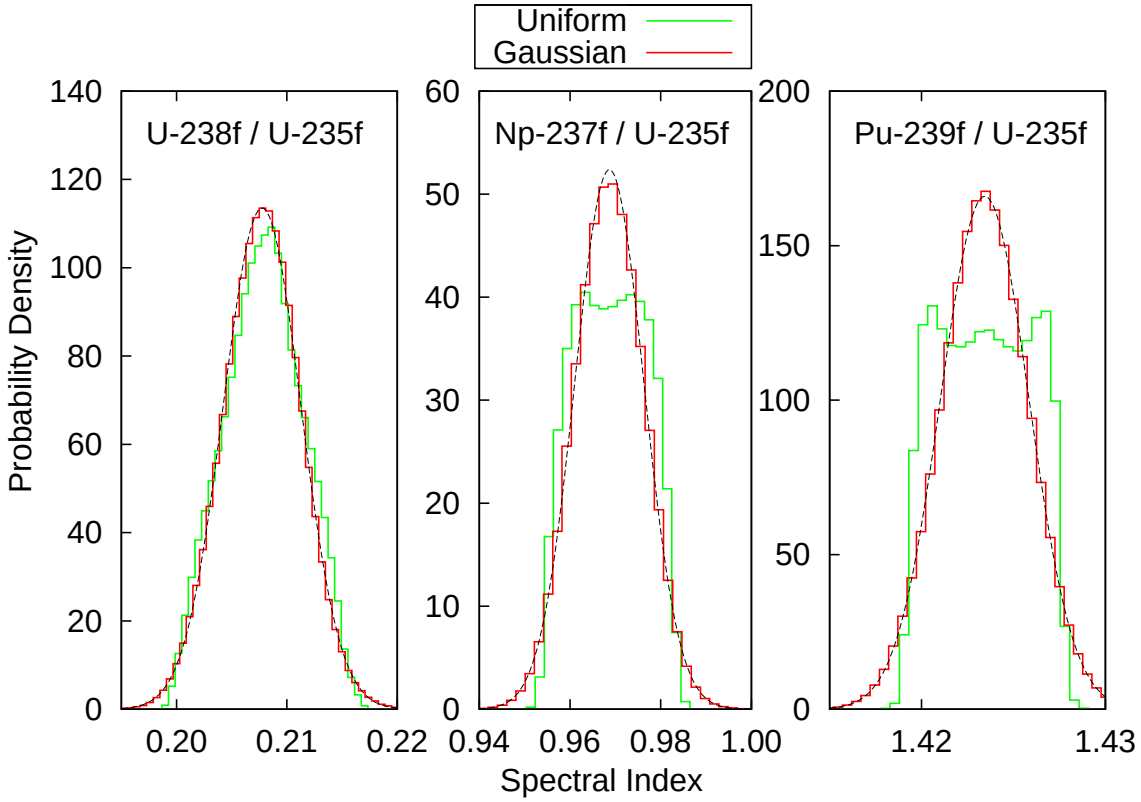

Figure 6.9: The probability density function of the spectral indices for the Jezebel fast critical assembly resulting from propagating the n+^{239}Pu PFNS uncertainties through MCNP5-1.60 with a Gauss quadrature set of order 8 with 8^K tensor product quadrature points. Note the continuous dashed line represents a Gaussian distribution based on the computed SCM moments.

the Gauss-Legendre and Gauss-Hermite quadrature sets, respectively, for the inner products of the angular flux coefficients computed in Eq. (5.25). The uniform and Gaussian probability density functions were then reconstructed, as in Eq. (5.19), from the spectral index coefficients and the underlying orthogonal polynomials. Compared with the computational cost to run MCNP5-1.60 for each realization of the PFNS, the PCE method is very inexpensive to reconstruct the PDF of the integral quantities from the calculated coefficients.

As we mentioned previously, the number of principal components used to model

the n+^{239}Pu PFNS uncertainties was found to be very important for the $\mathcal{I}^{(238f)}$ spectral index uncertainty, less important for the $\mathcal{I}^{(237f)}$ spectral index uncertainty and generally unimportant for the $\mathcal{I}^{(239f)}$ spectral index uncertainty. Figure 6.9 demonstrates the effect on the integral quantity uncertainty when using independent uniform distributions for the principal components. In a situation where many principal components with nearby eigenvalues are needed to construct realizations of the PFNS, the linear combination of independent uniform distributions in Eq. (5.10) would lead to an overall distribution that would be similar to a Gaussian distribution. In this case, because each of the 3 principal components are very important in the calculation of the $\mathcal{I}^{(238f)}$ spectral index uncertainty, the distribution begins to look similar to a Gaussian distribution while the distribution for the $\mathcal{I}^{(239f)}$ spectral index has a definite uniform shape coming from the dominance of the single most important principal component.

With a quadrature set of order 8 chosen to compute the PCE coefficients, a polynomial order $P = 7$ is used to reconstruct each probability density function seen in both Figs. 6.8 and 6.9. Allowing a higher order polynomial expansion, the skewness of the distributions can be observed if the higher order PCE coefficients are large enough. Skewness of the probability density function would be the result of some nonlinear effects being present while propagating the uncertainties through the transport equation. It is clear in both Figs. 6.8 and 6.9 that the higher order coefficients are very small and if there is any discernible skewness in the distributions it would be difficult to determine whether the skewness is present because of nonlinear effects or if the skewness is due to the statistical noise in the MCNP5-1.60 calculations.

To understand the importance of the uncertainties in the integral quantities, the uncertainty in the experimental benchmark of Jezebel for k_{eff} is compared with the calculations shown in Tables 6.4 and 6.5. The uncertainty in k_{eff} in the experimental benchmark has been reported in the ICSBEP handbook [13] to be 0.2% compared

with the $\approx 0.16\%$ calculated in the present work. Because the PFNS uncertainties lead to uncertainties of the same order compared with experimental measurements, the precise evaluation of the n+^{239}Pu PFNS is very important and should continue to be studied in both the areas of theoretical modeling and experimental measurements to better understand and possibly lower the evaluated uncertainties.

	Gaussian			Uniform		
Integral		Transport Solves			Transport Solves	
Quantitiy	Error	SCM	BF	Error	SCM	BF
k_{eff}	*0.67%	512	6,275	*0.62%	512	5,575
Leakage	3.33%	512	2,245	4.14%	512	135
$\mathcal{I}^{(238f)}$	1.18%	512	5,855	*0.33%	512	4,935
$\mathcal{I}^{(239f)}$	*0.42%	512	7,015	*0.36%	512	2,365
$\mathcal{I}^{(237f)}$	*0.31%	512	7,020	*0.27%	512	2,365
* Minimum of 1.00% is used in estimation of BF transport solves.						

Table 6.6: Jezebel: Convergence of k_{eff}, total leakage, and $\mathcal{I}^{(238f)}$, $\mathcal{I}^{(237f)}$ and $\mathcal{I}^{(239f)}$ spectral indices. The errors computed are the relative difference between the brute force and the SCM relative uncertainties with the number of brute force transport calculations being the last realization outside of the 1-σ error band.

Table 6.6 shows the approximate number of brute force transport calculations necessary to converge within 1-σ of the final converged integral quantity. Once again the error bands are established by computing the relative difference between the brute force relative uncertainties and the SCM relative uncertainties. Because the quadrature order is chosen to be larger than the one chosen for the Godiva problem, some of the integral quantity relative uncertainties computed using SCM are well converged, leading to small errors with respect to the direct sampling results. Therefore, the error bands are set at a minimum of 1.00% around the brute force converged relative standard deviations, resulting in a more reasonable estimation of the minimum number of brute force transport calculations. While propagating the n+^{239}Pu PFNS uncertainties through the Jezebel critical assembly, to obtain a reasonable estimation of the relative uncertainties in the integral parameters, the

SCM results computationally cost an order of magnitude less compared to the direct sampling approach. However, if the only information wanted from the uncertainty propagation is an estimate of the relative uncertainty in the integral parameters, a quadrature set of order 2 can be used resulting in only 8 transport solves for the SCM method. For the Gaussian case, for example, the relative uncertainty in k_{eff} is calculated to be 0.1556% with a quadrature set of order 2, which is less than a 5% error with respect to the converged brute force results. This approach would certainty lead to a reasonable estimate of the integral parameter uncertainties with nearly 3 orders of magnitude computational savings.

6.1.5 Summary

We have successfully used the recently released n+^{235}U and n+^{239}Pu PFNS covariance matrices from the ENDF/B-VII.1 data library and performed principal component analysis on the matrices to study the uncertainties present in the PFNS. The number of principal components needed to propagate uncertainties through any neutron transport application was found to be a maximum of $K = 2$ and $K = 3$ for the n+^{235}U and n+^{239}Pu PFNS covariance matrices, respectively. Each of the studied integral parameters behaved slightly differently depending on the number of principal components:

- For both the Lady Godiva and Jezebel critical assemblies, the k_{eff} and the $\mathcal{I}^{(238f)}$ spectral index integral quantities need the maximum number of principal components to accurately predict the correct propagated uncertainty. If too few principal components are used in propagating the uncertainty, the integral quantity uncertainties could be underestimated.
- In the Lady Godiva critical assembly, the relative uncertainties computed for the leakage and the $\mathcal{I}^{(237f)}$ and $\mathcal{I}^{(239f)}$ spectral indices changed very little when

more principal components were added. This is due to the bulk of the uncertainties in each of these integral parameters coming from the lower energy part of the spectrum. Figure 6.3 shows that with just a single principal component, the lower outgoing energy uncertainties in the PFNS are accurately modeled.

- For the Jezebel critical assembly, in order to accurately calculate the relative uncertainties for the leakage and the $\mathcal{I}^{(237f)}$ and $\mathcal{I}^{(239f)}$ spectral indices, the maximum number of principal components need to be used. This is in contrast to the integral parameters calculated for the Lady Godiva critical assembly. This is due to the higher energy spectrum (see Fig. 6.1) observed in the Jezebel assembly effectively shifting where the most sensitive region of the PFNS is located.

For both n+^{235}U and n+^{239}Pu PFNS in the Lady Godiva and Jezebel critical assemblies, respectively, a standard direct sampling approach was implemented along with the stochastic collocation method to propagate the uncertainties to the integral quantities. The direct sampling approach was implemented using 10,000 PFNS realizations. Because of the simplicity of the critical assemblies, it is computationally feasible to perform so many brute force realizations. However, if it is necessary to propagate the PFNS uncertainties through a much more computationally expensive transport problem (i.e. full-core critical reactor physics calculation) then the brute force approach would be prohibitively expensive. In comparing the brute force approach and the polynomial chaos expansion with the stochastic collocation method (PCE-SCM), the general result was that the brute force approach would computationally cost between 1–2 orders of magnitude more than the SCM approach just to calculate the relative standard deviation of the integral quantities. If we are interested in obtaining the probability density function for the integral quantities, the noise in the histogram may be too large to discern any nonlinear effects if the number of brute force calculations is decreased. On the other hand, the PCE-SCM approach

offers a computationally inexpensive approach to computing the probability density functions in a high fidelity histogram allowing any nonlinear effects to be seen clearly. Also, if all that is wanted is a reliable estimate of the relative uncertainty in the integral quantities, the PCE-SCM approach can be used with a very small quadrature order of 2 leading to only 2^K transport solves using the tensor product quadrature set.

The polynomial chaos expansion with the stochastic collocation method is used to calculate uncertainties of several important integral quantities in the Lady Godiva and Jezebel critical assemblies. The computed uncertainties in k_{eff} for both the Lady Godiva and Jezebel assemblies are shown to be of the same order or larger compared with the experimental benchmark uncertainties in the ICSBEP handbook [13] meaning the PFNS uncertainties have a significant impact on these applications and should be studied more to decrease the evaluated uncertainties. In general, the PCE-SCM results compare nicely with the direct sampling results and offer a significant improvement on computational cost while maintaining flexibility in propagating uncertainties with different distribution shapes and magnitudes. This work has shown that it is possible to propagate realistic nuclear data uncertainties through critical transport problems using the PCA dimension reduction technique along with applying the PCE-SCM method, and still obtain statistically significant results while dramatically reducing the computational cost.

6.2 Actinide Suite Uncertainty Propagation

One of the novel aspects of the present work is the availability of cross-isotope correlations in the PFNS uncertainties resulting from the actinide suite evaluations presented in Chapter 4.1. Never before have cross-isotope correlations been taken into account in either of the uncertainty quantification evaluation process or the un-

certainty propagation through critical assemblies. These cross-isotope correlations are included in the following sections where the PFNS uncertainties in the uranium and plutonium actinide suites are propagated through the Big Ten and Flattop assemblies. Unlike in Chapter 6.1 where the PFNS covariance matrices are taken from the ENDF/B-VII.1 nuclear data library [1] and used to obtain realizations, the model parameter covariance matrices along with LA model calculations are used in the following sections to obtain realizations of the PFNS. This approach avoids the linear assumptions made in the final calculation of the PFNS covariance matrices allowing LA model nonlinearities to persist through the uncertainty propagation calculations.

Sampling from the model parameters leads to a substantial difference in the input PFNS uncertainties and correlations compared to sampling directly from the PFNS covariance matrix seen in Chapter 6.1. In the following sections presenting numerical results from the propagation of uncertainties, the model parameters are sampled using a PCA on the model parameter covariance matrix and the brute force direct sampling method assuming a Gaussian distribution for each of the principal components. Compared with the Lady Godiva and Jezebel assemblies, the Big Ten and Flattop assemblies take substantially longer to calculate the integral quantities using MCNP5-1.60. For example, the Lady Godiva and Jezebel assembly calculations each take on the order of a half hour computational time while the Big Ten assembly takes between 8-9 hours using the same 4 threaded processors. Therefore, instead of running 10,000 brute force realizations of the PFNS through the assemblies, the Big Ten and Flattop results are obtained using 1,000 realizations.

In Figs. 6.10 and 6.11 the relative uncertainty and correlation matrix, respectively, of the PFNS for the n(0.5 MeV)+^{235}U fission reaction found in the actinide suite evaluation in Chapter 4.1 are compared with the PFNS sampled statistics resulting from each of the model parameter realizations passing through the LA model calculation. The differences between the expected input uncertainties and correla-

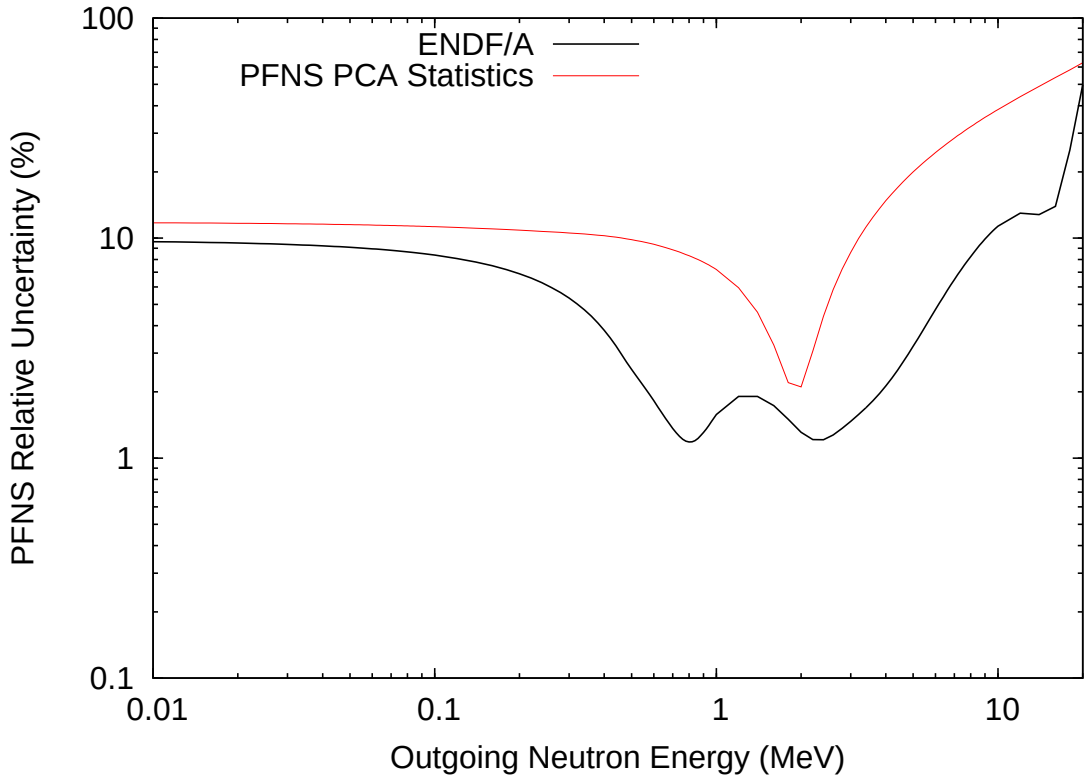

Figure 6.10: The relative uncertainty of the PFNS for the n(0.5 MeV)+^{235}U fission reaction obtained from the actinide suite evaluation in Chapter 4.1 compared with the sampled statistics coming from the model parameters.

tions and the actual input quantities are mainly due to the rigidity of the LA model causing the shape of the sampled statistics to be fixed and the nonlinearities in the LA model causing the magnitude of the uncertainties to be increased. The sampled model parameter statistics behave very well compared with the results of the actinide suite evaluation in Tables 4.2 and 4.3 even with the significant differences in the PFNS statistics. In order to include the cross-isotope correlations the sampling is chosen to come from the model parameters for simplicity and efficiency.

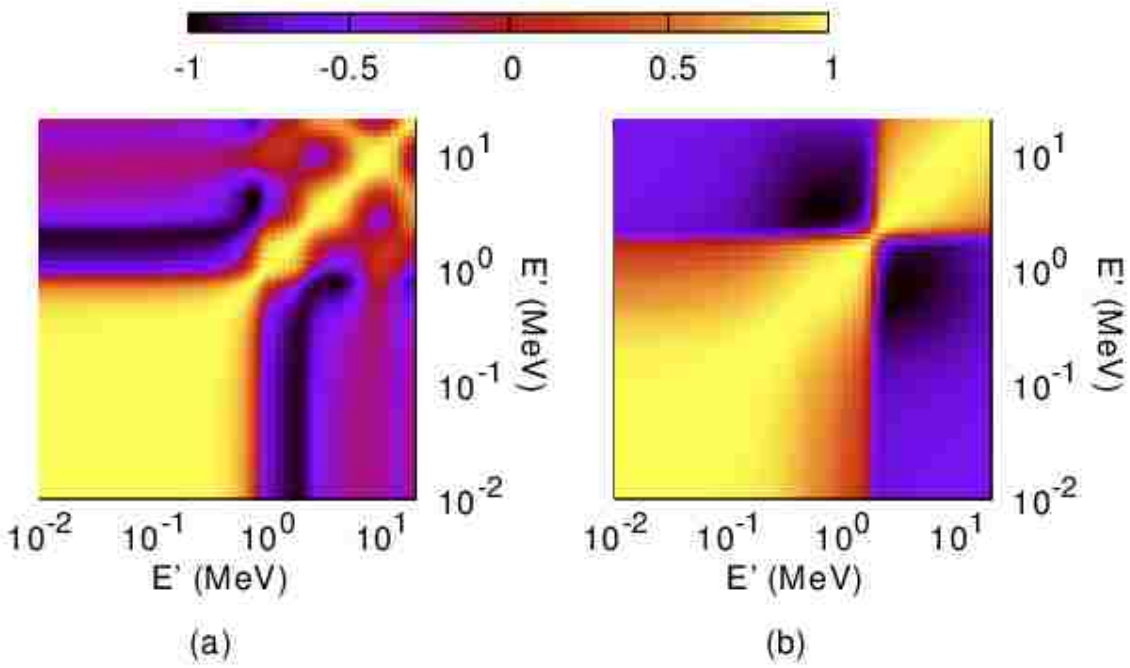

Figure 6.11: The correlation matrix of the PFNS for the n(0.5 MeV)+^{235}U fission reaction obtained from (a) the actinide suite evaluation in Chapter 4.1 compared with (b) the sampled statistics coming from the model parameters.

6.2.1 Impact of Cross-isotope Correlations

Along with the uncertainty quantification work presented in Chapter 4.1, the evaluation process led to a new evaluation of the mean values of the PFNS for each of the uranium and plutonium suites of actinides. Before propagating the uncertainties, the mean values of the newly evaluated PFNS are used to obtain the integral quantities in the Big Ten assembly and compared against the most recent releases of the U.S. nuclear data libraries [63, 1] and experimental measurements where available.

In Table 6.7 the calculated integral quantities of the Big Ten assembly show only a few small differences between the U.S. nuclear data libraries and the present evaluation work. Each of the spectral indices are all within the Monte Carlo statistical

Integral Parameter	Data Library		Present Work	Experimental Benchmark*
	ENDF/B-VII.0	ENDF/B-VII.1		
k_{eff}	0.99496(7)	0.99460(7)	0.99243(7)	0.9948(13)
$\mathcal{I}^{(238f)}$	0.0353(6)	0.0358(7)	0.0353(6)	0.03739(34)
$\mathcal{I}^{(237f)}$	0.312(2)	0.313(3)	0.311(2)	0.3223(30)
$\mathcal{I}^{(239f)}$	1.163(5)	1.162(5)	1.163(5)	1.1936(84)
*Taken From ICSBEP Handbook [13]				

Table 6.7: Big Ten critical assembly integral quantities calculated using the ENDF/B-VII libraries compared with the present evaluation work and the experimentally measured values.

uncertainties while the effective multiplication factor shows the most differences between each of the libraries. The ENDF/B-VII.0 and ENDF/B-VII.1 k_{eff} results are reasonably close to each other, within the 99% confidence interval for each calculation, while the present work is about 0.2% below that of the ENDF/B-VII.1 calculation. The lower effective multiplication factor can be attributed to the increased low outgoing-energy tail on the newly evaluated PFNS taking away from some of the neutrons emitted from the peak of the distribution in the 1–3-MeV range. Even though the Big Ten assembly is considered to be in the fast energy range, the neutrons with lower energy that induce fission generally lead to a smaller number of subsequent fission neutrons being emitted compared with high incident energy fission events. This effect on the multiplication factor is noticeable and is the reason for the lowered effective multiplication factor.

In comparison to the benchmarked experimental measurements, the spectral indices from all of the data libraries including the present work are all low and outside of the experimental uncertainties. This is attributed to the quality of the entire data library being used and not just the PFNS evaluations. The cross sections, angular distributions and other fission quantities, such as the average number of neutrons released in a fission event, may need to be re-evaluated in order to adequately compare the calculations to the measurements. The effective multiplication factors calculated

using MCNP5-1.60 with each of the ENDF/B-VII data libraries in Table 6.7 are in very good agreement with the experimental k_{eff} benchmark while the newly evaluated PFNS data library is about 0.2% below the experimental uncertainties. Once again, this difference is the result of the impact that the increased low outgoing energy tail in the PFNS has on the effective multiplication factor.

In an effort to understand the impact that the cross-isotope correlations have on the uncertainties in the effective multiplication factor and the ^{238}U, ^{237}Np and ^{239}Pu fission reaction spectral indices (see Eqs. (2.5)–(2.7)), the uncertainties in the PFNS for the uranium suite of actinides are propagated through the Big Ten assembly. Compared with the fast-critical systems like Godiva, Jezebel and the Flattop assemblies, the Big Ten assembly is considered to be in the fast energy range even with the intermediate enrichment of the uranium material. With a more balanced material composition in the Big Ten assembly, the cross-isotope correlations should have a larger impact compared with the other fast critical assemblies where the majority of fissioning events occur in the ^{235}U or ^{239}Pu isotopes depending on the primary material in each assembly.

In the uncertainty propagation work presented in Chapter 6.1 the covariance matrices for the PFNS reactions were treated independently and uncorrelated. In the same sense, Fig. 6.12 shows the overall PFNS correlations if the uranium isotopes present in the Big Ten assembly were assumed to be fully uncorrelated. All of the off-diagonal elements between uranium isotopes are set to zero guaranteeing that the uncertainties in the PFNS are uncorrelated. In this case, the PFNS for each of the uranium isotopes can be sampled independently requiring the individually quantified uncertainties to be subsequently combined to determine the total uncertainties by,

$$\tilde{\sigma}_{total} = \sqrt{\sum_{i=1}^{I} \tilde{\sigma}_i^2}\,, \tag{6.4}$$

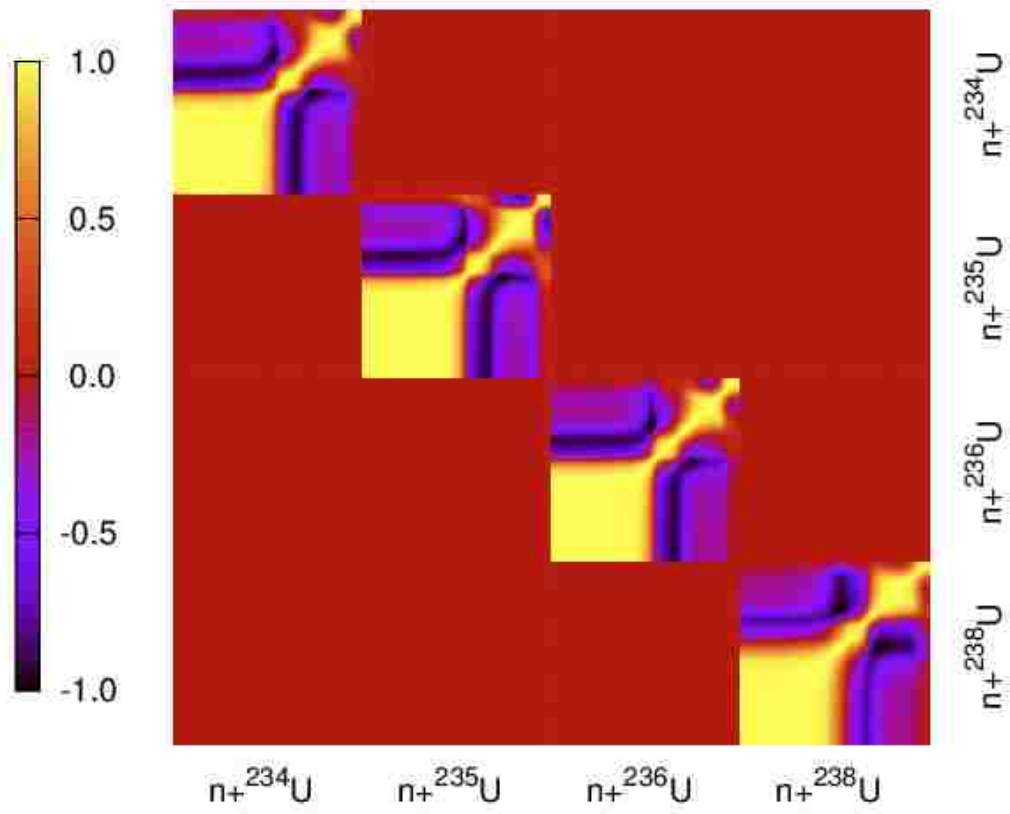

Figure 6.12: The correlation matrix excluding cross-isotope correlations of the PFNS for the n(0.5 MeV)+^{234,235,236,238}U fission reactions resulting from the actinide suite evaluation in Chapter 4.1.

where $\tilde{\sigma}_i$ is the relative uncertainty from source i.

Using the posterior model parameter correlations in Table 4.3 and Eq. (3.22), the cross-correlations between the uranium isotopes are computed. Figure 6.13 shows the PFNS correlations for the uranium isotopes present in the Big Ten assembly. Comparing the correlations in the Figs. 6.12 and 6.13, the cross-isotope correlations are significant which lead to differences in the quantified uncertainties.

In Table 6.8 the Monte Carlo statistics in the second column refer to a sample calculation for each of the integral quantities. When the statistics of the integral

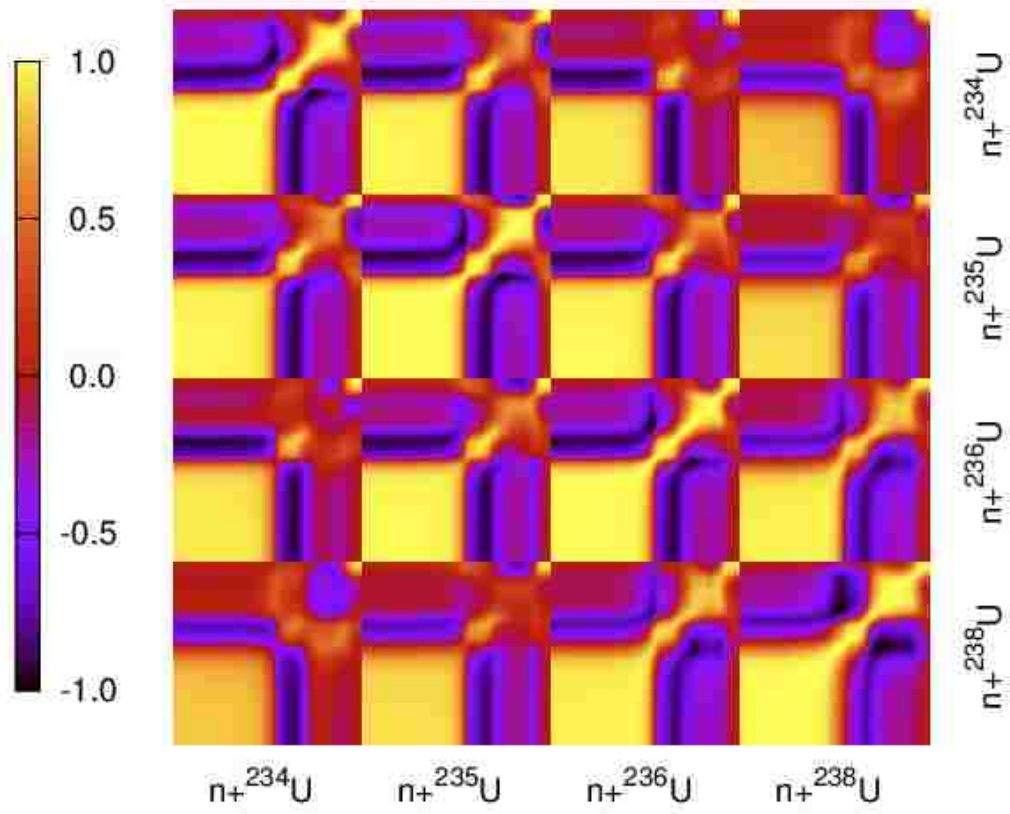

Figure 6.13: The correlation matrix including cross-isotope correlations of the PFNS for the n(0.5 MeV)+^{234,235,236,238}U fission reactions resulting from the actinide suite evaluation in Chapter 4.1.

quantities calculated using the MCNP5-1.60 tool for each realization of the PFNS are the same magnitude or larger than the uncertainties calculated coming from the PFNS uncertainties, then the uncertainties calculated should not be fully trusted because the Monte Carlo statistics could be influencing the results. All of the uncertainties calculated for the $\mathcal{I}^{(239f)}$ spectral index in Table 6.8 are small compared with not only the experimental measurement precision (0.70%) but also to the Monte Carlo statistics. Therefore, the $\mathcal{I}^{(239f)}$ spectral index uncertainty is not considered to be heavily influenced by the PFNS uncertainties and not discussed any further.

The remaining integral quantities in Table 6.8 including the k_{eff}, and the $\mathcal{I}^{(238f)}$

Integral Parameter	Monte Carlo Statistics (%)	Uncertainty (%)					
		Uncorrelated					Correlated
		^{234}U	^{235}U	^{236}U	^{238}U	Total	Total
k_{eff}	0.010	0.010	1.437	0.009	0.430	1.500	1.818
$\mathcal{I}^{(238f)}$	2.000	1.557	6.707	1.525	2.359	7.436	8.303
$\mathcal{I}^{(237f)}$	0.300	0.543	1.644	0.546	0.703	1.947	1.974
$\mathcal{I}^{(239f)}$	0.400	0.086	0.160	0.075	0.085	0.214	0.190

Table 6.8: Big Ten critical assembly quantified uncertainties due to the uranium suite PFNS uncertainties. The effect of the cross-isotope correlations can be seen in the differences between the total uncertainties in the uncorrelated and correlated results.

and $\mathcal{I}^{(237f)}$ spectral indices each have calculated uncertainties that are large compared to both the experimental measurement uncertainties ($\sim 0.13\%$ for k_{eff}) and the Monte Carlo precision to which they were calculated. Not only are the calculated uncertainties large, but there are significant differences between the correlated and uncorrelated total uncertainties. For example, the uncorrelated total uncertainties in k_{eff} and $\mathcal{I}^{(238f)}$ are under-predicted by about 17.5% and 10.4%, respectively, compared with the correlated total uncertainty calculated. Because this is not an insignificant amount of under-prediction, the correlations between the uranium isotopes in the PFNS uncertainties can have a large impact on the uncertainties quantified for this specific application.

In Figs. 6.14 and 6.15 the probability density function (PDF) is shown for the k_{eff} and $\mathcal{I}^{(238f)}$ integral parameters, respectively. Because the uncertainties of the PFNS for the ^{234}U and ^{236}U fission reactions are calculated to be very small and generally negligible, only the correlated PFNS and the uncorrelated PFNS for the ^{235}U and ^{238}U fission reaction PDFs are shown. In both Figs. 6.14 and 6.15, the correlated PDF shows a slightly wider distribution with a shorter peak compared to the uncorrelated PDFs and that is the result of the under-prediction of the uncorrelated uncertainty propagation. Even though the Big Ten assembly is composed on

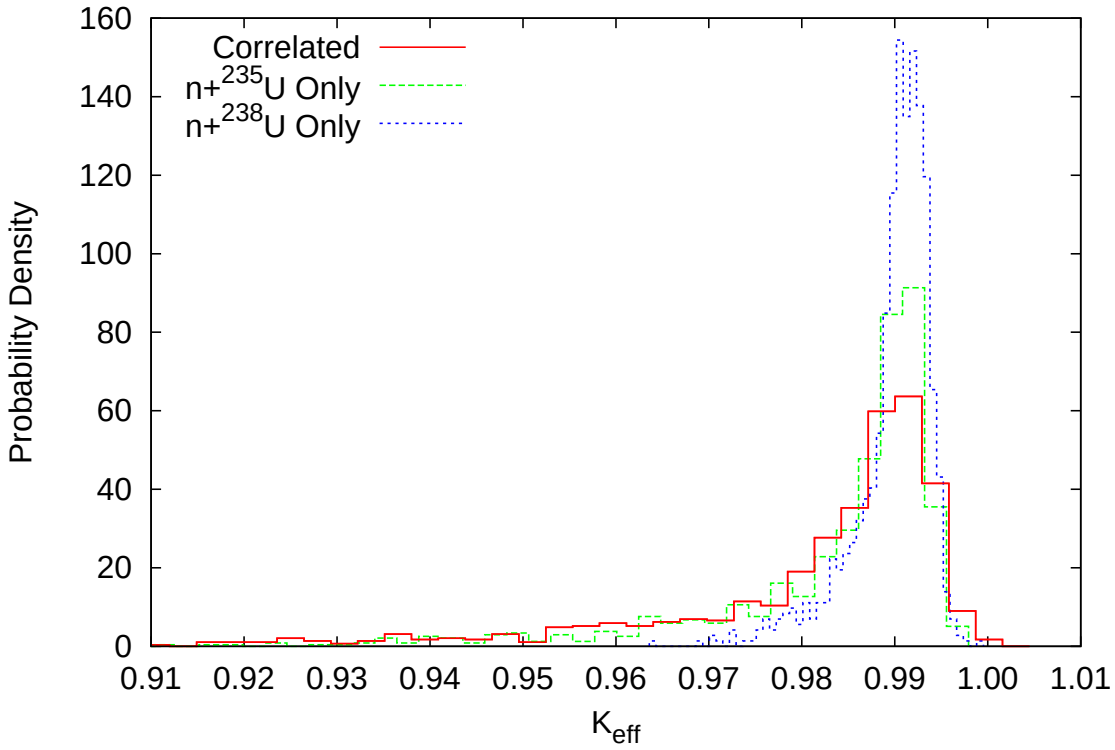

Figure 6.14: The probability density of the effective multiplication factor, k_{eff}, resulting from propagating the uranium suite PFNS uncertainties through the Big Ten assembly.

average of only 10% ^{235}U, the majority of the uncertainties come from the ^{235}U PFNS uncertainties because the fission cross section of ^{235}U still dominates the fission cross section of the remaining uranium isotopes present partly because of the ^{238}U(n,f) reaction threshold. Both of these integral quantities were calculated to have roughly the same relative uncertainty due to the uncertainties in the correlated PFNS nuclear data with some obvious non-Gaussian features leading to a long tail on the low side of the k_{eff} and $\mathcal{I}^{(238f)}$ spectral index.

In conclusion, the PFNS uncertainties can and do lead to large uncertainties in some of the integral quantities compared to the experimental measurement uncer-

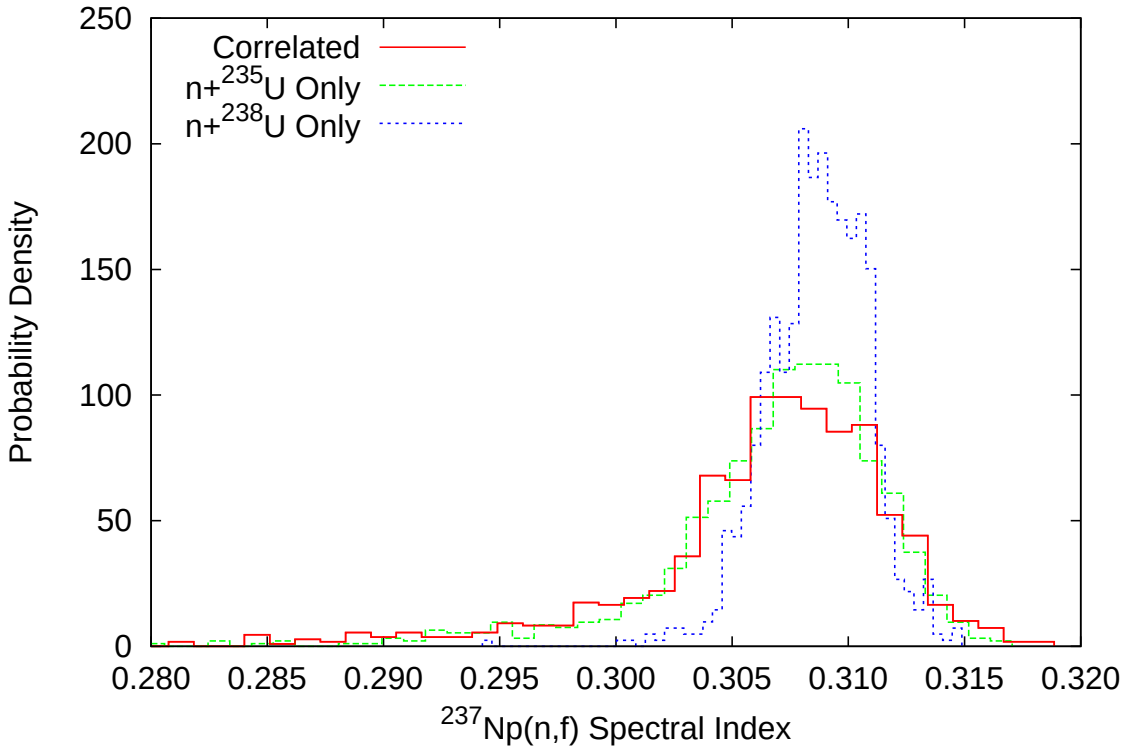

Figure 6.15: The probability density of the ^{237}Np(n,f) reaction spectral index resulting from propagating the uranium suite PFNS uncertainties through the Big Ten assembly.

tainties. And probably a more important result, the cross-isotope correlations found in the uncertainty quantification of the actinides in Chapter 4.1 lead to significant differences in propagated uncertainties in the Big Ten assembly.

6.2.2 Unified Monte Carlo and Total Monte Carlo Method

With a new evaluation of the PFNS for each of the uranium and plutonium actinides presented in Chapter 4.1, the mean values for each of the integral quantities in the Flattop assemblies are calculated and compared against the results from the most

recent releases of the U.S. nuclear data libraries [63, 1] and the available experimental measurements.

Integral Parameter	Data Library		Present Work	Experimental Benchmark*
	ENDF/B-VII.0	ENDF/B-VII.1		
k_{eff}	0.99917(10)	0.99878(10)	0.99892(10)	1.0000(14)
Leakage	0.31750(3)	0.31799(3)	0.31774(3)	-
$\mathcal{I}^{(238f)}$	0.1876(3)	0.1877(3)	0.1869(3)	0.1916(21)
$\mathcal{I}^{(237f)}$	0.910(1)	0.911(1)	0.909(1)	0.910(13)
$\mathcal{I}^{(239f)}$	1.402(2)	1.404(2)	1.404(2)	-
*Taken From ICSBEP Handbook [13]				

Table 6.9: Flattop-23 critical assembly integral quantities calculated using the ENDF/B-VII libraries compared with the present evaluation work.

In Table 6.9 the computed integral quantities from the U.S. nuclear data libraries, the present evaluation work and the available experimental benchmarks are shown for the Flattop-23 assembly. All of the calculations between the ENDF/B-VII.0, ENDF/B-VII.1 libraries and the modified ENDF/B-VII.1 library with the newly evaluated PFNS all agree in the 95% confidence interval meaning the new PFNS evaluation of the central value has a small impact on the central values of the integral parameters. The largest difference in the libraries exist for the calculated leakage where the new evaluation lies in between the two most recent versions of the U.S. nuclear data library. Comparing between the new evaluation and the experimental benchmarks available for the k_{eff} and the $\mathcal{I}^{(238f)}$ and $\mathcal{I}^{(237f)}$ spectral indices, the results all generally agree within the experimental uncertainties quoted. The largest discrepancy between the present work and the experimental benchmark is the $\mathcal{I}^{(238f)}$ spectral index calculation which is within the 99% confidence interval.

For the Flattop-25 assembly, the computed integral quantities are shown in Table 6.10. All of the data libraries including the present work calculate the k_{eff} value higher than the experimental benchmark calculation but they are within 1-σ of the experimental uncertainties. All of the spectral indices are calculated almost exactly

Integral Parameter	Data Library		Present Work	Experimental Benchmark*
	ENDF/B-VII.0	ENDF/B-VII.1		
k_{eff}	1.00291(9)	1.00271(9)	1.00278(9)	1.0000(30)
Leakage	0.31328(3)	0.31324(3)	0.31244(3)	-
$\mathcal{I}^{(238f)}$	0.1444(4)	0.1446(4)	0.1430(4)	0.1492(16)
$\mathcal{I}^{(237f)}$	0.771(1)	0.772(1)	0.765(1)	0.78(1)
$\mathcal{I}^{(239f)}$	1.360(2)	1.360(2)	1.357(2)	1.385(12)
*Taken From ICSBEP Handbook [13]				

Table 6.10: Flattop-25 critical assembly integral quantities calculated using the ENDF/B-VII libraries compared with the present evaluation work.

between the two U.S. data libraries while the present evaluation of the uranium PFNS leads to slightly lower results while all of the libraries calculate the spectral indices low in comparison to the experimental benchmark values outside of the 1-σ band.

Integral Parameter	Data Library		Present Work	Experimental Benchmark*
	ENDF/B-VII.0	ENDF/B-VII.1		
k_{eff}	1.00012(10)	1.00000(10)	0.99866(10)	1.0000(30)
Leakage	0.33991(3)	0.33981(3)	0.33917(3)	-
$\mathcal{I}^{(238f)}$	0.1771(3)	0.1776(3)	0.1750(3)	0.1799(20)
$\mathcal{I}^{(237f)}$	0.853(1)	0.854(1)	0.846(1)	0.856(12)
$\mathcal{I}^{(239f)}$	1.379(2)	1.380(2)	1.377(2)	-
*Taken From ICSBEP Handbook [13]				

Table 6.11: Flattop-Pu critical assembly integral quantities calculated using the ENDF/B-VII libraries compared with the present evaluation work.

The calculated central values in Table 6.11 for the Flattop-Pu assembly have some trends similar to the Flattop-25 assembly for the calculated spectral indices while the k_{eff} from the present evaluation work is calculated much lower in comparison to the experimental benchmark and both the U.S. nuclear data libraries. Even with the present evaluation calculation of the k_{eff} integral quantity, the results are still within 1-σ of the experimental benchmark uncertainties quoted.

In general, all of the calculations of the integral quantities agree between both of the U.S. nuclear data libraries, the present evaluation of the PFNS and the experimental benchmark calculations. In some cases where the present work seems to calculate the integral quantity further away from the experimental benchmark calculation, this does not mean that the newly evaluated PFNS is to blame. In fact, because the newly evaluated PFNS includes much more experimental data with some recent measurements not previously used and with the inclusion of the anisotropy parameter in the LA model, the work shown in Chapter 4.1 on evaluating the uranium and plutonium actinide suites should result in a much better evaluation of the PFNS for all of the included actinides. Therefore, more of the nuclear data library should also be studied and re-evaluated so that the source of all of the discrepancies with experimental benchmarks can be further understood before concluding that this new evaluation of the PFNS is incorrect.

To determine how the uncertainties in the correlated PFNS impact the uncertainties in the Flattop assembly integral quantities, both the uranium and plutonium PFNS uncertainties are propagated using MCNP5-1.60 utilizing both the standard direct sampling using the posterior model parameter covariance found in the actinide suite evaluation work in Chapter 4.1 and the UMC+TMC approach discussed in Chapter 5.2.2.

Integral Parameter	Monte Carlo Statistics (%)	Uncertainty (%)		
		Direct Sampling	UMC+TMC	Experimental
k_{eff}	0.010	0.521	0.020	0.13
Leakage	0.009	1.180	0.035	-
$\mathcal{I}^{(238f)}$	0.160	7.556	0.114	1.10
$\mathcal{I}^{(237f)}$	0.110	2.334	0.101	1.43
$\mathcal{I}^{(239f)}$	0.142	0.383	0.030	-

Table 6.12: Flattop-23 critical assembly quantified uncertainties due to the uranium suite PFNS uncertainties. The cross-isotope correlations are included in the quantification of the integral parameter uncertainties.

The uncertainties quantified for the integral parameters are displayed in Table 6.12 for the Flattop-23 critical assembly. One thing that is apparent in all of the results shown is that the magnitude of the UMC+TMC quantified uncertainties is much smaller than the direct sampling results. This is easily explained by the missing cross-experiment correlations used in the evaluation procedures for both the Kalman filter and UMC method. More details on the reasoning behind the extremely small uncertainties predicted by the UMC+TMC method will be discussed at the conclusion of this section.

Integral Parameter	Monte Carlo Statistics (%)	Uncertainty (%)		
		Direct Sampling	UMC+TMC	Experimental
k_{eff}	0.009	0.667	0.008	0.30
Leakage	0.010	1.141	0.063	-
$\mathcal{I}^{(238f)}$	0.280	7.497	0.136	1.07
$\mathcal{I}^{(237f)}$	0.131	2.346	0.129	1.28
$\mathcal{I}^{(239f)}$	0.147	0.355	0.019	0.87

Table 6.13: Flattop-25 critical assembly quantified uncertainties due to the uranium suite PFNS uncertainties. The cross-isotope correlations are included in the quantification of the integral parameter uncertainties.

In Table 6.13 the uncertainties in the Flattop-25 assembly are very similar in comparison to the uncertainties in the Flattop-23 assembly in Table 6.12. Both of the Flattop uranium core assemblies are nearly the same size and are both surrounded by a depleted uranium reflector. The main difference between the two assemblies is that the Flattop-23 assembly is highly enriched in ^{233}U while the Flattop-25 assembly is highly enriched in ^{235}U. Regardless of their material compositions, the direct sampling, UMC+TMC and experimental uncertainties behave similarly. The uncertainty calculated for k_{eff} in both assemblies resulting from the direct sampling approach is more than double that of the experimental uncertainties while the $\mathcal{I}^{(237f)}$ spectral index calculated uncertainties are slightly less than double that of the experimental uncertainties. The $\mathcal{I}^{(239f)}$ spectral index uncertainties are calculated to

be relatively small compared with the experimental uncertainties for the Flattop-25 assembly with the uncertainties calculated for both assemblies closest to the associated Monte Carlo statistics. Last, for both the Flattop-23 and Flattop-25 assemblies, the calculated uncertainties for the $\mathcal{I}^{(238f)}$ spectral index are $\sim 7.5\%$ compared with the $\sim 1.1\%$ experimental uncertainty. This proves to be relatively large compared with the experimental uncertainty where some more research on the evaluation of the uranium suite of actinides potentially including some the these integral data to help constrain the evaluation could be done to reduce the PFNS uncertainties.

Integral Parameter	Monte Carlo Statistics (%)	Uncertainty (%)				
		Direct Sampling		UMC+TMC		
		U	Pu	U	Pu	Experimental
k_{eff}	0.010	0.111	0.360	0.004	0.029	0.30
Leakage	0.009	0.296	0.277	0.025	0.026	-
$\mathcal{I}^{(238f)}$	0.171	0.135	2.961	0.144	0.227	1.11
$\mathcal{I}^{(237f)}$	0.118	0.059	1.165	0.043	0.137	1.40
$\mathcal{I}^{(239f)}$	0.145	0.016	0.219	0.012	0.033	-

Table 6.14: Flattop-Pu critical assembly quantified uncertainties due to both the uranium and plutonium suite PFNS uncertainties separately. The cross-isotope correlations are included in the quantification of the integral parameter uncertainties.

Because the Flattop-Pu assembly contains both a plutonium core and a depleted uranium reflector, the quantified uncertainties of each of the integral parameters are shown in Table 6.14 resulting from both the uranium and plutonium PFNS correlated uncertainties. In general, the uncertainties quantified for the integral parameters resulting from the PFNS in the uranium reflector are much smaller than the uncertainties from the plutonium core. The only integral parameter that does not show this trend is the leakage uncertainty which is calculated to be larger coming from the PFNS in the uranium reflector than from the plutonium core. The reason for this is clearly due to the geometry of the assembly with the PFNS in the uranium reflector core, located as the outer shell of the assembly, accounting for a significant

influence on the leakage of the system. The same argument can be made for why the PFNS in the plutonium core leads to significantly larger uncertainties in spectral indices which are calculated at the very center of the assembly far away from the depleted uranium reflector. In terms of trends in the uncertainties noticed in the Flattop-Pu assembly, the PFNS uncertainties impact the assembly very similarly to the uncertainties calculated for the Flattop-23 and Flattop-25 assemblies with the smaller magnitudes of the uncertainties quantified for the Flattop-Pu being the major difference.

In all of the uncertainty quantification results shown in Tables 6.12–6.14 all of UMC+TMC uncertainties are an order of magnitude or more smaller in comparison to the direct sampling uncertainties, considered to be the "benchmark" results. The reason for this is the posterior covariance matrices calculated from the Kalman filter in the actinide suite evaluation work in Chapter 4.1 have all been re-scaled because the evaluated uncertainties were deemed to be too small due to the missing cross-experiment correlations. In the UMC+TMC methodology, there is not a place where this similar re-scaling can be done to correct for the missing cross-experiment correlations. This means that the UMC+TMC method suffers by predicting uncertainties that are smaller than what is generally accepted and should only be used as an uncertainty propagation and quantification methodology when cross-experiment correlations are correctly taken into account.

6.2.3 Summary

In propagating the cross-correlated PFNS uncertainties through the Big Ten and Flattop assemblies several observations can be made about the sampling method, the impact of the cross-correlations and the newly implemented UMC+TMC method. By sampling from the model parameters and using the LA model calculation for

each realization of the model parameters, the sampling statistics deviate far from the evaluated PFNS uncertainties that have been proposed for the next release of the ENDF/B-VII nuclear data library prepared directly from the actinide suite evaluation work in Chapter 4.1. Because of the rigidity and nonlinearities present in the LA model, the uncertainties and correlations in the PFNS are found to be significantly different in both shape and magnitude. However, in order to propagate cross-isotope correlations present in the PFNS uncertainties, sampling using the model parameter covariance matrix becomes necessary for computational efficiency and simplicity.

The impact that the cross-isotopes correlations can have on the quantified integral parameters was investigated for the Big Ten assembly. Because of the material composition and the energy range of the assembly, the effects of the correlations can be summarized as follows:

- The k_{eff} uncertainties were calculated to be 17.5% smaller using the uncorrelated PFNS.
- The $\mathcal{I}^{(238f)}$ spectral index uncertainties were calculated to be 10.4% smaller using the uncorrelated PFNS.
- The $\mathcal{I}^{(237f)}$ spectral index uncertainties were calculated to be 1.4% smaller using the uncorrelated PFNS.
- The $\mathcal{I}^{(239f)}$ spectral index uncertainties were smaller than the Monte Carlo statistics from the MCNP5-1.60 calculations.

In conclusion, the cross-isotope correlations impacted the Big Ten uncertainty propagation results a significant amount and should be used where possible to conservatively predict the uncertainties in the final integral parameters.

The newly implemented UMC+TMC method was used to quantify the uncertainties in the integral parameters and comparisons were made with the direct sampling

approach applied to the posterior model parameter covariance matrix resulting from the actinide suite evaluation work. The UMC+TMC method sampled from the prior model parameters, then formally included all of the experimental data available to constrain the weight of each realization and finally each PFNS realization went through each of the Flattop assembly simulations using MCNP5-1.60. In all of the cases where the quantified uncertainties were larger than the Monte Carlo statistics, the UMC+TMC uncertainties were generally found to be an order of magnitude lower compared with the calculated direct sampling uncertainties. Much like the Kalman filter and the UMC method used to quantify the PFNS uncertainties, the UMC+TMC method suffers from the fact that cross-experiment correlations and model deficiencies are not accounted for in the evaluation procedure, leading to extremely small uncertainties in the final integral parameters. Fortunately for the Kalman filter and the UMC method, the posterior uncertainties in the covariance matrix are scaled up to a reasonable value from their originally calculated uncertainties, and the PFNS realizations are drawn from this re-scaled phase space. In the UMC+TMC method, because the covariance matrix formulation is bypassed, there is not a point at which the uncertainties can be scaled up to a reasonable value causing the extremely small quantified uncertainties. This method has been shown to work, but without the proper cross-experiment correlations available, the quantified integral parameter uncertainties are calculated to be much too small to have confidence in the result.

Chapter 7

Conclusions and Future Work

This work focused on evaluating and quantifying nuclear data uncertainties and propagating these uncertainties through neutron transport simulations of several important critical assemblies. To quantify the uncertainties in the prompt fission neutron spectrum (PFNS), two approaches were used: the first-order, linear Kalman filter and the unified Monte Carlo (UMC) method. The Kalman filter was implemented for the evaluation of the PFNS and its associated uncertainties for both the uranium and plutonium suites of actinides resulting in new evaluations including cross-isotope correlations in the PFNS uncertainties. One important aspect of this evaluation work was that the PFNS for the minor actinides, for which little experimental data exist, were evaluated consistently using the experimental data of the major actinides to constrain the Los Alamos (LA) model parameters. Presently in the ENDF/B-VII.1 nuclear data library, the evaluated PFNS for any given set of actinides rely on different physics models including evaporation, Watt and LA model theories, and this work provided a way to consistently evaluate these actinides along with their uncertainties within the framework of a single theoretical model. In general, the resulting PFNS evaluations were in agreement with the available experimental data and have been submitted for review and testing on various integral benchmarks. Also, for

the first time, cross-isotope correlations for the PFNS are provided through the LA model calculations and were used for a handful of applications in the uncertainty propagation portion of the present work. This uncertainty quantification and evaluation effort on the PFNS has been submitted for publication in the peer-reviewed, Nuclear Science and Engineering journal.

The UMC approach, which is a new method only having been studied on a toy problem, was implemented in an effort to compare alternative evaluation methodologies with the Kalman filter approach. Because the original implementation of the UMC method was not considered to be mathematically rigorous, several variations of the UMC approach were implemented for the evaluation of the PFNS, to further understand its advantages and limitations. It was found that while excluding the use of experimental data, the original UMC sampling algorithm was flawed in the application of this specific problem, leading to significant differences from the Kalman filter. We suggested a new approach to sample from a Gaussian distribution of the prior model parameters rather than a uniform distribution, and this led to very good agreement with the Kalman filter results. When experimental data was included in the evaluation using the two UMC approaches, the results were very similar due to the constraints put on the model parameters from the experimental data. Most importantly, the UMC implementations were capable of capturing the nonlinearities present in the LA model leading to a slightly different evaluation compared to the Kalman filter results. However, because these nonlinearities are mostly present in the high outgoing-energy tail of the PFNS, the impact on applications is considered to be negligible. In other words, the Kalman filter is perfectly suited to accurately evaluate the PFNS using the LA model.

In a second part of this work, we investigated the impact that the PFNS uncertainties have on the metrics of several nuclear engineering applications. The uncertainties quantified for the PFNS were propagated through neutron transport simula-

tions of the Lady Godiva, Jezebel, Big Ten and Flattop assemblies using two forward propagation methods: a "brute force" direct sampling approach and the polynomial chaos expansion - stochastic collocation method (PCE-SCM). First, the PCE-SCM approach was used to quantify the uncertainties in the Lady Godiva and Jezebel assemblies originating from the PFNS uncertainties available in the ENDF/B-VII.1 nuclear data library. In particular the ^{235}U PFNS covariance matrix, made available by the author of this work for the release of the ENDF/B-VII.1 data library [1], and the ^{239}Pu PFNS covariance matrix were decomposed using the principal component analysis (PCA). It was found that the matrices contained a maximum of three principal components describing the uncertainties and correlations present in each of the PFNS evaluations. By reducing the random dimension of the PFNS uncertainties, the implementation of the PCE-SCM demonstrated orders of magnitude computational savings compared with direct sampling to obtain the full characterization of the output quantity uncertainties in terms of the moments and probability distributions. This work provided a strong case for using these powerful stochastic spectral methods to obtain the uncertainties in the effective multiplication factor, total leakage and fission reaction spectral indices of these important critical assemblies in a computationally efficient manner. Note that this portion of work using the PCE-SCM methods to propagate the PFNS uncertainties has been submitted for publication in the peer-reviewed, Nuclear Science and Engineering journal.

Finally, the uncertainties quantified across the suite of uranium and plutonium actinides were used to propagate the cross-isotope correlations in the PFNS uncertainties through the Big Ten and Flattop assemblies. Direct sampling from the model parameters was done and each PFNS realization was obtained through an LA model calculation. For the Big Ten assemblies, the PFNS uncertainties were considered uncorrelated and correlated to study the impact that the cross-isotope correlations have on the moments of output quantity uncertainties. In general, it was found that the cross-isotope correlations led to larger predicted uncertainties in

the output quantities with the largest relative difference being $\sim 17.5\%$ for the effective multiplication of the system, suggesting that these cross-isotope correlations are very important for these applications. A new method, the unified Monte Carlo + total Monte Carlo (UMC+TMC) method was also implemented to propagate the correlated uncertainties through the Flattop assemblies. Compared with the direct sampling from the posterior model parameter covariance matrix, the UMC+TMC method predicted all of the output quantity uncertainties to be smaller by an order of magnitude or more, while the direct sampling uncertainties were reasonably predicted compared with the available experimental uncertainties. This result was expected and is mainly due to the missing cross-experiment correlations in all the evaluation methodologies used here. When reasonable cross-experiment correlations become available, the UMC+TMC method is expected to be an effective method for propagating uncertainties from the prior parameters, allowing for nonlinearities in both the LA model and the transport simulations to propagate to the final quantified uncertainties in the output variables.

As a result of this work, many interesting and important research topics remain. The most glaring obstacle that remains, especially for the uncertainty quantification methods presented in this work, is the availability of cross-experiment correlations. At this point, these correlations are not considered and due to this missing information that would be used in the implementations of the Kalman filter and UMC method, *ad hoc* corrections are made based mainly on expert judgement. These *ad-hoc* corrections, a simple re-scaling of posterior uncertainties in some cases, have been demonstrated to be effective, but cannot be implemented easily in the UMC+TMC method. Researching and understanding everything that the experimentalists did in the past and assigning correlations between separate experiments is not a trivial task. Fortunately, significant efforts are being placed on this subject and hopefully cross-experiment correlations will be available in the near future that can be used to re-evaluate not only the PFNS and its uncertainties but many other nuclear reactions

as well.

In terms of the evaluation methods and uncertainty quantification, the work presented here can be quickly extended in several areas. First, the actinide suite evaluation work can be extended to include other actinides, e.g., thorium, neptunium, americium, protactinium, where it will be important to study other differential, semi-integral and integral data that can be used in the evaluation to help constrain the evaluated model parameters. Also, this work should be extended to include higher incident neutron energies, above the threshold for second-chance fission, requiring theoretical physics components like a pre-equilibrium spectrum calculation in addition to the modified LA model. Also, because more measurements exist for the energy dependent average multiplicity, $\bar{\nu}(E)$, compared with the PFNS, this quantity could be used to help constrain the PFNS evaluation at higher incident neutron energies. Several research directions still remain for the implementation of the UMC evaluation methodology studied in this work. First, improvements should be made to increase the parallel computing capability, inherent in the UMC approach. Already underway, several quadrature-based sampling methods are being explored as a way of improving the UMC method with respect to the computational cost of the "brute force" Monte Carlo implementation. Another research direction that has already brought significant attention to the nuclear data evaluation community is the use of new and improved theoretical models such as the Monte Carlo Hauser-Feshbach (MCHF) model. Because of the stochastic nature of the MCHF model, it remains to be seen if the UMC evaluation method can be used with this new model to evaluate new nuclear data, including neutron multiplicity distributions and neutron-neutron correlations, far beyond the capabilities of the LA model.

The first obvious extension to the uncertainty propagation and quantification research presented in this work is to apply the same PCA, PCE-SCM and uncertainty propagation methods for the PFNS to many other important nuclear engineering

applications including: nuclear energy and reactor physics, radiation shielding and dosimetry, criticality safety, nuclear medicine, astrophysics and other complex multi-physics systems in the presence of significant nonlinearities. Another obvious extension is to perform the same analysis on other evaluated nuclear data, i.e. cross sections and fission neutron multiplicities, to study the impact of these quantified uncertainties on various applications. Due to the computational cost of simulating some of the highly complex nonlinear systems that are being modeled, such as nuclear reactor and weapon simulations, it would interesting to study the applicability of some of these stochastic spectral methods on these systems with the potential of improving the amount of information gained while reducing the computational cost of quantifying uncertainties.

Appendices

Appendix A

Matrix Inversion Identities

The following identities help when trying to invert a matrix of the form $(\mathbf{A}+\mathbf{BCD})$. More detailed derivations of the "matrix inversion lemma" or "Sherman-Morrison-Woodbury Identity" can be found in further reading [104, 105].

In inverting the matrix $(\mathbf{A}+\mathbf{BCD})$, a couple of identities need to be introduced. First is inverting a matrix $(\mathbf{I}+\mathbf{P})$:

$$\begin{aligned}(\mathbf{I}+\mathbf{P})^{-1} &= (\mathbf{I}+\mathbf{P})^{-1}(\mathbf{I}+\mathbf{P}-\mathbf{P}) \\ &= \mathbf{I}-(\mathbf{I}+\mathbf{P})^{-1}\mathbf{P} \end{aligned} \tag{A.1}$$

The second identity is helpful in manipulating complicated matrix multiplications:

$$\begin{aligned}\mathbf{P}+\mathbf{PQP} &= \mathbf{P}(\mathbf{I}+\mathbf{QP}) \\ &= (\mathbf{I}+\mathbf{PQ})\mathbf{P} \\ (\mathbf{P}^{-1}+\mathbf{Q})^{-1} &= ((\mathbf{I}+\mathbf{QP})\mathbf{P}^{-1})^{-1} = \mathbf{P}(\mathbf{I}+\mathbf{QP})^{-1} \\ &= (\mathbf{P}^{-1}(\mathbf{I}+\mathbf{PQ}))^{-1} = (\mathbf{I}+\mathbf{PQ})^{-1}\mathbf{P} \end{aligned} \tag{A.2}$$

To invert the sum of matrices of the form $(\mathbf{A}+\mathbf{BCD})$, $\mathbf{A}$ must be invertible:

$$\begin{aligned}(\mathbf{A}+\mathbf{BCD})^{-1} &= (\mathbf{A}[\mathbf{I}+\mathbf{A}^{-1}\mathbf{BCD}])^{-1} \\ &= [\mathbf{I}+\mathbf{A}^{-1}\mathbf{BCD}]^{-1}\mathbf{A}^{-1} \\ &= [\mathbf{I}-(\mathbf{I}+\mathbf{A}^{-1}\mathbf{BCD})^{-1}\mathbf{A}^{-1}\mathbf{BCD}]\mathbf{A}^{-1} \\ &= \mathbf{A}^{-1}-(\mathbf{I}+\mathbf{A}^{-1}\mathbf{BCD})^{-1}\mathbf{A}^{-1}\mathbf{BCDA}^{-1} \qquad \text{(A.3)}\end{aligned}$$

The third line in Eq. (A.3) used the identity in Eq. (A.1). Now repeatedly using the identity in Eq. (A.2) results in:

$$\begin{aligned}(\mathbf{A}+\mathbf{BCD})^{-1} &= \mathbf{A}^{-1}-(\mathbf{I}+\mathbf{A}^{-1}\mathbf{BCD})^{-1}\mathbf{A}^{-1}\mathbf{BCDA}^{-1} \\ &= \mathbf{A}^{-1}-\mathbf{A}^{-1}(\mathbf{I}+\mathbf{BCDA}^{-1})^{-1}\mathbf{BCDA}^{-1} \\ &= \mathbf{A}^{-1}-\mathbf{A}^{-1}\mathbf{B}(\mathbf{I}+\mathbf{CDA}^{-1}\mathbf{B})^{-1}\mathbf{CDA}^{-1} \\ &= \mathbf{A}^{-1}-\mathbf{A}^{-1}\mathbf{BC}(\mathbf{I}+\mathbf{DA}^{-1}\mathbf{BC})^{-1}\mathbf{DA}^{-1} \\ &= \mathbf{A}^{-1}-\mathbf{A}^{-1}\mathbf{BCD}(\mathbf{I}+\mathbf{A}^{-1}\mathbf{BCD})^{-1}\mathbf{A}^{-1} \\ &= \mathbf{A}^{-1}-\mathbf{A}^{-1}\mathbf{BCDA}^{-1}(\mathbf{I}+\mathbf{BCDA}^{-1})^{-1} \qquad \text{(A.4)}\end{aligned}$$

In case when $\mathbf{C}$ is also invertible the inverse can take the form:

$$\begin{aligned}(\mathbf{A}+\mathbf{BCD})^{-1} &= \mathbf{A}^{-1}-\mathbf{A}^{-1}\mathbf{B}(\mathbf{I}+\mathbf{CDA}^{-1}\mathbf{B})^{-1}\mathbf{CDA}^{-1} \\ &= \mathbf{A}^{-1}-\mathbf{A}^{-1}\mathbf{B}[\mathbf{C}^{-1}(\mathbf{I}+\mathbf{CDA}^{-1}\mathbf{B})]^{-1}\mathbf{DA}^{-1} \\ &= \mathbf{A}^{-1}-\mathbf{A}^{-1}\mathbf{B}(\mathbf{C}^{-1}+\mathbf{DA}^{-1}\mathbf{B})^{-1}\mathbf{DA}^{-1} \qquad \text{(A.5)}\end{aligned}$$

In another related special case when $\mathbf{C}$ is invertible, the matrix $(\mathbf{A}+\mathbf{BCD})^{-1}\mathbf{BC}$

can be manipulated to take the form:

$$\begin{aligned}
(\mathbf{A}+\mathbf{BCD})^{-1}\mathbf{BC} &= [(\mathbf{I}+\mathbf{BCDA}^{-1})\mathbf{A}]^{-1}\mathbf{BC} \\
&= \mathbf{A}^{-1}(\mathbf{I}+\mathbf{BCDA}^{-1})^{-1}\mathbf{BC} \\
&= \mathbf{A}^{-1}\mathbf{B}(\mathbf{I}+\mathbf{CDA}^{-1}\mathbf{B})^{-1}\mathbf{C} \\
&= \mathbf{A}^{-1}\mathbf{B}[\mathbf{C}^{-1}(\mathbf{I}+\mathbf{CDA}^{-1}\mathbf{B})]^{-1} \\
&= \mathbf{A}^{-1}\mathbf{B}(\mathbf{C}^{-1}+\mathbf{DA}^{-1}\mathbf{B})^{-1} \qquad \text{(A.6)}
\end{aligned}$$

The matrix inversion manipulations shown in Eqs. (A.3)–(A.6) using only standard matrix inversion properties and the identities in Eqs. (A.1) and (A.2) are useful when manipulating the Kalman filter update equations to a more useful computational form.

Appendix B

Exponential Matrix Integrals

We wish to calculate the moments of multivariate Gaussian distribution. First we define the elements of the mean as,

$$\langle x_i \rangle = \frac{\int_{-\infty}^{\infty} \cdots \int_{-\infty}^{\infty} x_i \exp\left\{-\frac{1}{2}\left(\vec{x}-\vec{b}\right)^T \mathbf{A}\left(\vec{x}-\vec{b}\right)\right\} d\vec{x}}{\int_{-\infty}^{\infty} \cdots \int_{-\infty}^{\infty} \exp\left\{-\frac{1}{2}\left(\vec{x}-\vec{b}\right)^T \mathbf{A}\left(\vec{x}-\vec{b}\right)\right\} d\vec{x}}\,, \tag{B.1}$$

and the elements of the covariance matrix as,

$$P_{i,j} = \frac{\int_{-\infty}^{\infty} \cdots \int_{-\infty}^{\infty} x_i x_j \exp\left\{-\frac{1}{2}\left(\vec{x}-\vec{b}\right)^T \mathbf{A}\left(\vec{x}-\vec{b}\right)\right\} d\vec{x}}{\int_{-\infty}^{\infty} \cdots \int_{-\infty}^{\infty} \exp\left\{-\frac{1}{2}\left(\vec{x}-\vec{b}\right)^T \mathbf{A}\left(\vec{x}-\vec{b}\right)\right\} d\vec{x}} - \langle x_i \rangle \langle x_j \rangle\,, \tag{B.2}$$

where the indices are defined for $i, j = 1, \ldots, N$, with the $\vec{x}$ and $\vec{b}$ vectors having N elements and $\mathbf{A}$ being a real, symmetric N-by-N matrix. Because $\mathbf{A}$ is real and symmetric it can be diagonalized such that,

$$\mathbf{A} = \mathbf{S}\mathbf{D}\mathbf{S}^{-1} = \mathbf{S}\mathbf{D}\mathbf{S}^T\,, \tag{B.3}$$

$$\mathbf{A}^{-1} = \mathbf{S}\mathbf{D}^{-1}\mathbf{S}^{-1} = \mathbf{S}\mathbf{D}^{-1}\mathbf{S}^T\,, \tag{B.4}$$

where the $\mathbf{S}$ matrix is orthonormal with the determinant equal to unity, $|\mathbf{S}| = 1$. The $\mathbf{D}$ and $\mathbf{D}^{-1}$ matrices are strictly diagonal. Now we perform a change of variables,

$$\vec{x} - \vec{b} = \mathbf{S}\vec{y}\,, \tag{B.5}$$

$$d\vec{x} = \mathbf{S}d\vec{y} = |\mathbf{S}|dy_1 dy_2 \cdots dy_N\,. \tag{B.6}$$

Inserting the definitions in Eqs. (B.5)–(B.6) into Eq. (B.1) and using the property in Eq. (B.3) we find the elements for the mean are now,

$$\begin{aligned}\langle x_i \rangle &= b_i + \frac{\int_{-\infty}^{\infty} \cdots \int_{-\infty}^{\infty} [\mathbf{S}\vec{y}]_i \exp\left\{-\frac{1}{2}\vec{y}^T\mathbf{S}^T\mathbf{A}\mathbf{S}\vec{y}\right\} d\vec{y}}{\int_{-\infty}^{\infty} \cdots \int_{-\infty}^{\infty} \exp\left\{-\frac{1}{2}\vec{y}^T\mathbf{S}^T\mathbf{A}\mathbf{S}\vec{y}\right\} d\vec{y}} \\ &= b_i + \frac{\int_{-\infty}^{\infty} \cdots \int_{-\infty}^{\infty} [\mathbf{S}\vec{y}]_i \exp\left\{-\frac{1}{2}\vec{y}^T\mathbf{D}\vec{y}\right\} d\vec{y}}{\int_{-\infty}^{\infty} \cdots \int_{-\infty}^{\infty} \exp\left\{-\frac{1}{2}\vec{y}^T\mathbf{D}\vec{y}\right\} d\vec{y}}\,.\end{aligned} \tag{B.7}$$

The $[\mathbf{S}\vec{y}]_i$ term can be expanded,

$$[\mathbf{S}\vec{y}]_i = \sum_{k=1}^{N} S_{i,k}y_k\,, \tag{B.8}$$

while the exponent term can also be expanded,

$$\vec{y}^T\mathbf{D}\vec{y} = \sum_{l=1}^{N} d_l y_l^2\,, \tag{B.9}$$

where the d_l are the diagonal elements of the matrix $\mathbf{D}$. Inserting these definitions into Eq. (B.7) we have,

$$\langle x_i \rangle = b_i + \frac{\int_{-\infty}^{\infty} \cdots \int_{-\infty}^{\infty} \sum_{k=1}^{N} S_{i,k}y_k \exp\left\{-\frac{1}{2}\sum_{l=1}^{N} d_l y_l^2\right\} d\vec{y}}{\int_{-\infty}^{\infty} \cdots \int_{-\infty}^{\infty} \exp\left\{-\frac{1}{2}\sum_{l=1}^{N} d_l y_l^2\right\} d\vec{y}}\,. \tag{B.10}$$

Notice that, while the expression remains rather complex, each integral in the numerator of Eq. (B.10) comes down a simple integration that can be done for the k-th term,

$$C \int_{-\infty}^{\infty} y_k \exp\left\{-\frac{1}{2} d_k y_k^2\right\} dy_k = 0\,, \tag{B.11}$$

where C is a nonzero constant defined by the integration terms moved outside of the k-th integral. Due to the evaluated integral in Eq. (B.11), the numerator in Eq. (B.10) is zero leading to the final expression for the components of the mean,

$$\langle x_i \rangle = b_i\,, \tag{B.12}$$

or, generalized as the mean vector,

$$\langle \vec{x} \rangle = \vec{b}\,. \tag{B.13}$$

Now, inserting the definitions in Eqs. (B.5)–(B.6) into Eq. (B.2) and applying Eq. (B.3), we find the elements for the covariance are now,

$$P_{i,j} = \frac{\int_{-\infty}^{\infty} \cdots \int_{-\infty}^{\infty} \left([\mathbf{S}\vec{y}]_i + b_i\right)\left([\mathbf{S}\vec{y}]_j + b_j\right) \exp\left\{-\frac{1}{2}\vec{y}^T \mathbf{D}\vec{y}\right\} d\vec{y}}{\int_{-\infty}^{\infty} \cdots \int_{-\infty}^{\infty} \exp\left\{-\frac{1}{2}\vec{y}^T \mathbf{D}\vec{y}\right\} d\vec{y}} - \langle x_i \rangle \langle x_j \rangle\,. \tag{B.14}$$

Now we expand the non-exponential terms in Eq. (B.14) as,

$$\left([\mathbf{S}\vec{y}]_i + b_i\right)\left([\mathbf{S}\vec{y}]_j + b_j\right) = [\mathbf{S}\vec{y}]_i [\mathbf{S}\vec{y}]_j + b_j [\mathbf{S}\vec{y}]_i + b_i [\mathbf{S}\vec{y}]_j + b_i b_j\,. \tag{B.15}$$

Inserting the expansion in Eq. (B.15) into Eq. (B.14) it is clear that the final term does not depend on the variables of integration and can be moved outside the integrals. Using the solution for elements of the mean, in Eq. (B.12), the final term in

Eq. (B.14) cancels out leaving,

$$P_{i,j} = \frac{\int_{-\infty}^{\infty} \cdots \int_{-\infty}^{\infty} ([\mathbf{S}\vec{y}]_i [\mathbf{S}\vec{y}]_j + b_j [\mathbf{S}\vec{y}]_i + b_i [\mathbf{S}\vec{y}]_j) \exp\left\{-\frac{1}{2}\vec{y}^T \mathbf{D}\vec{y}\right\} d\vec{y}}{\int_{-\infty}^{\infty} \cdots \int_{-\infty}^{\infty} \exp\left\{-\frac{1}{2}\vec{y}^T \mathbf{D}\vec{y}\right\} d\vec{y}} . \tag{B.16}$$

Also, the $b_j[\mathbf{S}\vec{y}]_i$ and $b_i[\mathbf{S}\vec{y}]_j$ terms in the expanded Eq. (B.16) lead to integrals analogous to the ones in Eq. (B.10) where the integrals are equal to zero in the numerator. Now Eq. (B.16) is simplified to,

$$P_{i,j} = \frac{\int_{-\infty}^{\infty} \cdots \int_{-\infty}^{\infty} [\mathbf{S}\vec{y}]_i [\mathbf{S}\vec{y}]_j \exp\left\{-\frac{1}{2}\vec{y}^T \mathbf{D}\vec{y}\right\} d\vec{y}}{\int_{-\infty}^{\infty} \cdots \int_{-\infty}^{\infty} \exp\left\{-\frac{1}{2}\vec{y}^T \mathbf{D}\vec{y}\right\} d\vec{y}} . \tag{B.17}$$

Expanding the $\mathbf{S}\vec{y}$ terms leads to,

$$P_{i,j} = \frac{\int_{-\infty}^{\infty} \cdots \int_{-\infty}^{\infty} \left(\sum_{k=1}^{N} S_{i,k} y_k\right) \left(\sum_{k=1}^{N} S_{j,l} y_l\right) \exp\left\{-\frac{1}{2}\vec{y}^T \mathbf{D}\vec{y}\right\} d\vec{y}}{\int_{-\infty}^{\infty} \cdots \int_{-\infty}^{\infty} \exp\left\{-\frac{1}{2}\vec{y}^T \mathbf{D}\vec{y}\right\} d\vec{y}} . \tag{B.18}$$

Once again, seen in Eqs. (B.10) and (B.11), when $l \neq k$, the numerator is equal to zero leaving only the terms when $l = k$. The final, simplified form of the covariance matrix is then,

$$P_{i,j} = \sum_{k=1}^{N} S_{i,k} S_{j,k} \frac{\int_{-\infty}^{\infty} y_k^2 \exp\left\{-\frac{1}{2} d_k y_k^2\right\} dy_k}{\int_{-\infty}^{\infty} \exp\left\{-\frac{1}{2} d_k y_k^2\right\} dy_k} . \tag{B.19}$$

It is easy to show that the ratio of univariate integrals in Eq. (B.19) is,

$$\frac{\int_{-\infty}^{\infty} y_k^2 \exp\left\{-\frac{1}{2} d_k y_k^2\right\} dy_k}{\int_{-\infty}^{\infty} \exp\left\{-\frac{1}{2} d_k y_k^2\right\} dy_k} = d_k^{-1} , \tag{B.20}$$

leading to a very clean definition for the elements of the covariance matrix, and with a little investigating, they can also be identified as the elements in Eq. (B.4) leading to,

$$\begin{aligned} P_{i,j} = \sum_{k=1}^{N} S_{i,k} S_{j,k} d_k^{-1} &= \left[\mathbf{S}\mathbf{D}^{-1}\mathbf{S}^T\right]_{i,j} \\ &= \left[\mathbf{A}^{-1}\right]_{i,j} , \end{aligned} \tag{B.21}$$

or, generalized as the covariance matrix,

$$\mathbf{P} = \mathbf{A}^{-1} . \tag{B.22}$$

References

[1] M.B. Chadwick, M. Herman, P. Oblozinsky *et al.*, "ENDF/B-VII.1 Nuclear Data for Science and Technology: Cross Sections, Covariances, Fission Product Yields and Decay Data," *Nuclear Data Sheets*, **112**, 2887 (2011).

[2] K. Shibata, O. Iwamoto *et al.*, "JENDL-4.0: A New Library for Nuclear Science and Engineering," *J. Nucl. Sci. Tech.*, **48**, 1-30 (2011).

[3] "The JEFF-3.1.1 Nuclear Data Library," OECD/NEA Report No. 6807, Ed. A. Santamarina, D. Bernard, and Y. Rugama (2009).

[4] OECD/WPEC Subgroup 26, "Uncertainty and Target Accuracy Assessment for Innovative Systems Using Recent Covariance Data Evaluations," M. Salvatores Coordinator, http://www.nea.fr/html/science/wpec (2008).

[5] M. Ishikawa, "Recent Application of Nuclear Data to Fast Reactor Core Analysis and Design in Japan," *Proceedings of Inter. Conf. on Nucl. Data for Sci. and Techn.* (Santa Fe, USA, 2004), p. 1405.

[6] M. Salvatores, G. Aliberti *et al.*, "Uncertainty and Target Accuracy Assessment for Innovative Systems Using Recent Covariance Data Evaluations," Report NEA/WPEC-26, OECD, Paris, (2008).

[7] G. Aliberti, G. Palmiotti, M. Salvatores, T.K. Kim, T.A. Taiwo, M. Anitescu, I. Kodeli, E. Sartori, J.C. Bosq, and J. Tommasi, "Nuclear Data Sensitivity, Uncertainty and Target Accuracy Assessment for Future Nuclear Systems," *Ann. Nucl. Energy*, **33**, 700 (2006).

[8] http://www.gen-4.org/

[9] R.E. Kalman, "A New Approach to Linear Filtering and Prediction Problems," *J. Basic Eng.*, **82D**, 35-45 (1960).

[10] R. Capote and D.L. Smith, "An Investigation of the Performance of the Unified Monte Carlo Method of Neutron Cross Section Data Evaluation," *Nucl. Data Sheets*, **109** (12), 2768 (2008).

[11] A.J. Koning and D. Rochman, "Towards Sustainable Nuclear Energy: Putting Nuclear Physics to Work," *Ann. Nucl. Energy*, **35**, 2024-30 (2008).

[12] H.C. Paxton, "A History of Critical Experiments at Pajarito Site," LA-9685-H, Los Alamos National Laboratory (1985).

[13] *International Handbook of Evaluated Criticality Safety Benchmark Experiments*, OECD Nuclear Energy Agency report NEA/NSC/DOC(95)03, September 2010 Edition.

[14] R.H. White, "Topsy, A Remotely Controlled Critical Assembly Machine," *Nucl. Sci. Eng.*, **1**, 53-61 (1956).

[15] R.E. Peterson and G.A. Newby, "An Unreflected U-235 Critical Assembly," *Nucl. Sci. Eng.*, **1**, 112-25 (1956).

[16] G.A. Jarvis, G.A. Linenberger, J.D. Orndoff, and H.C. Paxton, "Two Plutonium-Metal Critical Assemblies," *Nucl. Sci. Eng.*, **8**, 525-31 (1960).

[17] G.E. Hanson and H.C. Paxton, "Reevaluated Critical Specification of Some Los Alamos Fast-Neutron Systems," LA-4208, Los Alamos National Laboratory (1969).

[18] G.E. Hanson and H.C. Paxton, "A Critical Assembly of Uranium Enriched to 10% in Uranium-235," *Nucl. Sci. Eng.*, **72**, 230-6 (1979).

[19] B. Davison, *Neutron Transport Theory*, Oxford University Press, 1957.

[20] G.I. Bell and S. Glasstone, *Nuclear Reactor Theory*, Reinhold, 1970.

[21] J.J. Duderstadt and L.J. Hamilton, *Nuclear Reactor Analysis*, John Wiley & Sons, New York, 1976.

[22] E.E. Lewis and W.F. Miller, Jr., *Computational Methods of Neutron Transport*, John Wiley & Sons, New York, 1984.

[23] A.D. Carlson, V.G. Pronyaev, D.L. Smith *et al.*, "International Evaluation of Neutron Cross Section Standards," *Nuclear Data Sheets*, **110**, 3215 (2009).

[24] R.S. Varga, *Matrix Iterative Analysis*, Prentice-Hall, Englewood Cliffs, N.J., 1962.

[25] E. Wachspress, *Iterative Solution of Elliptic Systems*, Prentice-Hall, Englewood Cliffs, N.J., 1966.

[26] J. von Neumann, letter to R.D. Richtmyer, "Statistical Methods in Neutron Diffusion," LAMS-551, Los Alamos National Laboratory (1947).

[27] E.D. Cashwell and C.J. Everett, *A Practical Manual on the Monte Carlo Method for Random Walk Problems*, Pergamon Press, London, 1959.

[28] I. Lux and L. Koblinger, *Monte Carlo Particle Transport Methods: Neutron and Photon Calculations*, CRC Press, Boston, 1991.

[29] X-5 MONTE CARLO TEAM, "MCNP - A General N-Particle Transport Code, Version 5 - Volume I: Overview and Theory," LA-UR-03-1987, Los Alamos National Laboratory (2003).

[30] F.B. Brown, B.C. Kiedrowski, and J.S. Bull, "MCNP5-1.60 Release Notes," LA-UR-10-06235, Los Alamos National Laboratory (2010).

[31] EXFOR, Experimental Nuclear Reaction Data Base (2011). Available from <**http://www-nds.iaea.org/EXFOR**>

[32] R. Capote *et al.*, "Prompt Fission Neutron Spectra of Major Actinides," INDC(NDS)-0571 (2010).

[33] W.P. Poenitz and S.E. Aumeier, "Nuclear Data and Measurement Series, The Simultaneous Evaluation of the Standards and Other Cross Sections of Importance for Technology," Argonne National Lab., USA, September 1997, ANL/NDM-139.

[34] T. Kawano, P. Talou, M.B. Chadwick, and T. Watanabe, "Monte Carlo Simulation for Particle and γ-Ray Emissions in Statistical Hauser-Feshbach Model," *J. Nucl. Sci. Tech.*, **47** (5), 462-69 (2010).

[35] P. Talou, B. Becker, T. Kawano, M.B. Chadwick, and Y. Danon, "Advanced Monte Carlo Modeling of Prompt Fission Neutrons for Thermal and Fast Neutron-Induced Fission Reaction on Pu-230," *Phys. Rev. C*, **83**, 064612 (2011).

[36] J.C. Browne and F.S. Dietrich, "Hauser-Feshbach Calculation of the ^{252}Cf Spontaneous-Fission Neutron," *Phys. Rev. C*, **10** (6), 2545-49 (1974).

[37] J. Randrup and P. Möller "Brownian Shape Motion on Five-Dimensional Potential-Energy Surfaces: Nuclear Fission-Fragment Mass Distributions," *Phys. Rev. Lett.*, **106**, 132503 (2011).

[38] V. Weisskopf, "Statistics and Nuclear Reactions," *Phys. Rev.*, **52** (4), 295-303 (1937).

[39] D.G. Madland and J.R. Nix, "New Calculation of Prompt Fission Neutron Spectra and Average Prompt Neutron Multiplicities", *Nucl. Sci. Eng.*, **81**, 213-71 (1982).

[40] T. Ericson and V. Strutinski, "On Angular Distributions in Compound Nucleus Processes," *Nucl. Phys.*, **8**, 284 (1958).

[41] A. Tudora, "Systematic Behaviour of the Average Parameters Required for the Los Alamos Model of Prompt Neutron Emission," *Ann. Nucl. Energy*, **36** (1), 72-84 (2009).

[42] D. Smith, *Workshop on Neutron Cross Section Covariances*, Port Jefferson, NY, 27-28 June 2008.

[43] D. Smith, *Covariance Workshop*, Port Jefferson, NY, 23 June 2009.

[44] D.M. Hetric and C.Y. Fu, "GLUCS: A Generalized Least-Squares Program for Updating Cross-section Evaluations with Correlated Data Sets," ORNL/TM-7341 (1980).

[45] D.L. Smith, *Probability, Statistics and Data Uncertainties in Nuclear Science and Technology*, American Nuclear Society, LaGrange Park, IL, USA (1991).

[46] T. Kawano and K. Shibata, "Covariance Evaluation System," JAERI Data/Code, Japan Atomic Energy Research Institute, Tokai, Japan (1997).

[47] D.L. Smith, "Covariance Matrices for Nuclear Cross Sections Derived from Nuclear Model Calculations," ANL/NDM-159, Argonne National Laboratory (2004).

[48] A.J. Koning, "New Working Methods for Nuclear Data Evaluation: How to Make a Nuclear Data Library," *Proc. Int. Conf. on Nuclear Data for Science and Technology*, O. Bersillon, *et al.* (Eds.), EDP Sciences (2008), DOI:10.105/ndata:07683.

[49] A.J. Koning and D. Rochman, "Modern Nuclear Data Evaluation: Straight from Nuclear Physics to Applications", to appear in *Proceedings of the International Conference on Nuclear Data for Science and Technology*, Jeju, Korea (26-30 April 2010).

[50] D. Rochman, A.J. Koning, and S.C. van der Marck, "Uncertainties for Criticality-safety Benchmarks and k_{eff} Distributions", *Ann. Nucl. Energy*, **36**, 810-31 (2009).

[51] D. Rochman *et al.*, "On the evaluation of ^{23}Na Neutron-induced Reactions and Validations," *Nucl. Instr. Meth.*, **A612**, 374 (2010).

[52] D. Rochman, A.J. Koning, and S.C. van der Marck, "Exact Nuclear Data Uncertainty Propagation for Fusion Design," *Fusion Engineering and Design*, **85**, 669-82 (2010).

[53] E. Bauge, S. Hilaire, and P. Dossantos-Uzarralde, *Proceedings of the International Conference on Nuclear Data for Science and Technology*, 22-27 April 2007, Nice, France, O. Bersillon, *et al.* (Eds.), EDP Sciences (2008), p. 259.

[54] D.W. Muir *et al.*, "The Global Assessment of Nuclear Data, GANDR," *Proc. Int. Conf. on Nuclear Data for Science and Technology*, O. Bersillon, *et al.* (Eds.), EDP Sciences (2008), *http://dx.doi.org/10.1051/ndata:07635.*

[55] M. Herman *et al.*, "EMPIRE: Nuclear Reaction Model Code System for Data Evaluation," *Nucl. Data Sheets*, **108**, 2655-715 (2007).

[56] T. Kawano, "Estimation of Energy Dependence of the Optical Potential Parameters for ^{209}Bi," *Nucl. Sci. Eng.*, **131**, 107-15 (1999).

[57] P. Talou, P.G. Young, T. Kawano, M. Rising, and M.B. Chadwick, "Quantification of Uncertainties for Evaluated Neutron-Induced Reactions on Actinides in the Fast Energy Range," *Nucl. Data Sheets*, **112**, 3054 (2011).

[58] T. Bayes, "An Essay Toward Solving a Problem in the Doctrine of Chances," *Phil. Trans. Royal Soc. London*, **53**, 370-418 (1763).

[59] C.E. Shannon, "A Mathematical Theory of Communication," *The Bell System Technical J.*, **27**, 379-423 and 623-656 (July and October 1948).

[60] E.T. Jaynes, "Information Theory and Statistical Mechanics," *Phys. Rev.*, **106** (4), 620-30 (1957).

[61] N. Metropolis, A. Rosenbluth, M. Rosenbluth, A. Teller, and E. Teller, "Equation of State Calculations by Fast Computing Machines," *J. Chem. Phys.*, **21** (6), 1087-92 (1953).

[62] W.K. Hastings, "Monte Carlo Sampling Methods Using Markov Chains and Their Applications," *Biometrika*, **57** (1), 97-109 (1970).

[63] M.B. Chadwick, P. Oblozinsky, M. Herman *et al.*, "ENDF-B/V-II.0: Next Generation Evaluated Nuclear Data Library for Nuclear Science and Technology," *Nucl. Data Sheets* **107**, 2931 (2006).

[64] M.E. Rising, P. Talou, and A.K. Prinja, "Evaluation of Uncertainties for the Prompt Fission Neutron Spectrum and Average Neutron Multiplicity using the Los Alamos Model," *Trans. Am. Nucl. Soc.*, **104**, p.796-8 (2011).

[65] M.E. Rising, P. Talou, T. Kawano, and A.K. Prinja, "Systematic Uncertainty Quantification of Prompt Fission Neutron Spectra," submitted to Nuclear Science and Engineering (May 2012).

[66] P. Talou, T. Kawano, D.G. Madland *et al.*, "Uncertainty Quantification of Prompt Fission Neutron Spectrum for n(0.5 MeV)+239Pu," *Nucl. Sci. Eng.*, **166**, 254 (2010).

[67] N. Kornilov, F.-J. Hambsch, I. Fabry *et al.*, "The ^{235}U(n,f) Prompt Fission Neutron Spectrum at 100 K Input Neutron Energy," *Nucl. Sci. Eng.*, **165**, 117 (2010).

[68] A.S. Vorobyev, O.A. Shcherbakov, Yu.S. Pleve *et al.*, "Angular and Energy Distributions of Prompt Neutrons from Thermal Neutron-Induced Fission of U-233, U-235 (N,F)," *International Seminar on Interaction of Neutrons with Nuclei* (Dubna, Russia, 2009), p. 60.

[69] T. Miura, M. Baba, Thanwin, *et al.*, "Measurements of the Fast Neutron-Induced Prompt Neutron Fission Spectra of ^{233}U, ^{238}U, ^{232}Th.," *J. Nucl. Sci. Tech. Suppl.*, **2** (1), 204 (2002).

[70] A. Lajtai, J. Kecskemeti, J. Safar *et al.*, "Prompt Neutron Spectra for Energy Range 30 keV – 4 MeV from Fission of U-233, U235 and Pu-239 induced by Thermal Neutrons," *Proceedings of Inter. Conf. on Nucl. Data for Sci. and Techn.* (Santa Fe, USA, 1986), p. 613.

[71] B.I. Starostov, V.N. Nefedov, and A.A. Boytsov, "Prompt Neutron Spectra from Thermal Neutron Fission of ^{233}U, ^{235}U, ^{239}Pu and Spontaneous Fission of ^{252}Cf in the Secondary Neutron Energy Range 0.01 – 12 MeV," *VANT, Nucl. Constants*, **3**, 16-22 (1985).

[72] A.A. Boytsov, A.F. Semenov, and B.I. Starostov, "Relative Measurements of the Spectra of Prompt Fission Neutrons for Thermal Neutron Fission of the Nuclei U-233, U-235, Pu-230 in the Energy Range 0.01 – 5 MeV," *Proc. 6th All-Union Conf. on Neutron Physics* (Kiev, U.S.S.R., 1983), p. 294.

[73] P. Staples, J.J. Egan, G.H.R. Kegel *et al.*, "Prompt Fission Neutron Energy Spectra Induced by Fast Neutrons," *Nucl. Phys. A*, **591**, 41 (1995).

[74] G.S. Boikov, V.D. Smitriev, G.A. Kudyaev *et al.*, "Neutron Spectrum in the Fission of Th-232, U-235 and U-238 by Neutron with Energies 2.9 and 14.7 MeV," *Yad. Fiz.*, **53**, 628 (1991).

[75] Wang Yufeng, Bai Xixiang, Li Anli *et al.*, "Experimental Study of Prompt Neutron Spectrum of the ^{235}U Fission Induced by Thermal Neutrons," *Chin. J. Nucl. Phys.*, **11**, 47-56 (1989).

[76] P.I. Johansson, B. Holmqvist, and T. Wiedling, "An Experimental Study of the Prompt Fission Neutron Spectrum Induced by 0.5 MeV Incident Neutrons on U-235," *Nucl. Sci. Eng.*, **62**, 695 (1977).

[77] J.M. Adams and P.I. Johansson, "Fast Neutron Fission Spectrum Measurement of U-235 at 0.52 MeV Incident Neutron Energy," *Proc. Washington Conf. on Nuclear Cross-Sections and Technology II* (Washington, USA, 1975), p. 631.

[78] A.M. Trufanov, G.N. Lovchikova, M.I. Svirin *et al.*, "Investigation of the Neutron Spectra in Fission of Nucleus 238-U Induced by Fast Neutrons with Energies of 5.0 and 13.2 MeV," *Yad. Fiz.*, **64**, 3 (2001).

[79] M. Baba, H. Wakabayashi, M. Ishikawa *et al.*, "Fission Spectrum Measurement of Th-232 and U-238 for 2 MeV Neutrons," INDC(NDS)-220, Physics of Neutron Emission in Fission, MITO (1988) p. 149.

[80] D.G. Madland, "Total Prompt Energy Release in the Neutron-Induced Fission of ^{235}U, ^{238}U, and ^{239}Pu," *Nucl.Phys. A*, **772**, 113-37 (2006).

[81] H.H. Knitter, M.M. Islam, and M. Coppola, "Investigation of Fast Neutron Interaction with U-235," *Z. Phys.*, **257**, 108 (1972).

[82] E.P. Wigner, "Effects of Small Perturbations on Pile Period," CP-3048, Manhattan Project Report (1945).

[83] A. Gandini, "A Generalized Perturbation Method for Bi-Linear Functionals of the Real and Adjoint Neutron Fluxes," *J. Nucl. Eng.*, **21**, 755-65 (1967).

[84] A. Gandini, G. Palmiotti, and M. Salvatores, "Equivalent Generalized Perturbation Theory (EGPT)," *Ann. Nucl. Energy*, **13** (3), 109-14 (1986).

[85] B.T. Rearden, "Perturbation Theory Eigenvalue Sensitivity Analysis with Monte Carlo Techniques," *Nucl. Sci. Eng.*, **146**, 367-82 (2004).

[86] B.T. Rearden, "TSUNAMI-3D: Control Module for Three-Dimensional Cross Section Sensitivity and Uncertainty Analysis for Criticality," ORNL/TM-2005/39 Version 6, Oak Ridge National Laboratory (2009).

[87] B. Kiedrowski, F. Brown, and P. Wilson, "Calculating Kinetics Parameters and Reactivity Changes with Continuous-Energy Monte Carlo," *Proceedings of PHYSOR 2010 – Advances in Reactor Physics to Power the Nuclear Renaissance*, Pittsburgh, Pennsylvania, USA, May 9-14, 2010, on CD-ROM, American Nuclear Society, LaGrange Park, IL (2010).

[88] M. Loéve, *Probability Theory II*, 4th ed., New York: Springer-Verlag (1977).

[89] R. Ghanem and P. Spanos, *Stochastic Finite Elements: A Spectral Approach*, Springer-Verlag, New York (1991).

[90] E.D. Fichtl, *Stochastic Methods for Uncertainty Quantification in Radiation Transport*. Doctoral dissertation, University of New Mexico, May 2009.

[91] A.M.J. Olsson and G.E. Sandberg, "Latin Hypercube Sampling for Stochastic Finite Element Analysis," *J. Eng. Mech.*, **128**(1), 121-5 (2002).

[92] M.E. Rising, E.D. Fichtl, and A.K. Prinja, "Application of Principle Component Analysis to Uncertainty Propagation in Radiation Transport," *Trans. Am. Nucl. Soc.*, **104**, 334-6 (2011).

[93] K. Pearson, "On Lines and Planes of Closest Fit Systems of Points in Space," *Philosophical Magazine*, **2** (11), 559-72 (1901).

[94] I.T. Jolliffe, *Principal Component Analysis*, 2nd ed., Springer: Series in Statistics (2002).

[95] M.E. Rising and A.K. Prinja, "The Principal Component Analysis Method used with Polynomial Chaos Expansion to Propagate Uncertainties through Critical Transport Problems," presented at the Advances in Reactor Physics Conference (PHYSOR 2012), Knoxville, TN, April 15-20 (2012).

[96] J. Helton, J. Johnson, C. Sallaberry, and C. Storlie, "Survey of Sampling-based Methods for Uncertainty and Sensitivity Analysis," *Reliability Engineering & System Safety*, **91**, 1175-209 (2006).

[97] M.D. McKay, R.J. Beckman, and W.J. Conover, "A Comparison of Three Methods for Selecting Values of Input Variables in the Analysis of Output from a Computer Code," *Technometrics*, **21** (2), 239-45 (1979).

[98] D. Xiu and G.E. Karniadakis, "The Wiener-Askey Polynomial Chaos for Stochastic Differential Equations," *SIAM J. Sci. Comput.*, **24**, 619-44 (2002).

[99] E.D. Fichtl, A.K. Prinja, and J.S. Warsa, "Stochastic Methods for Uncertainty Quantification in Radiation Transport," *Proc. of the International Conference on Mathematics, Computational Methods and Reactor Physics*, Saratoga Springs, NY, USA, American Nuclear Society (2009).

[100] E.D. Fichtl and A.K. Prinja, "The Stochastic Collocation Method for Radiation Transport in Random Media," *J. Quant. Spectrosc. Radiat. Transfer*, **112**, 646-59 (2011).

[101] D.A.F. Ayres, M.D. Eaton, A.W. Hagues, and M.M.R. Williams, "Uncertainty Quantification in Neutron Transport with Generalized Polynomial Chaos using the Method of Characteristics," *Ann. Nucl. En.*, **45**, 14-28 (2012).

[102] N. Wiener, "The Homogeneous Chaos," *Amer. J. Math.*, **60**, 897-936 (1938).

[103] L. Mathelin, M. Hussaini, and T. Zang, "Stochastic Approaches to Uncertainty Quantification in CFD Simulations," *Numerical Algorithms*, **38** (1-3), 209-36 (2005).

[104] H.V. Henderson and S.R. Searle, "On Deriving the Inverse of a Sum of Matrices," *SIAM Review*, **23**(1), 53-60 (1981).

[105] D.J. Tylavsky and G.R.L. Sohie, "Generalization of the Matrix Inversion Lemma," *Proceedings of the IEEE*, **74**(7), 1050-2 (1986).